TRANSPORTS OF POLYMER NANOMEDICINE IN THE ENVIRONMENT

A Dissertation

by

MING ZHANG

Submitted to the Office of Graduate and Professional Studies of
Texas A&M University
in partial fulfillment of the requirements for the degree of

DOCTOR OF PHILOSOPHY

Chair of Committee,	Mustafa Akbulut
Committee Members,	Perla Balbuena
	Zhilei Chen
	Mark Lenox
Head of Department,	M. Nazmul Karim

December 2013

Major Subject: Chemical Engineering

ABSTRACT

With increasing production and commercial use of polymer nanomedicine and a lack of regulation to govern their disposal, polymer nanomedicine may enter into soils and ultimately into ground water system. In this dissertation, adsorption of polymeric nanoparticulate drug delivery system (PNDDS) in the environmental surface as well as uptake of nanomedicine into plants was investigated. Cellulose surface and silica surface were chosen as environmental surfaces and ryegrass was chosen as a plant.

The adsorption of PNDDS onto cellulose and silica surface was studied by quartz crystal microbalance with dissipation (QCM) and atomic force microscopy (AFM). Uptake of PNDDS into ryegrass was investigated by spectrofluorometry (SFM), confocal microscopy, scanning electron microscopy (SEM) and cross sectional transmission electron microscopy (TEM).

It is found that PNDDS can partially irreversibly adsorb on cellulose and silica surface. After adsorption, PNDDS may deform, disintegrate, or keep the same size depended on properties of PNDDS and PNDDS/surface interaction. Uptake of PNDDS into ryegrass was observed and PNDDS was found both in root cell and intercellular space. PNDDS could transport up to stem of ryegrass but not leaf. Adsorption onto root surface is the rate-determined step of the uptake process.

This dissertation represents an important step in understanding environmental impact of polymer nanomedicine. This is very important considering that PNDDS on and in the plants may later be consumed by animals and bacteria and accumulate in their

bodies, and can adversely influence environmental health. Also silica/cellulose surface and plants may also be used to treat waste water with PNDDS. Transport behavior and kinetics of PNDDS onto environmental surface studied in this dissertation also could guide to study transport behavior of the same type or other types of polymer nanomedicine in similar or other environmental systems.

DEDICATION

This dissertation is dedicated to my parents, Youtang and Jiaozhi, for their unconditional love and support throughout the courses of my academic career and of my whole life. This dissertation is also dedicated to my wife, Xiuting, whose endless love and care during these years. And it is also dedicated to my brother and sisters, Hongying, Xiongying, Jun, Xiangying and Bao, who always support me and shape the person I have become.

ACKNOWLEDGEMENTS

I would like to acknowledge the contribution and extensive knowledge of Dr. Mustafa Akbulut, whose guidance and patience are invaluable. Many thanks to Dr. Luis Cisneros-Zevallos and my committee members, Dr. Perla Balbuena, Dr. Zhilei Chen and Dr. Mark Lenox, for their guidance and support throughout the course of this research.

I would also like to extend my thanks to the staff of the Microscopy and Imaging Center, the staff of the Materials Characterization Facility for their support and training on state-of-the art equipment. Finally, I would like to thank all members in Dr. Akbulut's group for their help and cooperation necessary for the success of this work.

NOMENCLATURE

AFM	atomic force microscopy
BD	Brownian dynamics
DLS	dynamic light scattering
DTPA	diethylentriaminepentaacetic dianhydide
FDA	Food and Drug Administration
MWNT	multfi-walled carbon nanotubes
PCL	poly ε-carprolectone
PEG	polyethyleneglycol
PNDDS	polymeric nanoparticulate drug delivery systems
PLL	poly(L-lysine)
PS	polystyrene
RSA	random sequential adsorption
QCM-D	quartz crystal microbalance with dissipation
SEM	scanning electron microscopy
SFM	spectrofluorometry
SiNP	silica nanoparticles
SWNI	single-walled carbon nanotubes
TEM	transmission electron microscopy
THF	tetrahydrofuran
VDW	van der Waals

TABLE OF CONTENTS

Page

LIST OF FIGURES

Page

LIST OF TABLES

Page

CHAPTER I

INTRODUCTION

1.1 Background and Significance

Breathtaking developments in the area of nanotechnology over the last decade have opened up avenues to dramatic changes in the way that devices, materials, and systems are fabricated. The area of nanotechnology has been especially beneficial in the field of medicine. There are 247 nanomedicines that have been approved for use, under clinical trial data, or on the verge of clinical study according to a recent study relying on a detailed search of the literature, clinical trial data, and the Web [1]. Another recent study has reported that the global market value of nanomedicine reached $72.8 billion in 2011 [2]. While nanomedicines play an important role in the treatment and prevention of disease, the side effects of medicines on human and animal health resulting directly from treatment have been widely documented. However, it is only recently that the occurrence and fate of medicines in the environment, along with their potential consequences for human health, have been recognized as issues warranting consideration [3-6].

Nanoemulsions, liposomes, polymeric nanoparticles, surfactant micelles, dendrimers, and semiconductor nanocrystals are the major types of nanomedicines (Fig. 1.1) [7]. Currently, among these nanomedicines, polymeric nanoparticulate drug delivery systems (PNDDS) filled with therapeutic agents represent the one of the most commonly used forms of nanomedicine due to their increased bioavailability, ability to solubilize hydrophobic molecules, their higher payload capacity, excellent thermodynamic solution

stability in aqueous environments, and prolonged blood circulation times [8-12]. These properties of nanomedicines are very beneficial from pharmaceutical science perspective. However, from the environmental perspective, these properties can be undesirable. First, therapeutic component of nanomedicine can be toxic to living organisms at lower concentrations compared to therapeutic components due to their improved solubility and bioavailability. Second, polymeric nanomedicines can enable the distribution of insoluble therapeutics in the aqueous environment, which is otherwise impossible or can occur in very limited degree. Third, polymeric nanomedicines can enhance the amount of hazardous hydrophobic therapeutics carried into environment due to their high load capacities. Fourth, polymeric nanomedicine can persist a prolonged period of time in the environment and, thus, have a larger impact radius upon uncontrolled releases and accidental spills due to their stability in aqueous environments.

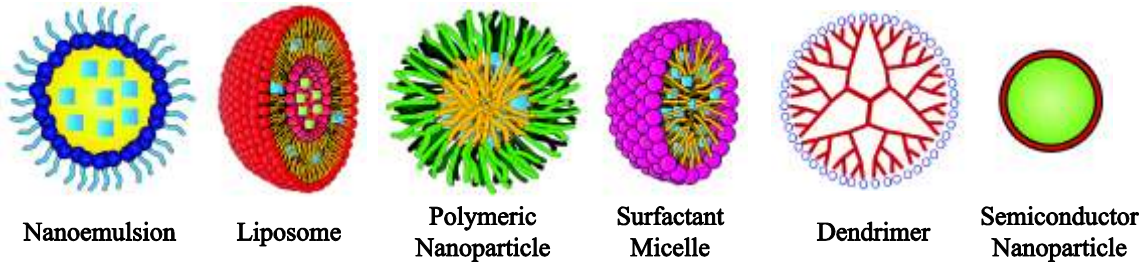

Figure 1.1. The major classes of nanomedicines.

Emerging PNDDS are predominantly loaded with hydrophobic therapeutics such as paclitaxel [13-15], docetaxel [16, 17], cisplatin [18-20], etoposide [15], fluorouracil [21-23], and estradiol [24, 25]. Recent ecotoxicity studies on Daphnia magna have revealed that cisplatin, fluorouracil, and estradiol belong among the compounds that are highly toxic for aquatic organisms (EC50 < 1 mg/L), paclitaxel and doxorubicin are

considered toxic (EC50 ranging 1-10 mg/L), and etoposide is harmful to aquatic organisms (10-100 mg/L) [26-28]. Other ecotoxicity studies on Pseudomonas putida have indicated similar trends of acute ecotoxicity associated with cisplatin and fluorouracil [28].

As most PNDDS are loaded with therapeutic materials that are ecotoxic, nanomedicine is an environmental concern. This concern is exacerbated by recent in vivo studies indicating that some of the intravenously administered nanomedicine can be excreted from the body intact through kidney or as metabolite through the liver/bile duct [29-32]. For instance, Lacerda *et al*. [33] dynamically tracked *in vivo* intravenously administered, multi-walled carbon nanotubes (having diameter of 20-30 nm and length of 500 nm) functionalized with diethylentriaminepentaacetic dianhydride (DTPA-MWNT) and radiolabeled with Indium-111 (111In) using a microSingle Photon Emission Tomography scanner. Imaging showed that nanotubes enter the systemic blood circulation and within 5 min begin to permeate the renal glomerular filtration system into the bladder. Urinary excretion of DTPA-MWNT was confirmed at 24 h post-administration. He *et al*. [34] has investigated the biodistribution and urinary excretion of different surface-modified silica nanoparticles (SiNPs) in mice in situ using an *in vivo* optical imaging system. They studies have demonstrated that three types of *iv*-injected 45-nm silica nanoparticles including polymer (PEG)-coated ones were partly excreted through the renal excretion route. In another study, siRNA DOTA/DOPE complexes (250 nm) and siRNA RGD-polyethylene imine-polymethylene glycol complex (130 nm), one type of polymer nanomedicine, showed a rapid renal clearance by glomerular

filtration [32]. These studies confirm that after administration, some portion of nanomedicine can be excreted from the body.

Nanomedicine can be released into the environment through various routes (Fig. 1.2). Residues released during the manufacturing process may eventually enter the surface water. After administration, some nanomedicine may be directly excreted out of the body [32, 33] and can reach the sewer system as mentioned above. These nanomedicines will usually go through a treatment facility before finding their way into receiving waters or land through the application of sewage sludge. Engineered nanoparticles released to wastewater and wastewater sludge may find their way to food chain [35-37]. Other routes of entry include the disposal of unused medicines and containers. Nanomedicine released into soils, sediments, and sewage systems may eventually find their way into groundwater, reservoirs, and river systems and, thereby, may enter into the food chains of living organisms. These release routes cover a number of different flow geometries over various types of environmental surfaces such as flow over vitrified clay of WC, flow inside polyethylene plastic or vitrified clay sewage pipe, flow in soil, flow near plant roots, and flow near aquatic life forms.

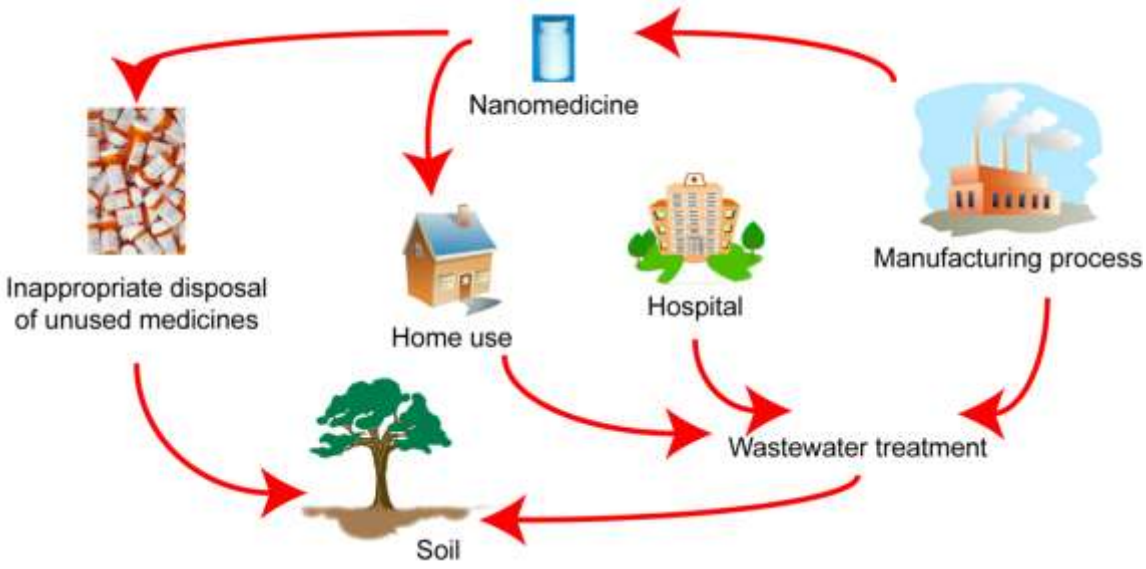

Figure 1.2. Routes by which nanomedicines enter the environment. The most important routes are waste effluents from manufacturing processes, excreta, disposal of unused or expired drug products, and accidental spills during manufacturing or distribution.

1.2 Transport Phenomena of Nanoparticles

The transport of a nanoparticle dispersion depositing onto a surface can be described by the convective diffusion theory [38]:

$$\frac{\delta N}{\delta t} = D_\infty \nabla^2 N - \vec{v}\nabla N - kN \qquad [1.1]$$

where N is the number of particles per unit area, D_∞ is the particle diffusion coefficient, k is the deposition rate coefficient, and v is the fluid velocity. At distances far from the solid surface, convection dominates over diffusion for transport of nanoparticles. At distances very close to the solid surface, the solvent stream movement is slow while the concentration gradient is large. In such regions, the contribution of diffusion to the nanoparticle movement is comparable to or larger than convection.

To determine the net concentration change at a particular point in time, we need to know the liquid flow pattern and boundary, and initial conditions. For generic

colloidal dispersions, the perfect sink conditions i.e., all particles arriving at the surface will adsorb, is a common assumption used in obtaining an approximate solution for Eq. 1.1. However, as time evolves and particles become adhered, the perfect sink condition is no longer valid, and then interactions between particles and the excluded area effects are present, which implies a time-dependent boundary condition for which analytical solutions are not available. To this end, numerical models have been developed, mainly the random sequential adsorption (RSA) model and Brownian dynamics (BD) simulations [39]. The RSA model is simpler and computationally less demanding and gives results consistent with experiments [39]. BD has also been applied to model systems, such as latex particles and globular proteins deposited onto mica surfaces [39].

Treatments of the detachment process have also been published [40, 41]. These aforementioned studies assumed laminar flow, but there are also some treatments for turbulent flow conditions [42, 43]. For polymeric nanomedicine, very little experimental information on the adsorption and desorption kinetics and thermodynamics on polymeric nanomedicine to environmental surfaces is available in the literature. Hence, the choice of the deposition rate coefficient as well as (time-dependent) boundary conditions for the convective-diffusion equation, which is critical for understanding the transport of polymeric nanomedicine in the environment, is currently not clear.

1.3 Transport of Nanoparticles in the Environment

There are numerous studies investigating the transport of various types of traditional materials such as solutes [44-46], amphiphiles [47-49], viruses [50-52], and colloidal particles [53-55] in the environment. Recently, the focus of environmental

transport studies has shifted towards engineered nanomaterials. To this end, many field and laboratory investigations focusing on the distribution and fate of nanomaterials such as TiO2 [56-58], CeO2 [59, 60], ZnO [61-63], Au [64], Fe2O3 [65], Al [66], Ag [67], CdSe [68], fullerenes [69], and carbon nanotubes [70-72] in the environment have recently been conducted. A common conclusion of these studies is that interactions between such nanomaterials and environmental interfaces, and interactions between nanoparticles themselves strongly influence the transport behavior of these nanoparticles in the environment.

To be specific, for instance, Guzman et al. [73] investigated the effect of pH on TiO2 nanoparticle aggregation and transport in porous media and found that over 80% of suspended particles and aggregates were mobile over the pH range of 1−12, except when close to the isoelectric point, where the particles were highly aggregated. Fang et al. [57] demonstrated that TiO2 nanoparticles are stable in soil suspensions, and the suspended TiO2 relative concentrations were positively correlated with dissolved organic carbon and clay contents, and negatively correlated with ionic strength, zeta potential and pH.

Darlington et al. [66] investigated the transport of aluminum nanoparticles in soil and sand matrices. They found that transport of aluminum nanoparticles was inversely related to the size of the agglomerated particles. Depending on the ionic strength of the solution in which they were suspended, the agglomerate size increased with time and further affected transport. In solutions that mimic surface water conditions of moderate ionic strength, aluminum nanoparticles will rapidly form micron-sized agglomerates and restrict transport. Similarly, particles loaded to the top of the column had limited

transport because of clogging of the matrix by agglomerates. Particles that remain unagglomerated and relatively small (200 nm) have greater transport potential, however, and could potentially reach groundwater or surface water. Particles with a surface charge similar to that of the matrix are transported, and those with opposite charges are retained in the matrix.

Elimelech and co-workers investigated the transport of single-walled carbon nanotubes (SWNTs) in soil columns [74]. They found that SWNT shape and structure, predominantly the very large aspect ratio and its highly bundled (aggregated) state in aqueous solutions, as well as the heterogeneity in soil particle size, porosity, and permeability, collectively contribute to straining in flow through soil media. They concluded that highly anisotropic and bundled SWNTs will not exhibit substantial transport and infiltration in soils because of effective retention by the soil matrix.

1.4 Interactions between Nanoparticle and Environmental Interfaces

Molecular interactions between a nanoparticle and a surface determine the adsorption and desorption behavior, and, as a consequence, modulate the transport of the nanoparticle near the surfaces. However, very little is known about the adsorption and desorption kinetics and thermodynamics of nanomedicine around environmental interfaces. Thus, in the following paragraphs, we will summarize the current state of knowledge on the interactions between “generic” engineered nanoparticle such as TiO2, ZnO, and Au nanoparticles and common types of substrates, and discuss the similarities and differences of generic engineered nanoparticles and nanomedicine.

The nanoparticle-substrate interactions are governed by physicochemical properties of (i) nanoparticleliquid interface; (ii) substrate-liquid interface; and, (iii) the contact zone between the nanoparticle-liquid interface and the substrate (Fig. 1.3) [75]. In a given medium, most important nanoparticle characteristics that determine the nature of interactions between a nanoparticle and a substrate are chemical composition, surface functionalization, size, shape, surface area, porosity, crystallinity, and heterogeneity of the nanoparticle [75, 76]. Other important quantifiable properties of nanoparticles, such as the effective surface charge (zeta potential), particle aggregation, state of dispersion, stability/biodegradability, dissolution characteristics, and hydration and valence properties of the surface layer are determined by the characteristics of the suspending medium [77, 78], which include the ionic strength, pH, temperature, and the presence of large organic molecules or surfactants [79].

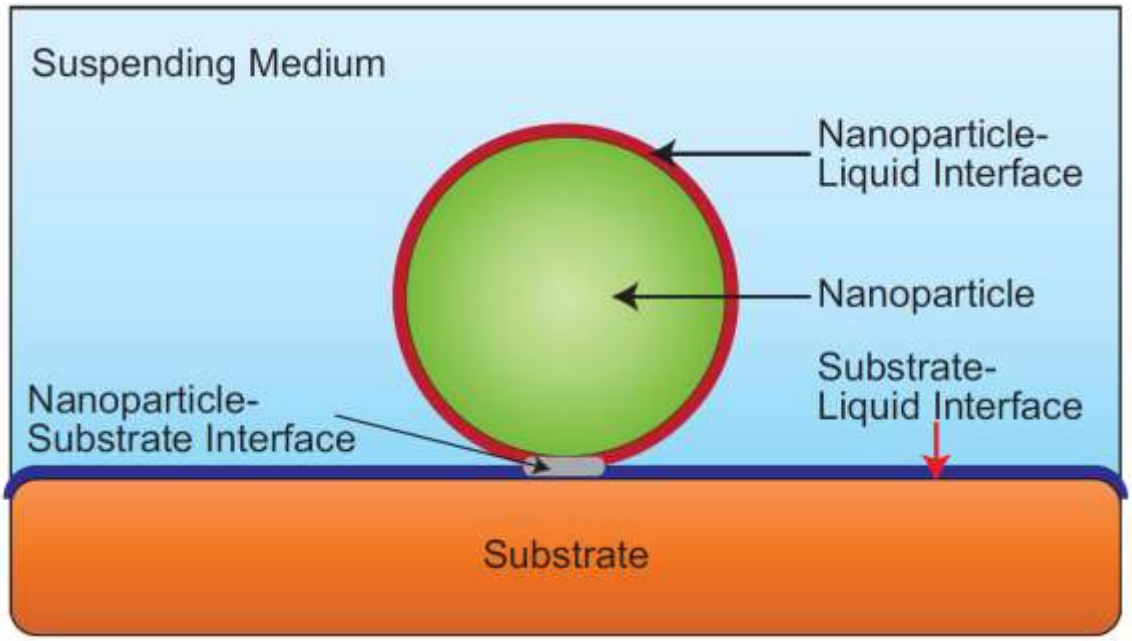

Figure 1.3. The main effects that occur between a nanoparticle and substrate stem from material properties, modification of the surface properties of those materials through interactions with the suspending medium, and the dynamic interactions of the solid–liquid interface with the substrate.

The particle characteristics contribute actively to the interactions with the medium through the following methods: (i) promoting the adsorption of ions, proteins, natural organic materials and detergents; (ii) double-layer formation; (iii) dissolution; or, (iv) minimizing free surface energy by surface restructuring [79]. Many of these newly acquired particle properties or transformed states determine the forces that operate at the nanoparticle-medium interface with characteristic decay lengths. These forces include long-range forces arising from attractive van der Waals (VDW) and (generally) repulsive electrostatic double-layer interactions as well as short-range forces arising from charge, steric, depletion, and solvent interactions [79]. Medium interactions (for example, protein interactions) could also induce large-scale changes, such as nanoparticle dissolution, ion leaching, phase transformation, and agglomeration [75].

Polymeric nanomedicines differ from the generic nanoparticles discussed above in two ways: (i) Polymeric nanomedicines usually have micellar core/shell structure, in which the core contains the hydrophobic part of an amphiphilic polymer and hydrophobic drug, and the shell contains the hydrophilic part of the amphiphilic polymer in an aqueous solution (Fig. 1.1). In contemporary formulations, a biocompatible polymer with very low critical micelle concentration and high glass transition temperature is typically selected as hydrophobic part of polymeric nanomedicine. Thus, polymeric nanomedicines have advantages over conventional surfactant micelles in that they have better thermodynamic stability in physiological solution, since amphiphilic polymers have remarkably lower critical micellar concentrations than surfactants. Namely, unlike traditional surfactant micelles, the polymeric nanomedicine core is a

kinetically frozen structure, which does not experience monomer association and dissociation i.e. it is not a dynamic system. Strong stability is an important requirement for most drug delivery systems. Otherwise, the administered drug will never reach the target site. (ii) For "generic" nanoparticles, the shell (corona) layer is thin relative to the core of the nanoparticles. The corona layer is responsible for screening out van der Waals interactions occurring between the core and a substrate, and it also introduces repulsive steric (entropic) forces in the overall system. On the other hand, structures of polymeric nanomedicine are "hairy" nanostructures, i.e., the core of the nanoparticles is thin relative to the shell of nanoparticles (Fig. 1.1). Thus, steric repulsion and screening of van der Waals interactions of polymeric nanomedicine are much stronger than that of generic nanoparticles. This means that hairy structure also provides an improved stability, which is an important requirement for drug delivery applications. These two differences bring additional contributions to the nanoparticle-substrate interactions discussed above, thereby can alter the transport behavior of polymeric nanomedicine significantly.

1.5 Summary and Objectives

In summary, environmental aspects of engineered nanoparticles are receiving increased attention as the consumption and production volumes of engineered nanoparticles increase [80, 81]. Various research groups have focused on different environmental aspects for various types of nanoparticles such as organic, inorganic, and metal nanoparticles, carbon nanotubes, and viruses. However, similar studies on polymeric nanomedicine are rather limited.

The overarching goal of the dissertation is to generate a fundamental understanding of the transport phenomena of nanomedicine in the environment. we aim to determine the relative importance of convection, diffusion, adsorption, desorption, and uptake processes taking place in such transport phenomena and how these processes depend upon the structural and physicochemical properties of the nanomedicine and the environmental surfaces involved. The specific objectives of this dissertation are: (i) adsorption and desorption of polymeric nanomedicine onto environmental surfaces; and (ii) uptake and translocation of polymeric nanomedicine in the vicinity of plant roots.

CHAPTER II

ADSORPTION OF POLYMERIC NANOPARTICLES*

2.1 Introduction

In general, adsorption is the transfer of an adsorbate from one phase to the adsorbent surface of an adjacent phase, and the accumulation of adsorbate at the interface resulting of the binding forces between the adsorbate and the adsorbent surface. These binding forces or interactions involve the weak van der Waals attraction contributing to physical adsorption, or the strong covalent bonds, i.e. hydrogen binding, in chemisorption. Usually physical adsorption is weak and reversible, while chemisorption is much strong and irreversible. Compared to other adsorption phenomena, polymer adsorption shows a range of binding energies depending on the type of forces present at the interface. Moreover, polymer adsorption is very different from that of small molecules. This is due to the large number of conformations that a macromolecule can adopt, both in the bulk solution and at the interface. Furthermore, the entropy loss or gain associated with a given flexible polymer can be substantially greater than that for small molecules or relatively stiff molecules [82]. Polymeric nanoparticles differ from polymers in their sizes and shapes, which affect the physical interaction such as van der Waals interactions, Born interactions, electric double layer interactions and so on.

---

*Reproduced with permission from Adhesion, Friction, and Lubrication of Polymeric Nanoparticles and their Applications, by Hongbo Zeng, in *Polymer Adhesion, Friction, and Lubrication,* 2013, New York. Copyright 2013 by Wiley.

Studies on adsorption behavior of polymeric nanoparticles can be divided into two: (i) adsorption of functional molecules on polymeric nanoparticles and (ii) adsorption of polymeric nanoparticles on large surfaces.

2.2 Adsorption onto Polymeric Nanoparticles

Adsorption onto polymeric nanoparticles involves the adsorption of small molecular agents or large molecules, mainly proteins, onto the polymeric nanoparticles. In this system, the polymeric nanoparticles act as the adsorbent surface, and the size of adsorbate is smaller than or similar to the polymeric nanoparticles. Adsorption of these adsorbates onto polymeric nanoparticles may (i) protect functional adsorbates and increase their stability, (ii) format targeted delivery of the adsorbate, (iii) improve the surface property of polymeric nanoparticles such as increasing bioavailability, enhancing cellulose uptake, and prolonging blood circulation time.

Adsorption of therapeutic molecules onto polymeric nanoparticles was well studied as one method to fabricate drug delivery systems. Not only do they enhance the uptake of the drugs but they also provide good stability. It is found that adsorption of drugs onto polymeric nanoparticles may increase their cellular uptake and their *vitro* or *vivo* stability [83, 84]. Adsorption of a target agent onto a polymer nanoparticle can make targeted drug delivery system. Examples of functionalized nanoparticles include fluorescence molecules, X-ray or MRI contrast imaging agents, to name a few. However, functionalizing nanoparticles may not be as efficient as loading them inside the particle, especially when the change of surface property by the functional molecule is not expected. This loading process can also increase both stability and uptake.

The protein adsorption on polymer nanoparticles has significant importance in biomedical applications both *in-vitr*o and *in-vivo*. *In-vitro* applications include protein separation, solid-phase immunoassay and enzyme immobilization. *In-vivo* applications involve bearing or filler biomaterials and various therapeutic carriers [85]. The adsorption of proteins for controlled drug delivery or drug targeting system is regarded as a major factor influencing *in-vivo* distribution after intravenous injection. Numerous proteins exist in the human body, and their adsorption, denaturation on the surface, and blood clothing are directly involved with overall biocompatibility and performance. Dispersing polymeric nanoparticles in protein mixture gives rise to a phenomenon called Vroman-effect. The adsorption patterns considered as a product of a sequence of adsorption of more abundant proteins with lower affinity are displaced by less abundant proteins with higher affinity in the early stage of adsorption [86].

2.3 Adsorption of Polymeric Nanoparticles on Large Surfaces

In this case, polymeric nanoparticles act as the adsorbate, and particle-surface interaction will determine the adsorption behavior. Contrary to adsorption of functional molecules onto polymer, studies on adsorption of polymeric nanoparticles onto large surfaces are rather limited. However, since adsorption is mainly determined by the interaction between nanoparticle surface and the large surface, understanding the adsorption behavior of polymers may well help us to understand the adsorption behavior of polymeric nanoparticles.

Polymer adsorption in general and biopolymer adsorption in particular show a range of binding energies depending on the type of forces present at the interface.

Hydrogen bonding and electrostatic interactions are very common in polymer adsorption. If the polymer consists of more than one block, and those blocks have different interactions with the surface. For example, during the course of adsorption of poly(ethylene oxide)-block-poly(L-lysine) copolymer (PEO-b-PLL) adsorption onto silica surface, PEO can bind with silica by hydrogen bonding, while PLL can bind via electrostatic interactions [87]. In these cases, two blocks competitively adsorb onto the surface. At low concentrations, both blocks bind with the surface, whereas at high concentration, the block possessing the stronger interaction mainly binds with the surface. Moreover, the block with weaker interaction will be replaced by the block with stronger interaction as the concentration increases.

The adsorption of polymers onto surfaces is found to take place via two processes at different time scales: (i) a diffusion-limited process in the initial stage, and (ii) a significantly slower process at dense surface coverage. This happens because the interaction between the polymer increases with increasing surface coverage. At initial stage, the surface coverage is low and the repulsive force from the pre-adsorbed polymer is ignored. In addition, the adsorption rate is determined by the polymer concentration in the solution/surface interface. However, at high surface coverage, interactions between polymers are strong, and therefore adsorbed polymers on the surface have to rearrange to a more brushy conformation for more polymers to adsorb [88, 89] .

The adsorption behavior of polymeric nanoparticles may be similar to the adsorption behavior of polymers, since the surface (a polymer) property of the nanoparticle plays an important role in the adsorption behavior. However, the particle

size and the shape may also influence the adsorption behavior, i.e. the particle size and the sharp affect the van der Waals interactions, Born interactions, electrical double-layer interactions and other interactions that occur between the particle and the surface. The difference in these interactions will result in a different the adsorption behavior.

Similar to the adsorption of polymer onto surfaces, the adsorption of polymeric nanoparticles may also take place via two kinetics regimes at different times. Initially, the adsorption rate is limited by the nanoparticles availability at the solution/surface interface. At high surface coverage, the adsorption sites become scarce, and repulsion between the similarly charged nanoparticles increases, thus presenting a potential barrier to adsorption. The slower polymeric nanoparticle surface rearrangement is necessary for further attachment, which becomes the rate-determining step. The maximum amount adsorbed at this stage is thought to be kinetically determined, which accounts for the reported irreversible adsorption [90].

2.4 Adsorption Isotherms

In general, multi-layer adsorption is not applicable due to the repulsive interaction between polymeric nanoparticles. Therefore, the pattern of polymeric adsorption equilibrium isotherms assumes either a Langmuir-type or Freundlich-type shape. The Langmuir-type model is described by

$$\Gamma = \frac{\Gamma_{max} C_{eq}}{b + C_{eq}} \qquad [2.1]$$

where C_{eq} is the equilibrium concentration, Γ is the absorb mass of the polymeric nanoparticle, Γ_{max} is the plateau value and b is a constant. Langmuir-type model is based on the assumption that the adsorption enthalpy does not vary with coverage. Langmuir-

type isotherm shows a steep initial slope followed by attainment of a plateau at high concentration. While the Freundlich model is described by

$$\Gamma = a(C_{eq})^m \quad [2.2]$$

where a and m are constants that define the functionality of Γ and C_{eq}. Freundich model is based on the assumption that the adsorption enthalpy decrease linearly with surface coverage. Freundlich isotherm shows a monitonic increase for all range of concentrations.

Due to the complicated interaction between polymeric nanoparticles, sometimes neither Langmuir model nor Freundlich model is accurate enough, and Langmiur-Freundlich model is used instead and is described by

$$\Gamma = \frac{\Gamma_{max}(C_{eq})^m}{b+(C_{eq})^m} \quad [2.3].$$

Langmuir-type isotherm is more widely used and it is valid for most of adsorption cases.

2.5 Adsorption Kinetics of Polymeric Nanoparticles onto Substrates

Polymeric nanoparticles usually can form strong covalent bonds with surface making a kind of chemisorption. However, these covalent bonds only happen to the adsorbed particle during their rearrangement or deformation. Physical interaction, such as van der Waals interaction, Born interaction, electrical double-layer interaction and so on, still play more important role in the adsorption process. Let us consider a simple system (Fig. 2.1) of a spherical rigid nanoparticle with a flat surface.

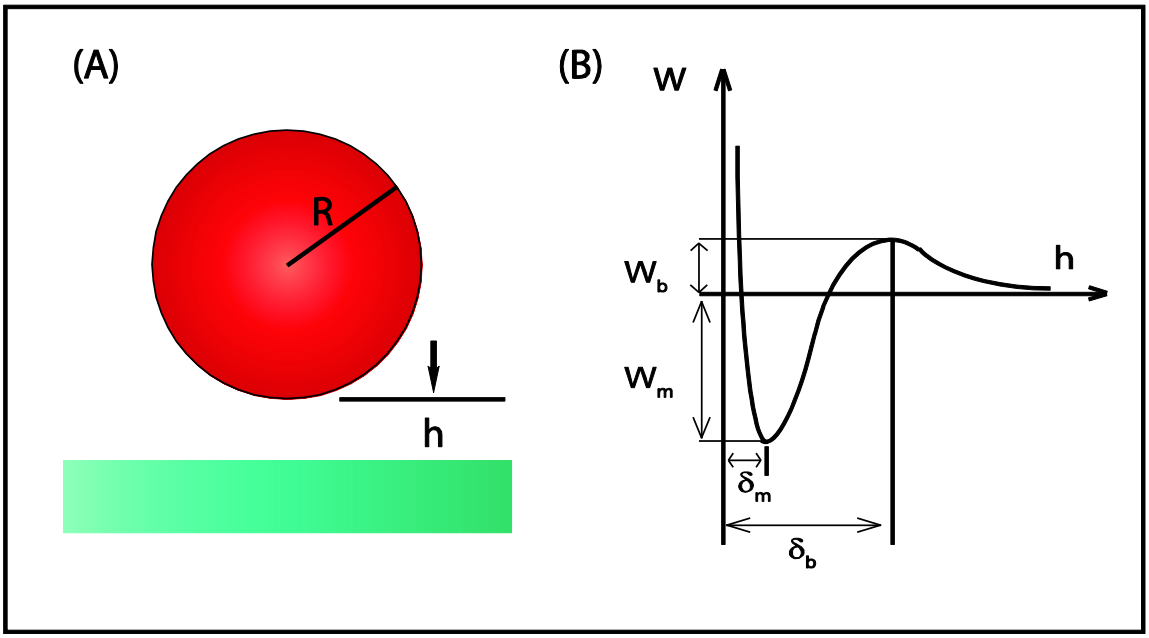

Figure 2.1. (a) Illustration of a simple system of a sphere nanoparticle with flat surface. (b) total interaction energy versus distance.

First, the van der Waals interaction energy between a sphere and a semi-infinite plate can be expressed as [91]:

$$W_{vdw}(h) = -\frac{A}{6}\left[\frac{R}{h} + \frac{R}{h+2R} + ln\frac{h}{h+2R}\right] \quad [2.4]$$

where A is the Hamaker constant.

Second, Born repulsion is a short-range molecular interaction, resulting from the overlap of electron orbitals. It is the twelfth-order term of the empirical Lennard-Jones 6-12 potential. The born repulsion between a sphere and a plate can be calculated using [92]:

$$W_{Born}(h) = \frac{A\sigma^6}{7560}\left[\frac{h+8R}{(h+2R)^7} + \frac{6R-h}{h^7}\right] \quad [2.5]$$

where σ is the collision diameter.

Third, the double-layer interaction between a sphere and a plate can be expressed as [93]:

$$W_{DL}(h) = 16\epsilon(\frac{kT}{e})^2 R \times tanh(\frac{e\varphi_{s1}}{4kT}) \times tanh(\frac{e\varphi_{s1}}{4kT}) e^{-\kappa h} \quad [2.6]$$

where ε is fluid dielectric constant of the medium, θ_{s1} and θ_{s2} are surface potential of the polymer nanoparticle and flate surface, κ^{-1} is Debye length. This expression is appropriate for monovalent electrolyte solutions when $\kappa h > 2$ and $\kappa R >> 1$. For low surface potential (θ_{s1}, θ_{s2} <50 mV), the follow equation may also be used [94].

$$W_{DL}(h) = 16\epsilon R \times \varphi_{s1} \times \varphi_{s2} \times e^{-\kappa h} \quad [2.7]$$

Summing the contribution from each effect (Equation 2.4, 2.5, 2.6 or 2.7) gives the total energy of interaction:

$$W(h) = W_{vdw}(h) + W_{Born}(h) + W_{DL}(h) \quad [2.8]$$

To calculate the adsorption kinetic, the equation of continuity for dispersed nanoparticles phase under isobaric-isothermal conditions in the form [95]:

$$\frac{\partial n}{\partial t} + \nabla \cdot \boldsymbol{j} = 0 \quad [2.9]$$

$$\boldsymbol{j} = -\boldsymbol{D_c} \cdot \left(\frac{\Delta\mu}{kT} + \frac{\Delta W_t}{kT}\right) n + \boldsymbol{U_p}.n \quad [2.10]$$

where j is the particle flux vector, D_c is diffusion tensor, $D_c = MkT$, M is the mobility tensor, μ is the chemical potential of particles, W_t is the total interaction potential, n is the local value of particle concentration, U_p is the particle velocity vector. For the region close to the interface of thickness (δ_a) where the flow contributions vanishes and the particle transport can be assumed to be one-dimensional, Equations 2.9 and 2.10 simplify into [85]:

$$\frac{\partial n}{\partial t} = \frac{\partial}{\partial h}\left[D(h)e^{-W/kT}\frac{\partial}{\partial h}\left(ne^{W/kT}\right)\right] \quad [2.11].$$

For linear adsorption regime, the flux can be expressed as follows [82]:

$$-j = k_a n(\delta_a) + k'_d n(\delta_m) \quad [2.12]$$

where $n(\delta_a)$ is the particle concentration at $h=\delta_a$, $n(\delta_m)$ is the particle concentration at the primary minimum,

$$k_a = \frac{e^{W(\delta_a)/kT}}{\int_{\delta_m}^{\delta_a}\frac{e^{W/kT}}{D(h)}dh} \quad [2.13]$$

$$k'_d = k_a e^{(W(\delta_m)-W(\delta_a))/kT} \quad [2.14]$$

By considering the surface coverage definition given by Equation 2.15 and $W(\delta_a)=0$ (no secondary minimum present), one can transform Equation 2.14 to the usual form as Equation 2.18 [85]:

$$\Gamma = \int_0^{\delta_a} n(\delta)dh \quad [2.15]$$

$$-j = k_a n(\delta_a) + k_d \Gamma(\delta_m) \quad [2.16]$$

where

$$k_a = \frac{1}{\int_{\delta_m}^{\delta}\frac{e^{W/kT}}{D(h)}dh} \quad [2.17]$$

$$k_d = \frac{k_a}{\int_{\delta_m}^{\delta} e^{-W/kT}dh} \quad [2.18]$$

The theoretic adsorption rate constant and desorption rate constant can be calculated by Equations 2.17 and 2.18.

CHAPTER III

ADSORPTION, DESORPTION, AND REMOVAL OF POLYMERIC NANOMEDICINE ON AND FROM CELLULOSE SURFACES*

3.1 Introduction

With the increasing consumption of nanomedicine and a lack of regulation governing their disposal, the occurrence and fate of medicines in the environment and the potential consequences for human health have been increasingly recognized as issues warranting consideration[3, 4, 96, 97]. Currently, among the various types of nanomedicine, polymeric nanoparticulate drug delivery systems (PNDDS) filled with therapeutic agents represent one of the most commonly used forms of drug delivery [8-12].

PNDDS released into soils and sediments may eventually find their way into groundwater, reservoirs, and river systems and, thereby, may enter into the food chains of living organisms [81, 98, 99]. To be able to properly assess the distribution and fate of PNDDS and develop successful strategies for minimizing any side effects on the environment, one has to understand how PNDDS interacts and adsorbs on environmental interfaces. In general, cellulose is the most abundant component of plant roots [100] and therefore important in the context of determining how PNDDS may accumulate on the plant roots, which can be consumed by animals or affect symbiotic relationships with

---

*Reproduced with permission from Adsorption, Desorption, and Removal of Polymeric Nanomedicine on and from Cellulose Surfaces: Effect of Size by Ming Zhang and Mustafa Akbulut, 2011. *Langmuir*, 27 (20), pp.12550-12559, Copyright 2011 by American Chemical Society.

fungi and bacteria.

Thus, in this study, we focus on the adsorption and desorption behavior of a model PNDDS on cellulose surfaces. The model PNDDS was ibuprofen loaded poly(ethyleneglycol-b-ε-caprolactone) (PEG-b-PCL) encapsulated nanoparticles of various sizes. PEG-b-PCL was selected as stabilizing building block because it is one of the most commonly used amphiphilic copolymer in formulations of the current PNDDS [101-104]. Ibuprofen is opted due to its low water solubility, which is a common feature of most therapeutics used in PNDDS formulations. Quartz crystal microbalance with dissipation (QCM-D) was employed to study the adsorption and desorption kinetics and thermodynamics of these PNDDS onto cellulose surfaces. We also used atomic force microscopy (AFM) to obtain complementary information on adsorption and desorption behavior of PNDDS.

3.2 Materials and Methods

3.2.1 Materials

Poly(ethyleneglycol-b-ε-caprolactone) (PEO-b-PCL, 5,000-b-6,500 g/mol) (Polymer Source Inc.), polystyrene (PS, 125,000 g/mol) (Alfa Aesar), ibuprofen (≥98%)(Sigma-Aldrich), and tetrahydrofuran (THF) (Sigma-Aldrich) were used as received.

3.2.2 Preparation of PNDDS

The PNDDS were prepared using a rapid nanoprecipitation method [105, 106].In this method, a hydrophobic therapeutic agent, ibuprofen, and an amphiphilic diblock copolymer, PEG-b-PCL, were molecularly dissolved in a water-miscible, organic phase,

THF. The mixture was loaded in a glass syringe. Add another glass syringe loaded an aqueous anti-solvent stream, Milli-Q water. These two syringes were connected to a three-way micro-mixer. Two syringe pumps were introduced to control the flow rates of organic and water phases. The flow rates of organic and water phases were 5 ml/min and 50 ml/min, respectively. These two flows were rapidly mixed to produce polymer encapsulated ibuprofen nanoparticles (Figure 3.1). The resultant dispersion was dialyzed against Milli-Q water overnight to completely remove THF with a standard regenerated cellulose dialysis membrane (12 kD-14 kD, Spectrum Laboratories, Inc.). The sizes of these nanoparticles were tuned by varying the concentration of ibuprofen and/or adding an extra filler agent, PS in the organic stream (Table 3.1).

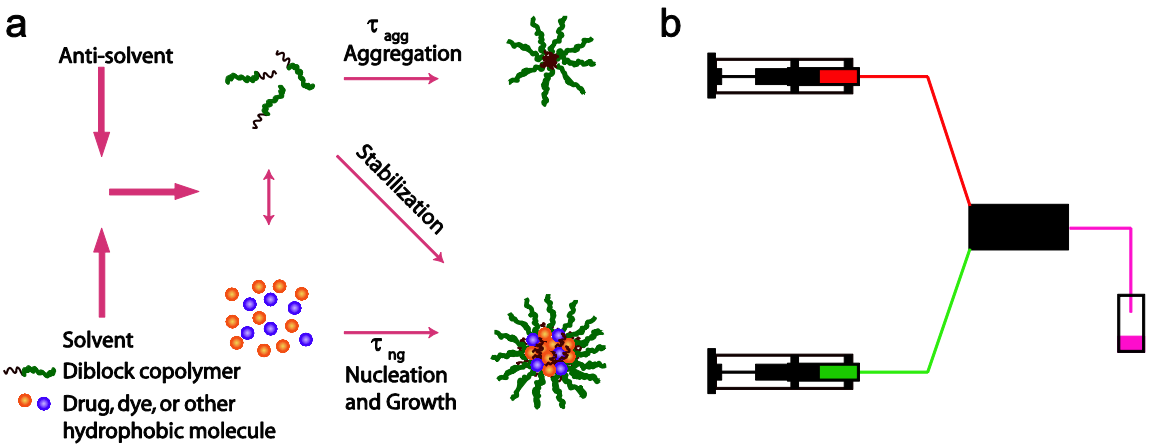

Figure 3.1 Schematic (a) theory, and (b) experiment setup of Flash NanoPrecipitation Method to Fabricate PNDDS

Table 3.1. Six different formulations used to create ibuprofen nanoparticles of varying size.

Formulation	Ibuprofen	PEO-b-PCL	PS
A	1.0%	2.0%	-
B	0.2%	0.2%	-
C	0.1%	0.1%	0.02%
D	0.1%	0.1%	0.05%
E	0.1%	0.1%	0.10%
F	0.1%	0.1%	0.20%

*The concentrations werein weight % (weight agent/weight THF) in THF stream before mixing with Milli-Q water at a 1:10 THF:H_2O (vol:vol) ratio. All formulations also contains very trace amount of Nile-Red (~10^{-3}%) for potential use in distribution of nanoparticles by fluorescence imaging.

3.2.3 Characterization of PNDDS

Dynamic light scattering (DLS) (Zetasizer Nano ZS90, Malvern) was used to measure the size and zeta potentials of PNDDS. At least three measurements were acquired by each of sample. Transmission electron microscopy (TEM) (JEM-2010, Jeol) was used to characterize the shape and size. A drop of PNDDS sample solution was added on a carbon film (CF-400-Cu, Electron Microscopy Sciences) and dried in room temperature. The images were got by a Gatan SC1000 ORIUS CCD camera (Model 832) at room temperature.

3.2.4 Quartz Crystal Microbalance with Dissipation (QCM-D)

The adsorption and desorption of PNDDS onto the cellulose surface were studied using a QCM-D (E1, Biolin Scientific) and a cellulose-coated QCM sensor (QSX 334, Biolin Scientific). In these experiments, upon interaction of PNDDS with the surface of the sensor crystal, changes in the resonance frequency, *f*, related to attached mass (including coupled water) in the adlayer is measured with a time resolution of better than 1 s. Measurement data for *f* was acquired at several harmonics (15, 25, 35, 45, 55, and 65

MHz) simultaneously. All measurements were performed at a temperature of 25°C, to within 0.1 °C. The liquid flow rate was very low, 3 μl/s and kept constant for all experiments. For all types of PNDDS, the concentration was 0.133mg/ml. In a typical experiment, first, a base line was obtained using Milli-Q water (18.2 MΩ cm^{-1} @ 25 °C). Then, Milli-Q water was replaced by PNDDS solutions to initiate and measure the adsorption of PNDSS on the cellulose surface. After the equilibrium was reached, PNDDS solution was replaced by Milli Q water to study the desorption behavior of PNDDS from cellulose surfaces. Each QCM experiment was repeated at least four to five times.

3.2.5 Atomic Force Microscopy (AFM)

The distribution of PNDDS on the cellulose surface after adsorption and desorption steps were characterized by AFM in contact mode (NanoscopeIIIa, Veeco Instruments, Santa Barbara, CA). The AFM measurements were conducted using a standard V-shaped SiN_4 probe (Veeco, Santa Barbara) with a spring constant of 6 N/m and tip radius of less than 20 nm. AFM measurements were performed at a 0˚ scan angle on a 10-μm×10-μm area at a speed of 1 μm/s.

3.3 Results

3.3.1 Characterization of Prepared Model PNDDS

Figure 3.2a displays the intensity-weighted particle size distribution for six different sizes of PNDDS prepared bytheformulations described in Table 3.1.All of the size distributions were unimodal and fairly narrow. The particle size measurements were also confirmed by transmission electron microscopy (TEM) (Fig. 3.2b and 3.2c). TEM

images also indicated that PNDDS were perfectly spherical and had a core-shell structure. For all PNDDS, the Zeta potential was found to be 30±3 mV, an indication of moderate electrostatic stabilization. Additional DLS measurements performed in pre-defined intervals over two weeks revealed that there was no significant change in the PNDDS size over a period of two weeks, suggesting an excellent stability in an aqueous environment at 25°C and pH 6.7.

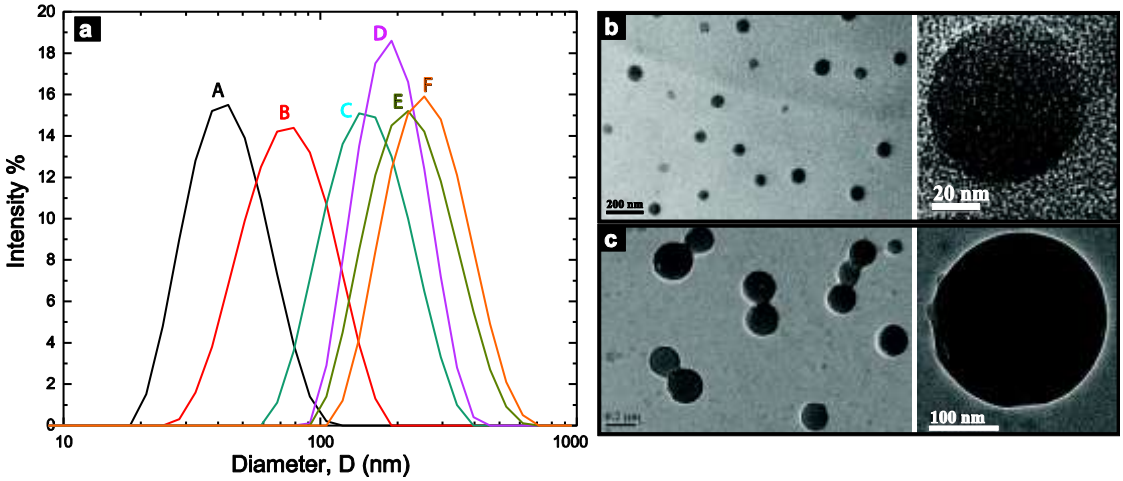

Figure 3.2. (a) The intensity-weighted particle size distributions for PNDDS. Z-average sizes of PNDDS were 46±1 nm (black, A), 81±2 nm (red, B), 159±1 nm (cyan, C), 197±4 nm (magenta, D), 238±7 nm (dark yellow, E), and 271±2 nm (orange, F). TEM micrographs for (b) 46-nm PNDDS and (c) 271-nm PNDDS described in DLS study. (Letters A through F shown in the particle size distribution graph indicate the formulation used (Table 2.1 in their preparation.)

3.3.2 Adsorption Kinetics and Thermodynamics of PNDSS on Cellulose Surface

Figure 3.3 shows a typical mass adsorption and desorption of PNDDS of various sizes on the cellulose surface as a function of time. For all sizes, both of the adsorption and desorption data followed an exponential trend, suggesting that the adsorption and desorption of PNDDS on the cellulose surface is a first-order process. In addition, it was found that during PNDDS exposure (adsorption stage, t_1), the time required to reach

steady-state increased with increasing PNDDS size (Fig. 3.3b). Furthermore, the adlayer mass under steady-state condition was about the same, 605±19 ng/cm^2 for all PNDDS. On the other hand, during rinsing (desorption stage, t_2), the time required to reach steady-state counter-intuitively increased with decreasing PNDDS size (Fig. 3.3c). Furthermore, while the complete removal/desorption was not observed for any sizes, a larger fraction of adlayer mass desorbed from the surface for smaller PNNDS. In other words, the adsorption of PNDDS on cellulose is partially reversible process. Overall, Figure 3.3 contains a lot of information, which we analyze and discuss in detail in the following paragraphs.

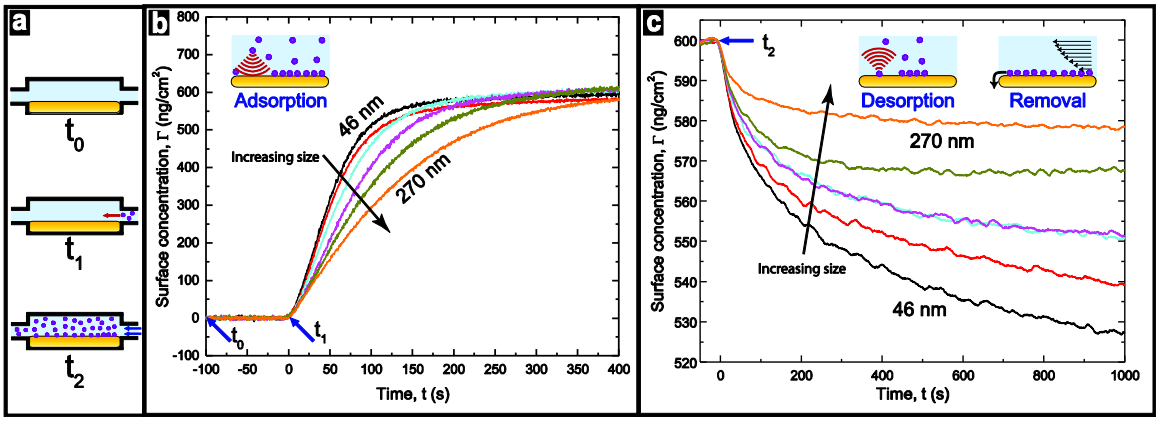

Figure 3.3. (a) Illustration of three different stages of QCM experiments involving a cellulose sensor and PNDDS: water exposure (t_0), PNDDS dispersion exposure (t_1), and water rinsing (t_2). Corresponding QCM response (b) for exposure step and (c) for the rinsing step.Z-average sizes of PNDDS were 46±1 nm (black), 81±2 nm (red), 159±1 nm (cyan), 197±4 nm (magenta), 238±7 nm (dark yellow), and 271±2 nm (orange).

3.3.3 Distribution of PNDDS on Cellulose Surface before and after Rinsing

Figure 3.4 displays AFM micrographs of cellulose QCM sensors before and after exposure of 197-nm PNDDS, and after water rinsing. As observed from QCM experiments, some of PNDDS (purple) remained on the cellulose, suggesting a partially

reversible adsorption behavior. The size analysis of PNDDS revealed that the height of adsorbed PNDDS, 150±20 nm is smaller than the diameter of the PNDDS in solution while the length and width of adsorbed PNDDS are 230±130 nm. Overall, although there are some deformations on the PNDDS upon adsorption, the volume of PNDDS is mostly preserved. This finding also means that PNDDS are stable against mechanical deformations as well i.e. they do not break down upon adsorption.

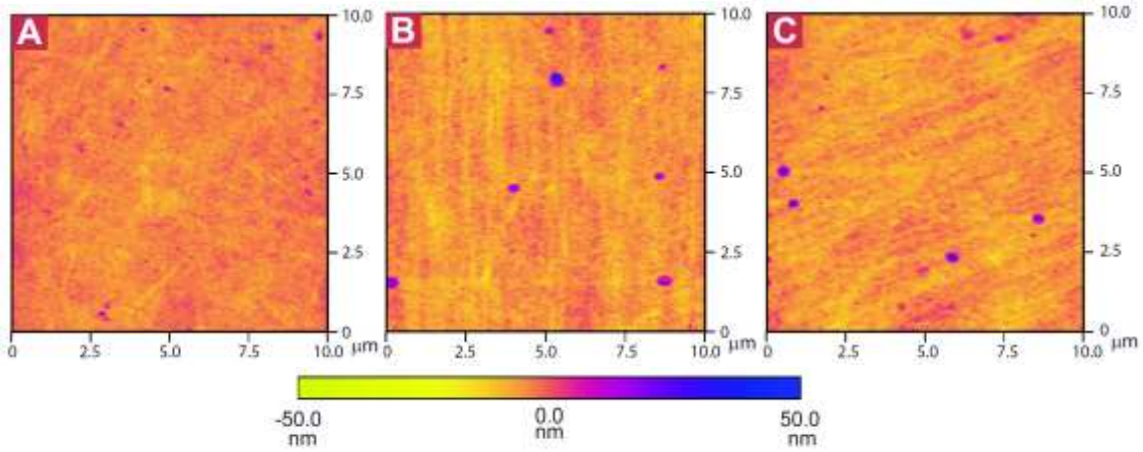

Figure 3.4. AFM micrographs of the cellulose QCM sensor (a) before PNDDS adsorption, (b) after PNDDS adsorption, and (c) after water rinsing.

3.3.4 Kinetic Models for PNDDS Adsorption and Desorption

To describe the kinetics of adsorption and desorption of PNDDS on cellulose surfaces, we relied on partially reversible adsorption model reported by Tassel *et al.*[107]:

$$\frac{\partial \Gamma_\alpha}{\partial t} = k_a m_s \Phi_\alpha(t) - k_d \Gamma_\alpha(t) - k_s \Gamma_\alpha(t) \Psi_{\alpha\beta}(t) \quad [3.1]$$

$$\frac{\partial \Gamma_\beta}{\partial t} = k_s \Gamma_\alpha(t) \Psi_{\alpha\beta}(t) \quad [3.2]$$

Here Γ_α and Γ_β are the concentration α-particles (reversibly bound particles) and β-particles (irreversibly bound particles) on the sensor surface (Fig. 3.5), respectively; m_s is the mass concentration of PNDDS in the solution; k_a is the rate constant of adsorption; k_d is the rate constant of desorption; k_s is the rate constant of spreading; $\Phi_\alpha(t)$ is the probability of an incoming α-particle to land in a non-overlapping site on the surface; and $\Psi_{\alpha\beta}(t)$ is the probability of an α-particle that is already on the surface to have sufficient area to spread.

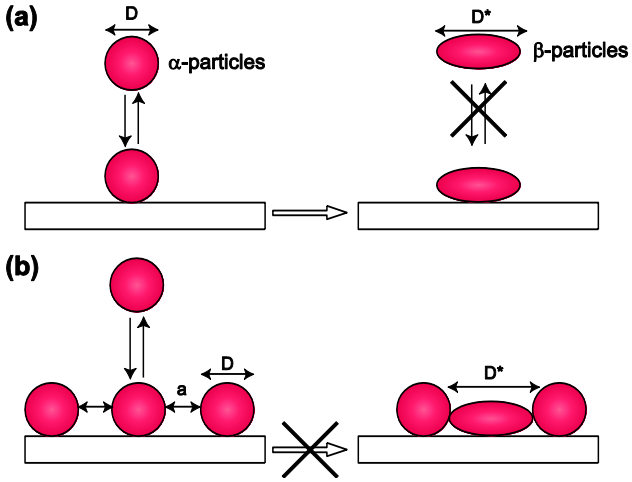

Figure 3.5. A schematic of the partially reversible adsorption model. Adapted from Ref. [107].Adsorption is forbidden if the new particle will overlap or be too close to previously adsorbed particles. Particles may deform and form an irreversible bind with the surface if space allows. Particles may desorb from the surface if no deformation happen but cannot desorb after deformation.

Since QCM measurements can only provide information about the total mass of adlayer, and cannot differentiate between α-particles and β-particles, Eqs. 3.1 and 3.2 are added together to yield the total mass balance on the surface:

$$\frac{d\Gamma}{dt} = k_a m_s \Phi_\alpha(t) - k_d \Gamma_\alpha(t) \qquad [3.3]$$

where Γ is the mass concentration of total PNDDS on the sensor surface. We assume that $\Phi_\alpha(t)$ is directly proportional with the empty space available for new particles to

adsorb on *i.e.* a Langmuir-type adsorption behavior for α-particles. This assumption implies that $\Phi_\alpha(t)=(\Gamma^*-\Gamma)/\Gamma^*$, where Γ^* is the maximum surface concentration of PNDDS that can cover the surface, which is the equilibrium concentration of PNDDS on the sensor surface at very large solution concentrations. For the sake of simplicity, we shall introduce another parameter, θ, which is the ratio of non-deformed to total PNDDS mass on the surface of the sensor ($\theta=\Gamma_\alpha/\Gamma$). Combining all of this information, the rate of mass change on the surface can be expressed during the PNDDS exposure stage as follows:

$$R_{exposure} = \frac{d\Gamma}{dt} = k_a m_s(\Gamma^* - \Gamma)/\Gamma^* - k_d\theta\Gamma \qquad [3.4].$$

Since the inlet stream contains a continuously supplied, constant concentration of PNDDS and the residence time of PNDDS in the chamber is small, m_s can be assumed to be constant. However, θ is a function of time: initially, $\theta_{(t=0)}=0$ which means that all PNDDS have enough space to deform on the surface, and at very long adsorption times, $\theta_{(t=\infty)}=\theta_\infty$, which means that there is no more space for any PNDDS to deform on the cellulose surface. If change in the total area occupied by PNDDS is small relative to the overall surface area during the adsorption experiment, an arithmetic average of $\theta_{(t=\infty)}$ and $\theta_{(t=0)}$, $\langle\theta\rangle$(independent of time) may be used instead of θ. This approximation leads to the following expression for Γ:

$$\Gamma = \frac{k_a m_s \Gamma^*}{k_a m_s + \Gamma^* k_d\langle\theta\rangle} + c_1 e^{-(k_a m_s/\Gamma^* + k_d\langle\theta\rangle)t} \qquad [3.5]$$

Fitting the QCM data shown in Fig. 3.3b with Eq. 3.5 enabled us to calculate kinetic parameters and surface coverage for each size of PNDDS (Table 3.2). The

equilibrium concentration of adsorbed PNDDS, $\Gamma_\infty = \frac{k_a m_s \Gamma^*}{k_a m_s + \Gamma^* k_d <\theta>}$, was found to mostly independent of PNDDS size, 609±19 ng/cm^2 as can also directly be seen from Figure 3.3. The surface coverage for smaller particles was more than that for larger ones; and ranged from 0.21 to 0.038. The corresponding average interparticle distances (from center to center) ranged from 89 nm to 1229 nm.

Table 3.2. Summary of the fitting parameters for the QCM data based on Eq. 3.5 for PNDDS exposure stage.

Diameter (nm)	$k_a m_s/\Gamma^* + k_d <\theta>$ (10^{-3}/s)	**Coverage (fraction)**	**Interparticle distance (nm)**
46	13.8±0.9	0.210±0.012	89±5
81	12.6±0.3	0.121±0.006	207±10
159	11.3±2.0	0.066±0.002	550±19
197	11.1±1.0	0.052±0.003	766±50
238	7.5±0.5	0.043±0.001	1015±31
271	5.2±0.4	0.038±0.002	1229±66

For the case of pure water inflow over the sensor, rinsing stage, the equilibrium shifted towards desorption and the adsorbed mass on the sensor decreased exponentially. However, as discussed in the previous sections, only the PNDDS that have not deformed on the surface (α-particles) can desorb from the sensor. Thus, during the rinsing stage, the change in the mass of adsorbed particles was primarily due to desorption of α-particles. For this system, the rate of mass change on the surface can be expressed as:

$$R_{rinsing} = -\frac{d\Gamma_\alpha}{dt} = k_d \Gamma_\alpha \qquad [3.6]$$

The solution for this equation is:

$$\Gamma_\alpha = C_2 e^{-k_d t} \qquad [3.7]$$

Fitting the QCM desorption data shown in Figure 3.3c with the model described in Eq.3.7 enabled us to determine the rate constant of desorption and the ratio of non-deformed to total PNDDS mass on the surface at equilibrium (Table 3.3). It was found that the rate constant of desorption was smaller for smaller PNDDS and ranged from 2.5×10^{-3} to $11.9\times10^{-3}s^{-1}$. It was found that a larger fraction of smaller PNDDS was in undeformed-state (α-particles) compared to larger PNDDS. This is presumably related to the fact that the larger particles had a larger equilibrium interparticle distance on the surface: The average interparticle distance of 46-nm PNDDS was about twice of its diameter, while that of 271-nm PNDDS was about 4.5 times of its diameter. This means that there is a smaller degree of steric hindrance that can laterally inhibit the deformation of PNDDS i.e. transformation from α-particles to β-particles (Fig. 3.5).

Table 3.3. Summary of the fitting parameters for the QCM data based on Eq. 2.7 for rinsing stage.

Diameter (nm)	$\Gamma_{\alpha\infty}$(ng/cm^2)	θ_∞	k_d(10^{-3}/s)
46	54±14	0.09±0.02	2.5±0.1
81	53±6	0.09±0.01	3.4±0.1
159	51±2	0.08±0.004	3.9±0.1
197	48±3	0.07±0.007	4.6±0.1
238	35±1	0.06±0.002	9.2±0.3
271	20±3	0.03±0.005	11.9±0.7

After k_d and $\langle\theta\rangle$ are found, we can calculate k_a since we have already determined $k_a m_s/\Gamma^* + k_d\langle\theta\rangle$ and $\Gamma_\infty = \frac{k_a m_s \Gamma^*}{k_a m_s + \Gamma^* k_d \langle\theta\rangle}$ from the adsorption data (Table 3.2). For $\langle\theta\rangle$, we considered two limiting cases (t=0 and t=∞) for all PNDDS sizes, and found that the difference in k_a obtained using $\theta_{(t=0)}$ and $\theta_{(t=\infty)}$ is smaller than 7% for all of the cases.

Thus, such as small variation of k_a with respect to time and θconfirms the validity of our assumption to use an arithmetic average of $\theta_{(t=0)}$ and $\theta_{(t=\infty)}$for $<\theta>$.With this assumption, the adsorption rate constants were determined and shown in Figure 3.6. The rate constant of adsorption decreased with increasing PNDDS size while the rate constant of desorption increased with increasing PNDDS size.

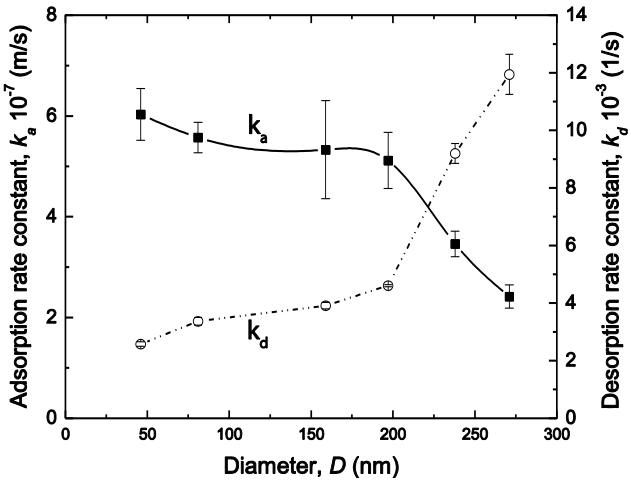

Figure 3.6. The measured adsorption and desorption rate constant of PNDDS as a function PNDDS diameter.

3.4 Discussion

3.4.1 Degree of PNDDS Deformations

The QCM data indicated that a larger fraction of smaller PNDDS was in undeformed-state (α-particles) compared to larger PNDDS. This behavior could be ascribed two phenomena. First, according to the JKR and DMT theories [108], in the absence of any applied load and assuming that the particle is rigid as compared to the substrate, the contact radius varies as the particle radius is raised to the ⅔power if the deformations are elastic. Maugis and Pollock [109] showed that the contact radius should vary with the particle radius to the ½ power if the deformations are plastic.Rimai

et al. [110] studied deformation of polystyrene particles ranging from 2 to 12.5 μm on polished polyurethane (elastic) substrate experimentally, and showed that the contact radius changes with the particle radius raised to the ¾ power. In essence, current particle adhesion studies have predicted that the contact radius should vary with the particle radius to between ½ and ¾ power. Regardless of the model chosen, the contact radius increases with increasing particle size. This means that larger particles have a higher tendency to be in β-state (Fig. 3.5).

The fact that a larger fraction of smaller PNDDS is in undeformed-state may also be related to the interparticle separation (particle spacing). The average interparticle distance of 46-nm PNDDS was about twice of its diameter, while that of 271-nm PNDDS was about 4.5 times of its diameter. This means that there is a smaller degree of steric hindrance for larger particles that can laterally inhibit the deformation of PNDDS i.e. transformation from α-particles to β-particles (Fig. 3.5)

3.4.2 Partially Reversible Adsorption-Desorption Behavior

A possible explanation for the incomplete desorption is that upon adsorption and deformation, the large number of PNDDS segments in the vicinity of the surfaces collectively create a large energy barrier, hindering the simultaneous breakage of all segment−surface contacts and hence prohibiting desorption [111].

Another explanation for the irreversible behavior is as follows: Partially reversible adsorption-desorption behavior is also ultimately an adhesion hysteresis phenomenon where the work needed to separate two surfaces or molecules is generally greater than that originally gained on bringing them together. For surfaces composed of

chain molecules (such as cellulose and polyethylene glycol segments of PNDDS), their adhesion hysteresis is largely determined by the rearrangement or restructuring of surface molecular groups to enhance the number and/or strength of contacting bonds across the interface [112-116] . Involving interactions of two polymers, Maeda *et al.*[117] showed that one or two methylene groups can interdigitate with or penetrate into the opposite surface to increase the number of van der Waals bonds by an order of magnitude. In addition, the degree of interdigitation and entanglement for polymer-polymer junctions is strongly rate-dependent in general [118-120]. Thus, since there is a continuous flow PNDDS at the exposure (deposition stage) and PNDDS is relatively labile on the cellulose surface, the adhesion hysteresis (or incomplete removal of PNDDS) is expected to depend on the relative magnitude of the rate of interdigitation and entanglement with respect to the rate of PNDDS translation on the surface. In essence, those of PNDDS that have sufficient time and/or space to entangle and interdigitate with cellulose surfaces will bind irreversibly to the surface while those that do not have enough time and/or space to entangle and interdigitate will bind to the surface reversibly.

Similar partially reversible adsorption/desorption behaviors were also observed in other soft-condensed matter systems such as copoly (ethylene oxide−propylene oxide−ethylene oxide) on self-assembled monolayer (SAM) of a long-chain alkanethiol ($CH_3(CH_2)_{10}SH$) [111]; annexin A1 binding to solid-supported lipid bilayers [121]; leucine-lysine peptide adsorption and desorption at $–CH_3$ and –COOH terminated

alkylthiolate monolayers [122]; and giant unilamellar vesicles containing STxB lipid receptor onto Globotriaosylceramide [123].

3.4.3 Trends in Adsorption and Desorption Rate Constants

As shown in the Figure 3.6, the rate constant of adsorption decreased with increasing PNDDS size while the rate constant of desorption increased with increasing PNDDS size. To understand the reasons behind this behavior, we consider the intermolecular interactions between PNDDS and the cellulose sensor. When these forces act over distances that are short compared to the diffusion boundary-layer thickness, and when the forces form an energy barrier, the adsorption and desorption rates may be calculated by lumping the effect of the interactions into a boundary condition on the usual convective-diffusion equation [85]. This condition takes the form of a first-order, reversible reaction on the collector's surface.

The rate of adsorption and desorption is related to the total interaction potential, W, as follows [85]:

$$k_a = \frac{1}{\int_{\delta_m}^{\delta} \frac{e^{W/k_B T}}{D_C(h)} dh} \quad [3.8]$$

$$k_d = \frac{k_a}{\int_{\delta_m}^{\delta} e^{-W/k_B T} dh} \quad [3.9]$$

where h is the separation between the particle and surface, k_B Boltzmann constant, T temperature, δ_m is the separation at which there is a primary minimum in the total interaction potential, δ is the diffusion boundary-layer thickness, $D_c(h)$ is the diffusion coefficient given by Nernst-Einstein equation [124]:

$$D_c(h) = \frac{f(\frac{h}{R})}{6\pi\mu R} k_B T \quad [3.10]$$

The wall correlation function *f(h/R)* tends to *h/R* when *h/R* <<1 and unity(*i.e.* Stokes–Einstein equation) when *h/R*>>1 where *R* is the particle radius. For simple shape of the specific interaction energy profile, one can estimate k_a and k_d analytically. In the case when energy distributions around the primary minimum and the barrier region can be approximated by a parabolic distribution, these constants are given by [85]

$$k_a \cong \frac{D_{c,\infty}}{R} \sqrt{\frac{W_b}{2\pi k_B T}} \times e^{-\frac{W_b}{k_B T}} \quad [3.11]$$

$$k_d \cong \frac{k_a}{\delta_m} \sqrt{\frac{-W_m}{\pi k_B T}} \times e^{\frac{W_m}{k_B T}} \quad [3.12]$$

where, W_b is the interaction energy at $h = \delta_b$, where is the maximum energy barrier; W_m is the interaction energy at $h = \delta_m$. There are three important types of interactions between PNDDS and cellulose surface that plays a role in the adsorption and desorption behavior: attractive van der Waals interaction, Born repulsion, and electrical double-layer repulsion.

First, the van der Waals interaction energy between a spherical particle and a semi-infinite plate can be expressed as [91]:

$$W_{vdw}(h) = -\frac{A}{6}\left[\frac{R}{h} + \frac{R}{h+2R} + ln\frac{h}{h+2R}\right] \quad [3.13]$$

where *A* is the Hamaker constant, which typically ranges between 10^{-21} to 10^{-20} J for organic molecules in water [125-127]. Considering that the surface tension of PEO (γ_{PEO} =30.7 mJ/m^2) and cellulose ($\gamma_{cellulose}$ =31.8 mJ/m^2) are relatively close to one another [125, 128], the Hamaker constant of PEO-water-cellulose interface, $A_{PEO\text{-}water\text{-}cellulose}$ has

to be close to the Hamaker constant of cellulose-water-cellulose interface, $A_{\text{cellulose-water-cellulose}}$. Thus, in all relevant calculations, we used the latter Hamaker constant, $A_{\text{cellulose-water-cellulose}}$, which was experimentally measured to be 8.0×10^{-21} J by Bergstrom *et al.* [126].

Second, Born repulsion is a short-range molecular interaction, resulting from the overlap of electron orbitals. It is the twelfth-order term of the empirical Lennard-Jones 6-12 potential. The born repulsion between a sphere and a plate can be calculated using [92]:

$$W_{Born}(h) = \frac{A\sigma^6}{7560}\left[\frac{h+8R}{(h+2R)^7} + \frac{6R-h}{h^7}\right] \quad [3.14]$$

where σ is the collision diameter, which is treated as a second characteristic property of the particles and typically has a value of the order of 0.5 to 0.9 nm [127].

Third, when a surface come in contact with polar solvents, such as water, an electrostatic charge can develop by dissociation of surface groups or by adsorption of charged molecules such as polyelectrolyte from the surrounding solution. Such effects give rise to the double-layer interaction between the opposing surfaces, which, for a sphere and a plate, can be expressed as follows [94]:

$$W_{DL}(h) = \varepsilon R \times \psi_{s1} \times \psi_{s2} \times e^{-\kappa h} \quad [3.15]$$

Where ε is the dielectric constant of the medium, ψ_{s1} and ψ_{s2} are surface potential of the PNDDS and cellulose surface, respectively, and κ^{-1} is Debye length. This equation is valid for small surface potential ($|\psi_{s1}|,|\psi_{s2}|$<50 mV).

Summing the contribution from each effect gives the total energy of interaction:

$$W(h)=W_{VDW}(h)+W_{Born}(h)+W_{DL}(h) \quad [3.16]$$

Equation 16 involves one attractive and two repulsive terms, and can have single or multiple extrema depending on the relative magnitude and range of each interaction term. For PNDDS used in the QCM experiments, we calculated the total energy as a function of separation and observed that there are only one minimum and one maximum in the total interaction energy. This is because van der Waals attraction is stronger than double-layer and weaker than Born repulsion at short separation (below 0.3 nm) while the van der Waals attraction is weaker than double-layer repulsion and stronger than Born repulsion at large separations (above 20 nm). The minima was located at around 0.4 nm (Fig. 3.7a), which is close to the collision diameter while the maxima is located at around 50-75 nm depending on the size of particles (Fig. 3.7b). In addition, it was found that amplitudes of the minima and maxima were nearly proportional to particle radius.

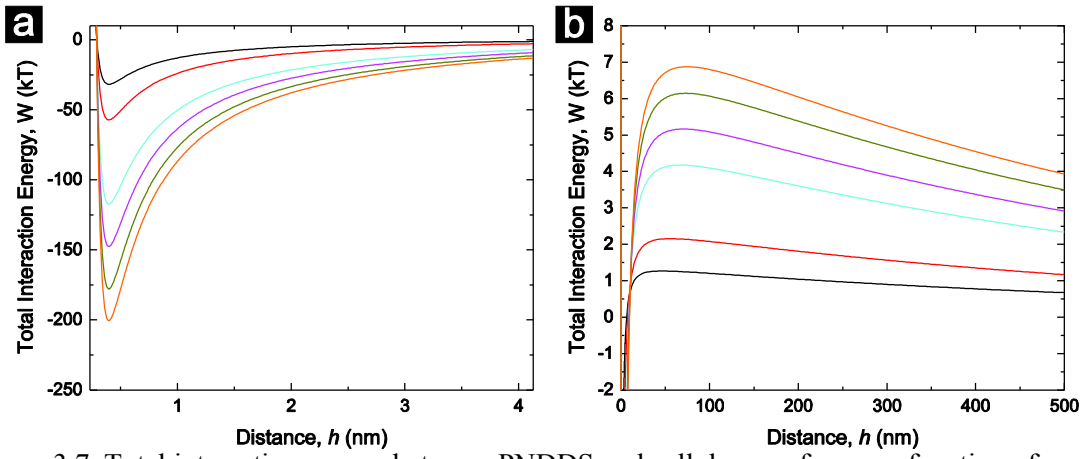

Figure 3.7. Total interaction energy between PNDDS and cellulose surface as a function of distance for PNDDS of various sizes.(black line: 46nm, red line: 81 nm, cyan line: 159nm, magenta line: 197nm, dark yellow: 238nm, and orange: 271 nm.)

Table 3.4. List of the theoretical and experimental adsorption and desorption rate constants for PNDDS ranging from 46-nm to 271-nm. The theoretical constants are calculated using Eqs. 2.11 and 2.12 with a cut-off distance, δ_m= 0.4 nm; A=0.8×10^{-20} J; ζ=7×10^{-10} m; k_BT=4.1×10^{-21} J; ε_r=78.38; θ_{s1} = -12mV[126]; θ_{s2} = -30mV; κ^{-1} = 680 nm; and μ=0.001 N·s·m^{-2} for all particle sizes.

Diameter	**Theoretical Results**		**Experiment Results**	
(nm)	k_a(m/s)	k_d(1/s)	k_a(m/s)	k_d(1/s)
46	7.35E-5	8.87E-9	6.03E-7	2.58E-3
81	1.27E-5	1.90E-20	5.57E-7	3.37E-3
159	6.09E-7	9.13E-18	5.33E-7	3.91E-3
197	1.64E-7	2.11E-25	5.12E-7	4.61E-3
238	4.60E-8	4.82E-31	3.46E-7	9.20E-3
271	1.81E-8	2.83E-35	2.42E-7	11.94E-3

With the knowledge of the total energy of interaction, Eqs.3.11 and 3.12 allow us to estimate k_a and k_d (Table 3.4). The estimated and experimental k_a values followed similar trends, suggesting that a simplified model for the interactions is sufficient to capture the basic trends of PNDDS adsorption to cellulose surfaces. Since the adsorption rate constant has the Arrhenius form and the apparent activation energy is nearly proportional to particle radius (Fig. 3.7), k_a decreased roughly exponentially with increasing particle radius. However, it is also worth to underline that small errors in the interaction energy are greatly enhanced due to the exponential dependence of k_a to the interaction energy. To obtain more accurate estimates of k_a values, a number of additional effects, such as surface roughness, solvation of surface, and adlayer particle-particle interactions can be incorporated into the model.

While the theoretical and experimental k_a values followed similar trends, the theoretical and experimental k_d values were very different from one another and even followed an opposite trend with respect to size (Table 3.4). This finding suggests that

forces other than intermolecular forces govern the "desorption" of PNDDS from cellulose surface. Considering there is a flow field passing parallel to surface, hydrodynamic forces can be responsible for the "desorption" or removal of PNDDS from the cellulose surface. It is important to note that while intermolecular forces between PNDDS and cellulose surface act perpendicular to surface, hydrodynamic forces acts both parallel (drag force) and perpendicular (lift force) to the surface (Fig. 3.8).

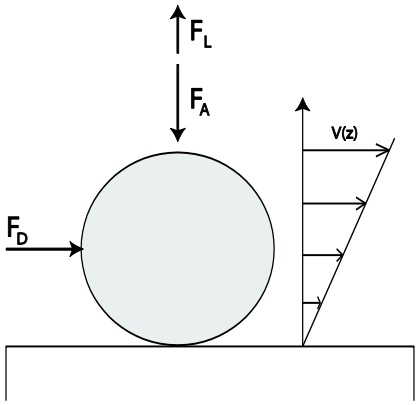

Figure 3.8. Illustration of hydrodynamic and adhesive forces acting on a particle resting on a plate in the presence of flow field.

To determine the relative importance of hydrodynamic and intermolecular forces acting on a PNDDS adsorbed on the cellulose surface, we calculated the lift and adhesion forces acting on PNDDS for the conditions used in our experiments. The lift force acting on a spherical particle resting on a plane can be calculated as described by Leighton and Acrivos [129]:

$$F_L = 0.576\rho D^4 (\frac{\partial V}{\partial z})^2 \qquad [3.17]$$

where V is the fluid velocity as a function of position, $\partial V/\partial z$ is the shear rate, D is the particle diameter, and ρ is the fluid density. The adhesion force between the particle and surface can be calculated using van der Waals interaction at a cut-off distance of 0.16 nm (direct contact separation):

$$F_A = F_V = \frac{AD}{12h^2} \quad [3.18]$$

These calculations reveal that hydrodynamic lift force (F_L~10^{-22} N) is much smaller than adhesion force (F_A~10^{-9} N). Thus, the contribution of lift force into the desorption process is minimal. On the other hand, the drag force acts parallel to surfaces *i.e.* orthogonal to intermolecular forces. Thus, although the drag force is small compared to the intermolecular forces, it can still move the particle parallel to the surface given that the drag force is larger than frictional forces and rolling resistance, $F_D \geq \chi F_A$ [130–133]. Here, χ is the coefficient of static friction or the rolling resistance coefficient depending on the type of motion the particle experiencing (spherical particles can slide and/or roll on the cellulose surface). In most practical applications, the rolling resistance coefficient ranges from 10^{-3} to 10^{-5} [134]. In addition, Knothe and Miedler [135] have shown that if an elastic cylinder is rolling on a plane of the same material, there is no rolling resistance. Thus, we expect that the rolling resistance of PNDDS on cellulose would be negligibly small and the undeformed PNDDS can be removed from the cellulose surface via a hydrodynamics-induced rolling mechanism. For such a removal process, the mass of the particle removed from the sensor per unit time is equal to the product of the particle velocity (at the center of mass) (V_P), the particle surface

concentration (Γ), the length of the sensor that is orthogonal to the flow direction (b), and the inverse of the total area of the sensor ($1/S$):

$$\frac{d\Gamma}{dt} = -\frac{V_p b \Gamma}{S} \quad [3.19]$$

Comparison of Eq. 3.19 with Eq.3.6 suggests that the effective rate constant of desorption (removal) is $k_d = V_p b/S$. The velocity of particle depends on the hydrodynamics of the flow field in which the particles are dispersed. To get a rough idea about the particle velocity, let us assume that the particles are initially at rest on the cellulose surface. The drag force acting on such a particle can be calculated using the following equation [136]:

$$F_D = 1.7009 \cdot 3\pi\mu D V_c \quad [3.20]$$

where μ is the fluid viscosity and V_c is the fluid velocity at the center of the particle. According to the Newton's second law, acceleration is equal to the ratio of applied force to mass. Thus, we can obtain the following expression between the particle and fluid velocities:

$$\frac{dV_p}{dt} = \frac{F_D}{\frac{1}{6}\pi D^3 \rho} = \frac{1.7009 \cdot 18\mu}{\rho D^2}(V_c - V_p) \quad [3.21]$$

Integration of Eq. 3.21 gives rise to an exponential relationship between the particle velocity and time:

$$V_p = V_c\left(1 - e^{-\frac{1.7009 \cdot 18\mu}{\rho D^2}t}\right) \quad [3.22]$$

Eq. 3.22 indicates that a stationary particle reaches 95% the fluid velocity in ~10^{-8} s. Thus, we can safely conclude that the particle velocity is equal to the fluid velocity (at the center of mass of the particle) for all practical purposes. Assuming no slip boundary condition for the fluid, the velocity distribution is:

$$V(z) = 1.5\langle V\rangle\left(\frac{z}{l} - \frac{z^2}{l^2}\right) \quad [3.23]$$

where l is the distance between two walls of the QCM, $\langle V\rangle$ is the velocity averaged over 0 to l. For the complete slip boundary condition for the fluid, the velocity is uniform, $V(z)=\langle V\rangle$. Figure 3.9 displays the effective rate of removal of PNDDS from cellulose surface estimated using two different boundary conditions (full slip and no slip). While the fluid velocity obtained by assuming the full slip boundary condition overestimates the rate of removal, the fluid velocity obtained by no-slip boundary condition underestimates it. This observation suggests that a partial slip boundary condition for the fluid could give rise to a more accurate estimate for the effective rate of removal.

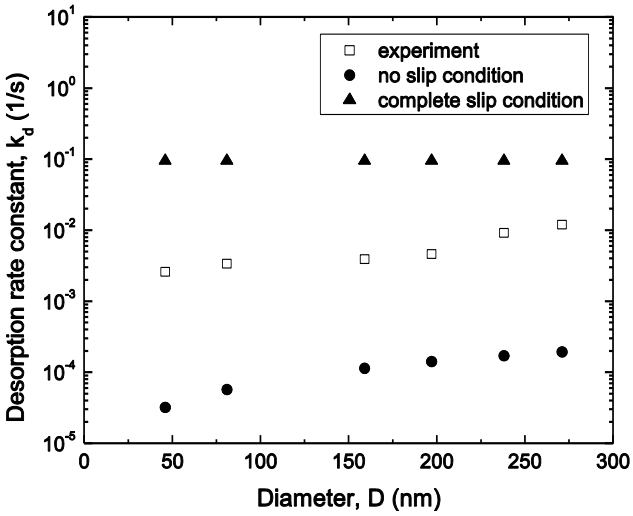

Figure 3.9. Comparison of the experimental and theoretical effective rate of removal values for PNDDS of various sizes from cellulose surfaces.

3.4.4 Environmental Implications

Emerging PNDDS are predominantly loaded with hydrophobic therapeutics such as paclitaxel [13-15], docetaxel [16, 17], cisplatin [18-20], etoposide [15], fluorouracil

[21-23], and estradiol [24, 25]. Recent ecotoxicity studies on *Daphnia magna* have revealed that cisplatin, fluorouracil, and estradiol belong among the compounds that are highly toxic for aquatic organisms (EC50 < 1 mg/L), paclitaxel and doxorubicin are considered toxic (EC50 ranging 1-10 mg/L), and etoposide is harmful to aquatic organisms (10-100 mg/L) [26-28]. Other ecotoxicity studies on *Pseudomonas putida* have indicated similar trends of acute ecotoxicity associated with cisplatin and fluorouracil [28]. In this study, we showed that if a nanomedicine spill is to occur and to approach to the proximity of a cellulosic surface, some fraction of the nanomedicine can irreversibly adsorb on the cellulosic surface. Considering this finding as well as the potential ecotoxicity of nanomedicine, we can claim that a nanomedicine spill can permanently contaminate cellulosic surfaces of plants, which may later be consumed by animals or affect symbiotic relationships with fungi and bacteria, *i.e.* causing ecotoxic effects.

3.5 Conclusion

We have investigated the adsorption, desorption, and removal of behavior of a model polymeric nanomedicine of various sizes on and from cellulose. This study shows that most of the adsorbate PNDDS do not desorb from the cellulose surface even upon rinsing with a large amount of water *i.e.* the adsorption process is only partially reversible. The irreversibility is attributed to the interdigitation and entanglement of PNDDS segments and D-glucose chains of cellulose. In addition, the rate constant of adsorption decreases with increasing PNDDS size. This trend is ultimately related to the activation energy of absorption, which is, at first approximation, linearly proportional to

the PNDDS size. The theoretical k_a calculations relying on attractive van der Waals interaction, Born repulsion, and electrical double-layer repulsion give a fairly accurate estimates for the measured k_a values. In addition, it is shown that hydrodynamic forces acting parallel to the surfaces (orthogonal to the intermolecular forces) are of great importance in the context of PNDDS dynamics near the cellulose wall, and ultimately responsible for the removal of PNDDS via rolling or sliding. As the particle size increases, the removal rates of the particles increased for a given hydrodynamic condition.

CHAPTER IV

UPTAKE AND TRANSLOCATION OF POLYMERIC NANOPARTICULATE DRUG DELIVERY SYSTEMS INTO RYEGRASS*

4.1 Introduction

In recent years, rapid advances in science and technology have opened up the burgeoning new field of nanotechnology, bringing a myriad of opportunities and possibilities for development and fabrication of novel materials and nanodevices. Polymeric nanoparticulate drug delivery systems (PNDDS) filled with therapeutic agents represent one of the most commonly used forms of nanomedicine due to their special properties as mentioned in Chapter I. With the increasing production and consumption of nanotherapeutics, their occurrence, fate, and impaction in the environment have been increasingly recognized as issues warranting consideration [3, 4, 137-141].

Because most PNDDS are loaded with therapeutic materials that are ecotoxic, nanomedicine is an environmental concern. This concern is exacerbated by recent in vivo studies indicating that some of the intravenously administered nanomedicine can be excreted from the body intact through kidney or as metabolite through the liver/bile duct [29-32]. Engineered nanoparticles released to wastewater and wastewater sludge may find their way to food chain [35-37]. Thus, transport of PNDDS in the environment needs to be studied to predict the fate and potential environmental destination of PNDDS

---

in case of uncontrolled releases and accidental spill.

In previous chapter we studied the adsorption, desorption, and removal of behavior of a model polymeric nanomedicine of various sizes on and from cellulose. It is found that most of the adsorbate PNDDS do not desorb from the cellulose surface. In addition, it is shown that hydrodynamic forces acting parallel to the surfaces (orthogonal to the intermolecular forces) are of great importance in the context of PNDDS dynamics near the cellulose wall, and ultimately responsible for the removal of PNDDS via rolling or sliding. Since cellulose is the main component of plant root, whether PNDDS behave similar adsorption on root surface and whether PNDDS can uptake by plants is the next consideration.

Therefore, in this study, we investigate the transport behavior of the same model PNDDS, ibuprofen loaded poly(ethyleneglycol-b-ε-caprolactone) (PEG-b-PCL) encapsulated nanoparticles, in the vicinity of roots of ryegrass (Lolium perenne), which is the first level in the food chain and a common model plant used in the environmental science studies [142, 143]. As we mentioned in previous chapter, PEG-b-PCL was selected as the carrier because it is one of the most popular, FDA approved amphiphilic copolymer used in formulations of the current polymeric drug delivery systems [101, 103]. Ibuprofen is opted as a therapeutic building block due to its low water solubility, which is a shared feature of most therapeutics used in PNDDS formulations [144, 145].

4.2 Materials and Methods

4.2.1 Materials

Poly(ethylene glycol-b-ε-caprolactone) (PEO-b-PCL, 5,000-b-6,500 g/mol,

Polymer Source Inc.), polystyrene (PS, 125,000 g/mol, Alfa Aesar), ibuprofen (≥98%, Sigma-Aldrich), Nile Red (Tokyo Kasei Kogyo co. LTD), and tetrahydrofuran (THF, 99.9%, Sigma-Aldrich) were used as received.

4.2.2 Preparation and Characterization of PNDDS

The PNDDS were prepared using a solution precipitation method [105, 106]. The detail of the method was present in the previous chapter. Shortly, a hydrophobic therapeutic agent (ibuprofen) and an amphiphilic diblock copolymer (PEG-b-PCL) were molecularly dissolved in tetrahydrofuran (THF). The mixture was then very rapidly mixed against a Milli-Q water stream to produce polymer encapsulated ibuprofen nanoparticles. The flow rates of organic and water streams were 5 ml/min and 50 ml/min, respectively. The resultant dispersion was dialyzed overnight to completely remove THF. The sizes of these nanoparticles were adjusted by varying the concentration of ibuprofen and/or adding an extra filler agent (PS) in the organic stream (Table 4.1). In addition, 0.001% wt. of Nile red was introduced into THF stream to produce fluorescent PNDDS so that the fluorophore was imbibed in the PNDDS, not on its surface, to ensure that surface chemistry was not altered.

The size distributions and zeta potentials of PNDDS were measured using dynamic light scattering (DLS) (Zetasizer Nano ZS90, Malvern). The morphology of PNDDS was characterized using transmission electron microscopy (TEM) (JEM-2010, Jeol). Detail information of DLS and TEM could also find in Chapter III.

4.2.3 Plant Germination and Exposure of PNDDS to Ryegrass

1 g Perennial ryegrass seeds (Pennington Seed Inc., GA) were germinated in pots

with 200 g soil (Miracle-Gro® Organic Choice®, ScottsMiracle-Gro, OH). After germination and growing for about one week at room temperature, the leaf was typically about 10 cm while the root was approximately 8 cm. At this stage, after gentle washing and removing residual soil from the root, the ryegrass was transferred into vials filled with tap water and kept there for one day. Then the ryegrass was transferred into vials filled with PNDDS of a given size and concentration of 0.133 mg/ml and kept in the vials for a predefined amount of time. Here, it is important to emphasize that only the roots of the ryegrass were exposed to PNDDS. Each experiment was replicated at least three times for statistical reliability. A separate solution of PNDDS without the ryegrass was used as a control experiment to keep track of fluorescence level of PNDDS solution. The other control experiments involved the exposure of the ryegrass to molecular Nile Red in water or just water instead of Nile Red loaded PNDDS in water.

4.2.4 Spectrofluorometry (SFM)

To determine the transport of PNDDS from aqueous media onto and into ryegrass as a function of time, we immersed ryegrass roots to dispersions of PNDDS that are loaded with a trace amount of fluorescent Nile Red for 0 h, 1 h, 3h, 9 h, 27 h, 81 h, and 312 h. Then, we measured the fluorescence intensity of the PNDDS solution using SFM at these predefined intervals. Similarly, a control experiment measuring the fluorescence intensities in the absence of ryegrass root was conducted to determine the variation in fluorescence level with respect to time. All fluorescence measurements were made by a PTI QuantaMaster series spectrofluorometer (Photon Technology International, Inc., NJ, USA) equipped with a PTI LPS-220B lamp, using 1.00 cm

disposable cells. The excitation wavelength was 549 nm, and the corresponding emission spectra ranged from 559 nm to 700 nm.

4.2.5 Confocal Microscopy

A confocal microscope (Leica TCS SP5) was used to determine the distribution of PNDDS on and in the ryegrass by focusing on different planes of ryegrass. The excitation laser wavelength was 543 nm, and the observed wavelength ranged from 560 nm to 650 nm. This range was selected to distinguish the fluorescence signal of chlorophylls (650 nm to 800 nm) from that of Nile Red. Since each PNDDS size had a slightly different fluorescence spectrum, the confocal micrographs of each PNDDS size were normalized with respect to the corresponding fluorescence intensities using ImageJ. PNDDS exposed to molecular Nile Red in water and just water were control groups in confocal microscopy studies.

4.2.6 Scanning Electron Microscopy (SEM)

The grass roots were observed by SEM (JEOL JSM-7500F) to determine the local distribution of PNDDS on the root surface after immersing roots in the PNDDS dispersion and rinsing with an excess amount of water. PNDDS exposed to only water worked as a control group. For both cases, the root was coated with 4-nm Au layer to fulfill the conductivity requirement of SEM.

4.2.7 Cross Sectional TEM

Sections from roots, stems and leaves of treated and control plants were fixed in 2.5% (vol/vol) glutaraldehyde-1.0% (vol/vol) acrolein in 0.1 M HEPES buffer, pH 7.4 for 30 minutes with intermittent vacuum at room temperature. Fixation was terminated

by a 6 min cycle [2 min ON; 2 min OFF; 2 min ON] at 250 watts with intermittent vacuum in a Ted Pella Biowave laboratory microwave (Ted Pella, Inc, Redding, CA) at 20 C. Specimens were then washed three times 1 min at 250 watts in 0.1 M HEPES buffer pH 7.4 followed by post fixation overnight at 4 C in 1 (wt vol) osmium tetroxide in the same buffer. Specimens were then dehydrated in a graded methanol series [5% (vol/vol) steps from 5% to 3 X 100%]. Each dehydration step was done for 1 min at 250 watts with intermittent vacuum. Infiltration and embedding were done in a low viscosity epoxy resin[146]. Ultrathin sections (90-100 nm) were cut on a Reichert Ultracut E ultramicrotome (Leica Microsystems, Inc., Buffalo Grove, IL). These thin sections were imaged in a JEOL 1200EX transmission electron microscope at an accelerating voltage of 100 kV. Samples of the nanoparticles were enrobed in 2% (wt/vol) agarose and then fixed and processed in the same manner that the plant material was handled to determine the influence of fixation method on the nanoparticles.

4.3 Results

4.3.1 Characterization of PNDSS

Table 4.1 summarizes the formulations used in the preparation of PNDDS with varying size and the resultant mean intensity-averaged PNDDS sizes. These formulations gave rise to particle mean intensity-averaged sizes ranging from 46 nm to 271 nm, enabling us to systematically study the effect of PNDDS size on their transport behavior across ryegrass. All of the size distributions were unimodal and fairly narrow (Fig. 4.1a). Transmission electron microscopy (TEM) micrographs indicated that PNDDS were mostly spherical (Fig. 4.1b). Stability studies revealed that there was no

significant change in the particle size (hydrodynamic radius) after over a period of one month or after diluting 10 times, suggesting an excellent stability in water (Fig. 4.1c). However, it is important to underline that the stability of nanoparticles with respect to the hydrodynamic size does not necessarily mean that there is no release of drug out of PNDDS. The release of drug from the core of PNDDS can lead to a more porous PNDDS while maintaining the same hydrodynamic radius. Such a structural change is not usually detected by DLS.

Table 4.1. Experimental conditions used for preparing ibuprofen-loaded PNDDS.

Formulation	Ibuprofen	PEO-b-PCL	PS	Mean size (nm)
A	1.0%	2.0%	-	46±1
B	0.1%	0.1%	-	117±4
C	0.1%	0.1%	0.02%	159±1
D	0.1%	0.1%	0.05%	197±4
E	0.1%	0.1%	0.10%	238±7
F	0.1%	0.1%	0.20%	271±2

The concentrations were in weight % (weight agent/weight THF) in THF stream before mixing with Milli-Q water at a 1:10 THF/H2O (vol/vol) ratio. To enable fluorescence tracking, all formulations also contained 0.001% wt. Nile Red as a fluorescent building block that is imbibed in the PNDDS.

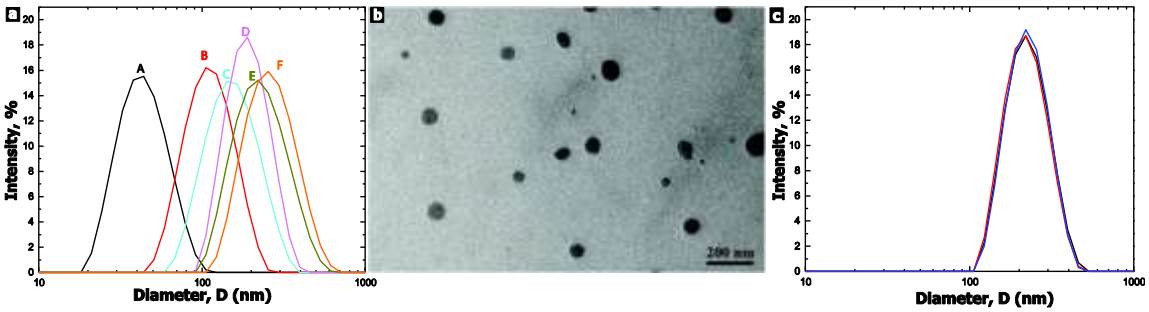

Figure 4.1. (a) Intensity weighted particle size distributions for PNDDS. The mean intensity-averaged sizes of three different batches of PNDDS were 46±1 nm (black, A), 117±4 nm (red, B), 159±1 nm (cyan, C), 197±4 nm (magenta, D), 238±7 nm (dark yellow, E), and 271±2 nm (orange, F). (b) TEM images PNDDS of 46 nm. (c) DLS results of initial 197-nm PNDDS (black), 197-nm PNDDS after diluted 10 times (red), and 197-nm PNDDS after kept for one month (blue). (Letters A-F shown in (a) indicate the formulation used (Table 4.1) in their preparation)

4.3.2 Spectrofluorometry (SFM) Studies

Figure 4.2a shows the emission fluorescence spectra of Nile red-loaded PNDDS of all particle sizes with the excitation wavelength of 549 nm. The spectra had a maximum at a wavelength varying from 610 nm to 640 nm depending on the size of PNDDS. This variation was presumably due to the differences in average intermolecular distances between Nile red molecules for each formulation and the presence of polystyrene molecules.

To determine the relationship between the emission fluorescence maxima and PNDDS concentration, PNDDS of all sizes were diluted into 0.5, 0.25, and 0.1 times their initial concentrations, and their emission maxima were measured by SFM. Figure 4.2b shows the linear fit results of emission maxima of PNDDS versus the concentrations of PNDDS. It shows that the emission maxima are proportional to the concentration of PNDDS of all particle sizes. With these obtained fit equations, the concentrations of PNDDS during uptake experiment for all times were calculated as a function of time.

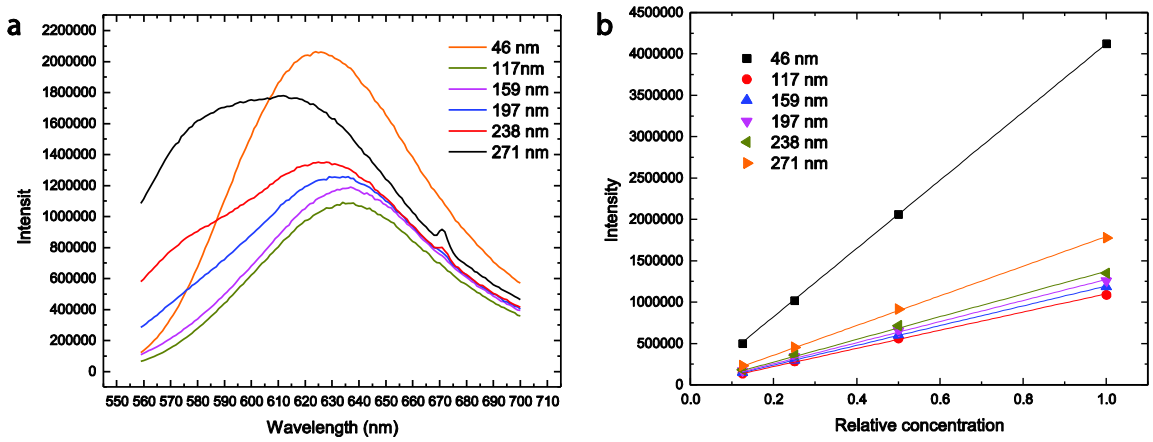

Figure 4.2. (a) Emission fluorescence spectra of PNDDS of different sizes. The emission maxima were recorded at the wavelength varying from 610 nm to 640 nm depending on the formulations used to create PNDDS; (b) Linear fit of the SFM maximum intensity versus concentration of PNDDS. All PNDDS show good linear fit. The fit equation is used to determine the concentration of PNDDS during uptake experiments.

Given that the peak fluorescence intensity was proportional to the concentration of the PNDDS, the analysis of fluorescence intensity data allowed us to calculate the concentration of PNDDS in the solution i.e. PNDDS that is not adsorbed or not uptaken by the roots (Fig. 4.3). It can be clearly seen that the roots consume (adsorb and uptake) the smaller PNDDS much faster. For instance, at t=312 h, relative concentration of 46 nm, 159 nm, and 271 nm PNDDS in the solution was 0.09±0.06, 0.36±0.03 and 0.74±0.08, respectively. This means that 91±6%, 64±3%, and 26±8% of PNDDS were localized in and on the ryegrass for 46 nm, 159 nm, and 271 nm PNDDS, respectively.

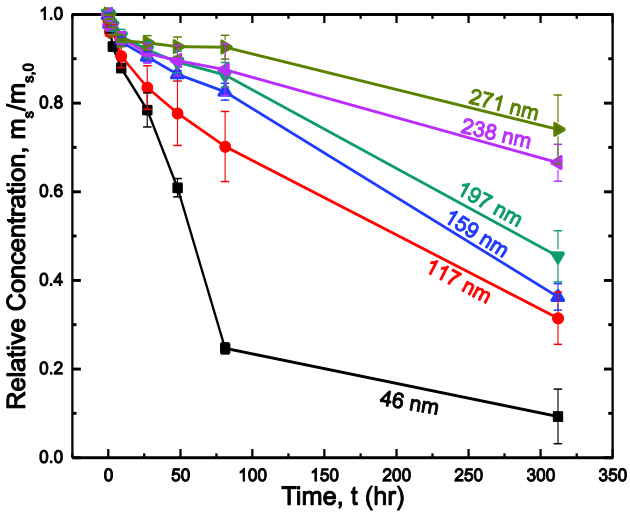

Figure 4.3. The relative concentration, $m_s/m_{s,0}$, (the concentration at any time over the initial concentration) of the PNDDS in the solution (*i.e.* PNDDS that is not adsorbed or not uptaken by the roots) as a function of exposure times for various PNDDS sizes. The data is normalized with respect to the fluorescence intensities of control experiments to account for the variation in fluorescence level with time in the absence of ryegrass roots.

4.3.3 Confocal Microscopy

The ryegrass roots exposed to PNDDS dispersions were also characterized by confocal microscopy to determine the distribution of PNDDS across the ryegrass (Fig. 4.3&4.5). Figure 4.4 displays the confocal microscopy images of roots and leaves upon exposure to 271-nm PNDDS dispersion in water, molecular Nile Red in water, and just water, respectively for 81 hr. These images revealed that while ryegrass can uptake both molecular Nile Red and PNDDS, molecular Nile Red yielded much weaker fluorescence signal, especially in roots. For the case of PNDDS exposure, the fluorescence intensity in the roots was much higher than that in leaves. No fluorescence response was observed for the case of exposure to water only, indicating that there was no chlorophyll-induced interference in fluorescence response for the selected wavelength range.

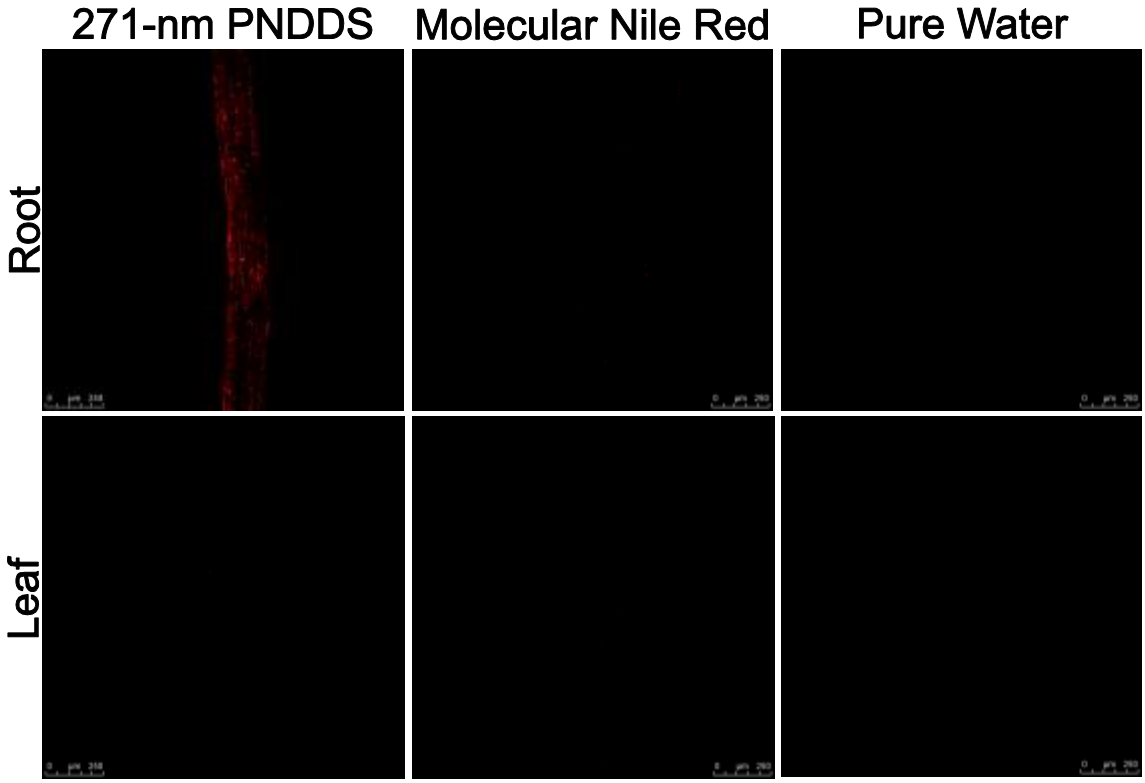

Figure 4.4. Confocal microscope images of ryegrass after exposed to aqueous PNDDS dispersion, molecular Nile Red at maximum solubility in water (saturated solution), and water. The ryegrass exposed to PNDDS shows strong fluorescence signal in root but very weak signal in leaves; the ryegrass exposed to free Nile red shows very weak fluorescence signal in both roots and leaves; and the ryegrass exposed to water show no fluorescence signal.

The difference between the fluorescence behavior of PNDDS and that of molecular Nile Red in the roots can be attributed to the following: First, for a given concentration, the fluorescent intensity of molecular Nile Red in water is 40 times less than that in lipophilic environment [147, 148]. Second, the solubility of Nile Red in water is very poor (less than 1 μg/mL) [149]. Therefore, PNDDS prepared by the formulations described in Table 4.1 can carry higher concentrations of Nile Red to the roots compared to the solubility of Nile Red in water. Considering these points, we can conclude that Nile Red-loaded PNDDS not molecular Nile Red is responsible for the

strong fluorescence response observed in Figure 4.4. Similarities between the fluorescence behavior of leafs that are exposed to PNDDS and molecular Nile Red and that of roots that are exposed to molecular Nile Red may suggest that, for the PNDDS case, only Nile Red molecules that are released from the PNDDS core can reach to the leaves. The fact that the fluorescence intensity of leaves that are exposed to PNDDS did not show any significant variation as a function of PNDDS size also supports this argument.

Figure 4.5 displays the fluorescence images of different part of ryegrass after exposed to PNDDS of different size for 1 hr, 27 hr and 81 hr. These experiments revealed that most of the PNDDS was localized at the root and stem and almost no PNDDS was found at the leaves (Fig. 4.5). Although we only exposed the root of the plant to PNDDS dispersion, the presence of PNDDS in the stem suggests that PNDDS was uptaken by the roots and then transferred into the stem.

The comparison of the local and overall image intensities of the ryegrass revealed that the confocal microscopy results were also self-consistent with the SFM data: At 1 hr, the fluorescence intensities of roots and stems that had been exposed to the PNDDS of varying sizes were not significantly different from each other (Fig. 4.5). On the other hand, at 81 hr, while the stem and root of the ryegrass that was exposed to 46-nm PNDDS had the highest overall fluorescence intensity, the stem and root of the ryegrass that was exposed to 271-nm PNDDS had very weak fluorescence emission intensity for a given excitation intensity.

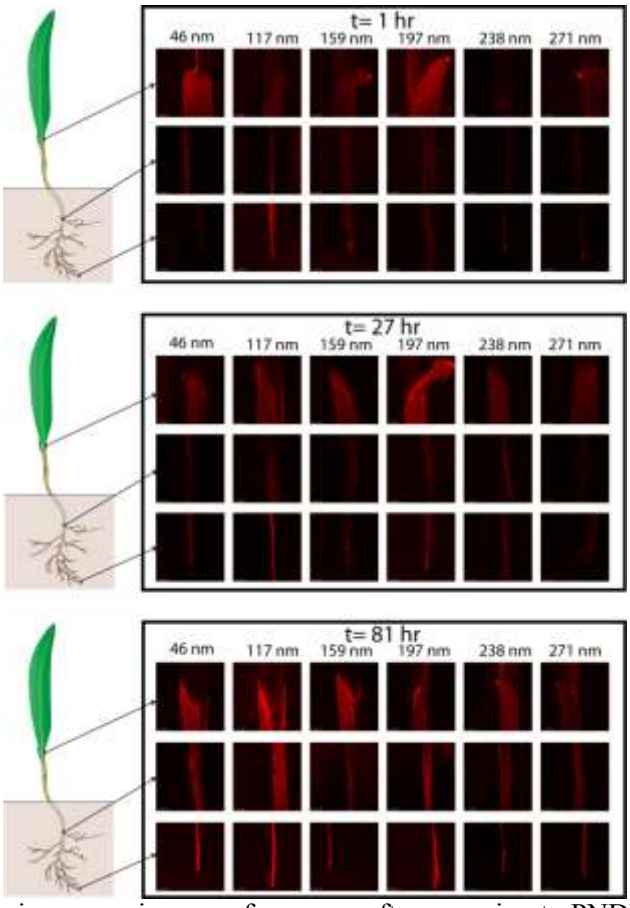

Figure 4.5. Confocal microscope images of ryegrass after exposing to PNDDS (0.133 mg/ml) for 1 hr, 27 hr, and 81 hr. For all times, PNDDS is found in the cap of root, the middle of root and the stem, but not in the leaf. The clear effect of PNDDS size on the uptake of PNDDS into ryegrass can be observed at later times (81 hr). During the acquisition stage, the optical filter is applied to eliminate all wavelength expects a range from 560 nm to 650 nm to distinguish the fluorescence signal of chlorophylls from that of Nile Red tagged PNDDS.

The comparison of fluorescence intensities at root, stem, and leaf revealed that at the beginning, the fluorescence intensities in stems were higher than those in roots. This finding suggests that the rate of PNDDS transport from the root to the stem was initially much faster than the rate of PNDDS uptake from the root surface to root interior. It was also found that as PNDDS accumulated in stems with time, the rate of PNDDS transport from the root to the stem decreased (i.e. the stem was saturated with PNDDS), thereby

PNDDS started to accumulate in roots more.

4.3.4 Scanning Electron Microscope (SEM) Studies

To better understand the uptake mechanism of PNDDS into the plant, we characterized the root surfaces using SEM after exposing them to PNDDS and rinsing them with the excess water (Fig. 4.6). First, it was found that PNDDS had strong interaction with the plant root and was not washed away even with the excess water, while no nanoparticles were found in the control group. This suggests that the adsorption of PNDDS onto the root surface may be an irreversible process. Similar irreversible and partially reversible adsorption behavior on the roots has previously been observed in other systems such as bacteria [150], mineral ions [151], and pesticides [152]. The adsorption of PNDDS may also be irreversible. Second, SEM images suggest that there is some intercellular space that exists between cells (Fig. 4.6b, blue highlight). These openings are known to be responsible for the transport of water and solutes into the root through the apoplast route [153, 154], and presumably enable entry of PNDDS into the ryegrass roots as well.

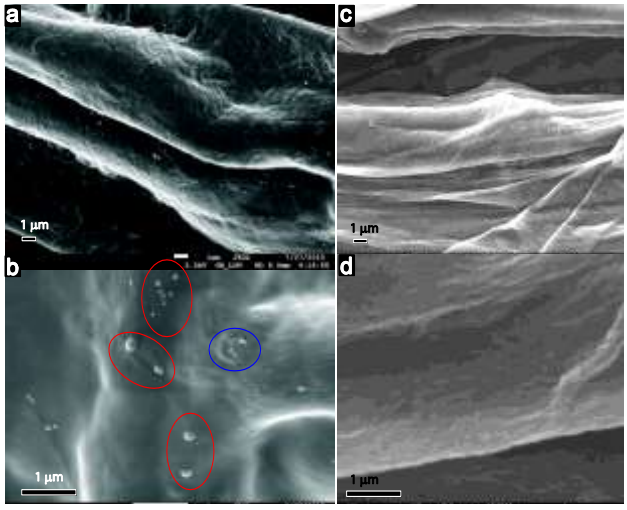

Figure 4.6. (a) Low (×5,000) and (b) high (×20,000) magnification SEM micrographs of the ryegrass root upon exposure to PNDDS of 159 nm solution (0.133 mg/ml). (c) and (d) SEM micrographs of ryegrass root without exposure to PNDDS. There were many PNDDS (red circles) adsorbed on the root even after excess water rinsing. The blue circle indicates a possible PNDDS entry site into the plant. The samples were coated with a 4 nm Au film to enable SEM imaging.

4.3.5 Cross Sectional TEM

Cross sectional TEM was used to independently confirm the uptake of PNDDS into ryegrass root and further study the distribution of PNDDS in the roots. Comparison of the cross sectional TEM images of the roots with and without PNDDS (197-nm) treatment revealed that while the PNDDS treated samples contain some particles (red and green arrows in Fig. 4.7a&b), the control sample had no particles (Fig. 4.7c). The micrographs of PNDDS that underwent the same fixation procedure used for the preparation of roots for cross sectional TEM indicate that the PNDDS were fairly stable against such a procedure (Fig. 4.7d&e). The further analysis of micrographs indicates that the average size of the particles marked with red arrows were 190±30 nm (n>10), very close to the size of PNDDS. These findings suggest that it is indeed possible that ryegrass roots can uptake PNDDS and PNDDS are localized both in root cells and

intercellular space.

It is important to note that in addition to 190 nm particles, there were other particles of 50-100 nm (shown with green arrows). The PNDDS of the smaller size were observed both in PNDDS treated root and PNDDS treated by the agarose gel. We believe that the smaller particles are presumably lightly loaded micelles obtained during the preparation of PNDDS. The existence of smaller particles can be seen from the particle size distributions in Figure 4.1. Alternatively, the microtoming procedure may also break PNDDS into smaller pieces. Therefore, both small and large particles appear in the micrographs.

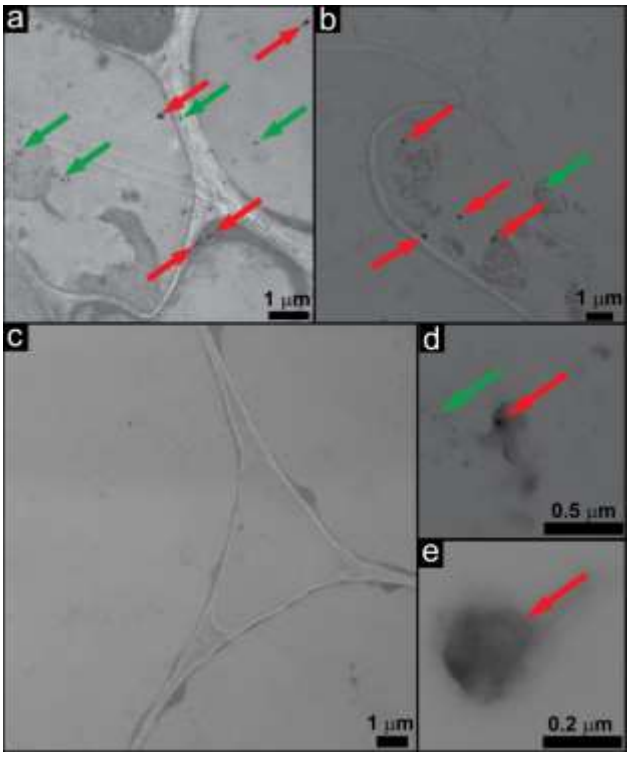

Figure 4.7. Cross sectional TEM images of (a) and (b) the ryegrass root upon exposure to the PNDDS of 197 nm; (c) the ryegrass root in the absence of PNDDS exposure; and (d) and (e) PNDDS that are treated with the agarose gel and microtoming procedure used for the preparation of the roots for the cross sectional TEM.

4.3.6 Kinetics of PNDDS Uptake

Overall transport of PNDDS from solution to a ryegrass can be considered in two processes: (i) adsorption of PNDDS onto the root surface, and (ii) uptake of PNDNS from the root surface to the root interior. Considering the adsorption of PNDDS onto cellulose surface is mostly an irreversible process [155] and SEM images (Fig 4.6) showed that PNDDS was not washed away from root surface, we assume the adsorption of PNDDS onto ryegrass root is irreversible. And the overall process can be expressed as:

$$\mathrm{P+S} \xrightarrow{k_a} \mathrm{P{\bullet}S} \xrightarrow{k_{up}} \mathrm{P^*} + \mathrm{S} \qquad [4.1]$$

where P indicates PNDDS in solution; P•S PNDDS that is bound to root surface; P* PNDDS in root cell; k_a is the adsorption rate constant; and k_{up} the uptake rate constant. In this scheme, the adsorption is assumed to be a Langmuir type, which is widely used in adsorption model for proteins [107, 156, 157], inorganic nanoparticles [158, 159] and polymers [160, 161]. Therefore, the relationship between the concentration of PNDDS in the solution (m_s) and the concentration of PNDDS on the root surface (Γ) is as follows:

$$\frac{V}{S}\frac{dm_s}{dt} = -k_a m_s \theta \qquad [4.2]$$

$$\frac{d\Gamma}{dt} = k_a m_s \theta - k_{up}\Gamma \qquad [4.3]$$

where V is the volume of solution in vials; S is the surface area of root; $\theta=(\Gamma^*-\Gamma)/\Gamma^*$ is the possibility for PNDDS located in empty space on the surface and will not overlap with pre-adsorbed PNDDS; and Γ^* is the maximum surface concentration of PNDDS,

indicating the equilibrium surface concentration when the solution PNDDS concentration is very large. Combination of Eq. 4.2 and 4.3 leads to a second order non-linear differential equation:

$$\Gamma^* \frac{V}{k_a S}\frac{d^2\ln(m_s)}{dt^2} + \frac{V}{S}\left(m_s + \frac{k_{up}\Gamma^*}{k_a}\right)\frac{d\ln(m_s)}{dt} + k_{up}\Gamma^* = 0 \qquad [4.4].$$

The initial conditions for this differential equation, $m_s(t=0)$ is known experimentally and $dm_s(t=0)/dt = -k_a m_s(t=0)\times S/V$. Using a numerical integration technique (Euler method) and the least square method for experimental data within 48 h (See Appendix B1 for further details), we could calculate k_a, k_{up} and Γ^*. However, in this problem, a large number of degrees of freedom exist, creating multiple solutions. Further systematic numerical calculations revealed that only when Γ^* is between 0.4 g/m^2 and 0.8 g/m^2, fits for both k_a and k_{up} yield positive values. Table 4.2 shows the fit results for k_a and k_{up} result when Γ^* = 0.6 g/m^2. Similarly, k_a and k_{up} fit results obtained using Γ^* = 0.4 g/m^2 and 0.8 g/m^2 can be found in Table 4.3 and Table 4.4

Table 4.2. Fit results of k_a, k_{up} and $\Gamma^* k_{up}$. with Γ^* = 0.6.

Diameter (nm)	k_a (m/hr)	k_{up} (1/hr)	$k_a m_{s,0}$ (g/(m^2·hr))	$\Gamma^* k_{up}$ (g/(m^2·hr))
46	0.0041±0.0006	0.169±0.058	0.55±0.08	0.101±0.034
117	0.0030±0.0020	0.099±0.027	0.40±0.24	0.060±0.016
159	0.0020±0.0007	0.051±0.001	0.27±0.09	0.031±0.001
197	0.0013±0.0008	0.039±0.007	0.17±0.10	0.023±0.004
238	0.0027±0.0015	0.031±0.013	0.36±0.19	0.019±0.008
271	0.0022±0.0005	0.014±0.010	0.29±0.06	0.008±0.006

Table 4.3. Fit results of k_a, k_{up} and $\Gamma^* k_{up}$ with $\Gamma^* = 0.8$.

Diameter (nm)	k_a (m/hr)	k_{up} (1/hr)	$k_a m_{s,0}$ (g/(m^2·hr))	$\Gamma^* k_{up}$ (g/(m^2·hr))
46	0.0032±0.0003	0.130±0.048	0.43±0.04	0.078±0.028
117	0.0021±0.0009	0.075±0.023	0.28±0.11	0.045±0.014
159	0.0015±0.0005	0.034±0.002	0.20±0.06	0.021±0.001
197	0.0010±0.0006	0.024±0.006	0.14±0.08	0.014±0.004
238	0.0018±0.0009	0.018±0.011	0.24±0.11	0.011±0.006
271	0.0017±0.0005	0.008±0.005	0.23±0.06	0.005±0.002

Table 4.4. Fit results of k_a, k_{up} and $\Gamma^* k_{up}$ with $\Gamma^* = 0.4$.

Diameter (nm)	k_a (m/hr)	k_{up} (1/hr)	$k_a m_{s,0}$ (g/(m^2·hr))	$\Gamma^* k_{up}$ (g/(m^2·hr))
46	0.024±0.014	0.24±0.08	3.2±1.8	0.14±0.05
117	0.016±0.011	0.15±0.04	2.1±1.5	0.09±0.02
159	0.004±0.002	0.08±0.01	0.5±0.2	0.05±0.01
197	0.002±0.001	0.07±0.01	0.2±0.1	0.04±0.01
238	0.004±0.002	0.06±0.02	0.5±0.3	0.03±0.01
271	0.003±0.001	0.03±0.01	0.4±0.1	0.02±0.01

Overall, regardless of the choice of Γ^* value (in the range of 0.4 to 0.8 g/m^2), k_a and k_{up} gave rise to similar order of magnitudes; and k_{up} increased with decreasing PNDDS size in an exponential manner. While there is mostly an inverse correlation between adsorption rate, k_a, and PNDDS size; k_a for 238-nm and 271-nm PNDDS deviated from this trend presumably due to the increased effect of gravitational forces for larger particles. The relative magnitudes of adsorption flux to uptake flux increased with increasing PNDDS size, indicating that more and more bottlenecking at uptake step will take place as the PNDDS size increases.

4.4 Discussion

Regarding the possible route/mechanism of entry for PNDDS into the ryegrass: lateral roots commonly originate from the pericycle and grow through the cortex of the parent root. Once the lateral root breaks through the outer epidermal layer

to the outside, PNDDS may gain entrance through the resulting crevice (Fig. 4.8).

For nanoparticle transport through root tissue to the xylem system observed in our experiments, there may be two main potential routes: apoplast and symplast routes (Fig. 4.8). The apoplast route involves the space between cells and the cell walls themselves along the radial length corresponding to the root surface (openings at the surface) and the stele (containing the xylem and phloem), whereas the symplast route involves the active uptake or passive uptake of water molecules and ions through the plasma membrane and transfer from cell to cell through the plasmodesmata, which are pores between cells that connect protoplasm and allow transfer of molecules [162-164]. Plasmodesmata have been shown to transport proteins (including transcription factors), short interfering RNA, messenger RNA, and viral genomes from cell to cell [165]. As such, it may also allow the transport of PNDDS. The presence of PNDDS in root cell and intercellular space (Fig. 4.7) reveals that both apoplast and symplast routes may exist in the transport of PNDDS in ryegrass.

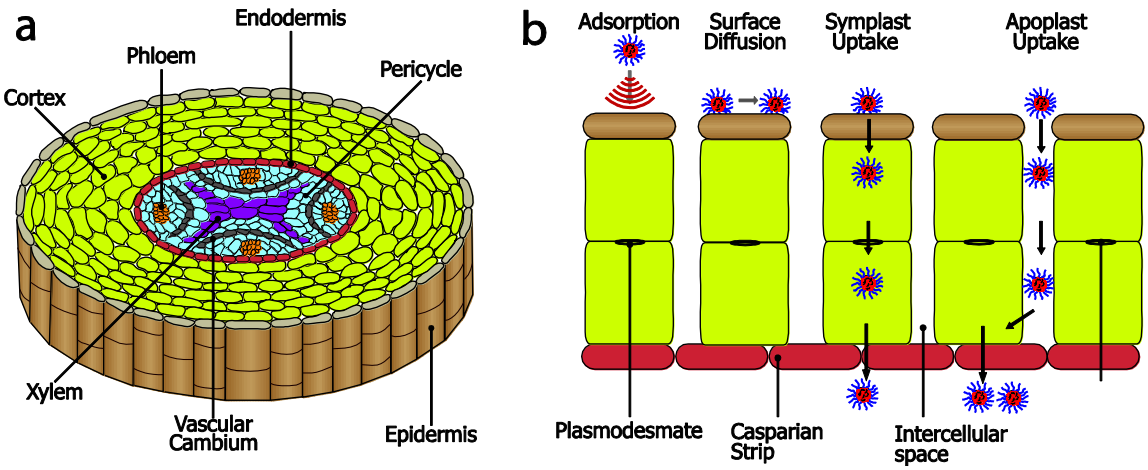

Figure 4.8. (a) Root structure and (b) Possible routes for PNDDS uptake into root

The uptake and accumulation of nanoparticles by plants is increasingly recognized as an important environmental issue by researchers [166-171]. The presence of nanoparticles in stem and roots and absence of nanoparticles in leaves were also observed by Lin *et al*. [168], when they exposed ryegrass (*L.perenne*) to ZnO nanoparticle of size 9-37 nm. ZnO nanoparticles primarily adhered to root surface and individual nanoparticles were observed in the apoplast and protoplast spaces in root endodermis and stele. Zhu *et al*. [169] showed that the exposure of pumpkin (*Cucurbita maxima*) roots to 20 nm iron oxide nanoparticles leads to their major accumulation (45.5% of fed nanoparticles) in the roots and their negligible translocation (0.6% of fed nanoparticles) to the leaves. Lin *et al*. [170] investigated the uptake and translocation of carbon nanomaterials by rice plants (*Oryza sativa*) and found that fullerene C70 of 1.17 nm could be easily taken up by roots and transported to leaves. The differences in the concentration of PNDDS in leaves and roots are presumably due to the selective transport of the membranous ligule, which is located at the inner base of the leaf between where the leaf attaches to the main stem and the stem itself [172-174].

The trend of decreasing uptake rate, k_{up}, with increasing PNDDS size can be explained through the consideration of the mass fluxes of particles or molecules across a porous membrane when the particle size is comparable to the pore size [175]. Similar trends were also observed in other systems: For instance, Nikido and Rosenberg [176] showed that the permeability of the outer membrane of *Escherichia coli* cell to sugars decrease with increasing molecule size. Likewise, the rate internalization of hydrogel particles into HeLa cells was shown to be a strong function of size [177].

Emerging PNDDS are predominantly loaded with hydrophobic therapeutics such as paclitaxel [13-15], docetaxel [16, 17], cisplatin [18-20], etoposide [15], fluorouracil [21-23], and estradiol [24, 25]. Recent ecotoxicity studies on *Daphnia magna* have revealed that cisplatin, fluorouracil, and estradiol belong among the compounds that are highly toxic for aquatic organisms (EC50 < 1 mg/L), paclitaxel and doxorubicin are considered toxic (EC50 ranging 1-10 mg/L), and etoposide is harmful to aquatic organisms (10-100 mg/L) [26-28]. Other ecotoxicity studies on *Pseudomonas putida* have indicated similar trends of acute ecotoxicity associated with cisplatin and fluorouracil [28].

This study suggest that if spill or uncontrolled release of PNDDS is to occur and to expose ryegrass roots to the PNDDS, ryegrass can adsorb and uptake it. This is very important considering that PNDDS on and in the plants may later be consumed by animals and bacteria and accumulated in their bodies, can adversely influence environmental health.

4.5 Conclusions

In summary, this study shows that ryegrass can uptake PNDDS of size ranging from 46 nm to 271 nm through its roots. The rate and fraction of PNDDS uptake by ryegrass roots increased with decreasing size. It is also shown that very small amount of PNDDS, if any, transport from stem to leaf, which is presumably due to the selectivity of membranous ligule. Furthermore, the adsorption step was faster than the uptake step, making the uptake step overall rate determining step for the transport of PNDDS from aqueous media into ryegrass root.

CHAPTER V

ADSORPTION AND REMOVAL DYNAMICS OF POLYMERIC NANOPARTICULATE DRUG DELIVERY SYSTEMS ON SILICA SURFACE*

5.1 Introduction

With the increasing consumption, production, and number of clinical trials of nanomedicines, their occurrence and fate in the environment, and their potential consequences for human health have been increasingly recognized as issues warranting consideration [3, 4, 137-141]. Polymeric nanoparticulate drug delivery systems (PNDDS) filled with therapeutic agents is one of the most commonly used forms of nanomedicine due to their ability to solubilize hydrophobic molecules as well as their increased bioavailability, ability to solubilize hydrophobic molecules, higher payload capacity, excellent stability in aqueous environments and in blood, and prolonged blood circulation time [11, 178-180]. To properly assess the distribution and fate of such nanomedicine and develop successful strategies for minimizing any environmental side effects, a better understanding of interactions between such nanomedicine with environmentally significant surfaces is needed.

In the previous two chapters, adsorption and removal behavior of PNDDS on cellulose surface, as well as uptake and translocation of PNDDS into ryegrass were well studied. It is shown that PNDDS could irreversible adsorb on cellulose surface and root

---

surface. PNDDS could also uptake by ryegrass after adsorbed on root surface. After PNDDS enters into environment via different routes in Chapter I, PNDDS could also expose to other environmental surface such as rocks, soils and/or sands.

This chapter investigates the adsorption and removal behavior of a model PNDDS on and from silica surface. Here, silica is selected as the environmental surface as it constitutes a significant fraction of rocks, soils, and sands [181, 182]. The model PNDDS is levofloxacin loaded poly(ethylene glycol-b-ε-caprolactone) (PEG-b-PCL) nanoparticles. PEG-b-PCL is selected as the drug carrier material because it is one of the most commonly used, Food and Drug Administration (FDA) approved, amphiphilic copolymers in formulations of the current polymeric nanomedicine[183, 184]. Levofloxacin, which is a broad spectrum antibiotic of the fluoroquinolone drug class, is chosen as the therapeutic component because of its low water solubility, which is a common feature of most therapeutics used in polymeric nanomedicine formulations [185, 186]. The adsorption and removal kinetics are studied using QCM-D and AFM. Transport models are developed to describe the adsorption behavior of polymeric nanoparticles in the QCM-D chamber.

5.2 Materials and Methods

5.2.1 Materials

Poly(ethyleneglycol-b-ε-caprolactone) (PEO-b-PCL, 5,000-b-6,500 g/mol) (Polymer Source Inc., Montreal, Canada), polystyrene (PS, 125,000 g/mol) (Alfa Aesar, Ward Hill, MA), levofloxacin (≥98) (Sigma-Aldrich, St. Louis, MO), and tetrahydrofuran (THF, Sigma-Aldrich, St. Louis, MO) were used as received.

5.2.2 Preparation and Characterization of PNDDS

PNDDS was prepared using a rapid precipitation method [105, 187]. Detail information of the method could find in Chapter II. Briefly, Levofloxacin and PEG-b-PCL (an amphiphilic diblock copolymer) were molecularly dissolved in THF. Then, the THF solution was very rapidly mixed with Milli-Q water by a tangential vortex mixer. The flow rates of THF and water streams were 5 ml/min and 50 ml/min, respectively. The resultant nanoparticles were dialyzed overnight to remove the THF. Six different formulations of PNDDS with different concentrations of levofloxacin, polystyrene fillers, and PEG-b-PCL were used to produce PDNNS of systematically varying sizes (Table 5.1). The sizes and zeta potential of PDNNS dispersions were measured using Dynamic Light Scattering (Zetasizer Nano ZS90, Malvern). The morphologies of polymeric nanomedicine were characterized by TEM (JEM-2010, Jeol). The detailed information about DLS and TEM could find in Chapter III.

Table 5.1. Six different formulations used for creating different sizes of Levofloxacin nanomedicine.

Formulation	Levofloxacin	PEO-b-PCL	PS
A	1.0%	2.0%	-
B	0.5%	0.5%	0.02%
C	0.5%	0.5%	0.03%
D	0.5%	0.5%	0.04%
E	0.5%	0.5%	0.10%
F	0.5%	0.5%	0.40%

*The concentrations were in weight % (weight agent/weight THF) in THF stream before mixing with Milli-Q water at a 1:10 THF:H_2O (vol:vol) ratio.

5.2.3 Quartz Crystal Microbalance with Dissipation (QCM-D)

To study the adsorption and removal of PDNNS on and from the silica surface, QCM-D (E1, Biolin Scientific) and silica-coated QCM sensor (QSX 303, Biolin Scientific) were used. The sensor crystal and O-ring that seals the cell/sensor assembly were cleaned as described by Hook and Kasemo [188]. After cleaning and mounting the QCM-D, Milli-Q (18.2 MΩ cm^{-1} @ 25 °C) solution was injected into the chamber, and the system was allowed to equilibrate for at least 0.5 h and then, a base line was obtained. Afterwards, the Milli-Q water was replaced with the PDNNS solution to measure dynamics of PDNNS adsorption on the silica surface (exposure stage). Finally, the PDNNS solution was replaced back with Milli-Q water to study desorption and removal behavior of the PDNNS from the surface (rinsing stage). In all experiments, the concentration of the PDNNS solutions and flow rates were kept constant, 0.5 mg/ml and 2.5 µl s, respectively. All measurements were performed at a temperature of 25°C and at several overtone numbers (n = 3, 5, 7, 9, 11, and 13). Each experiment was repeated at least three times for each PDNNS size (formulation).

The recorded frequency and dissipation curves were evaluated with the QTools software (Biolin Scientific). The adsorbed nanomedicine mass on silica sensor was obtained by applying the Voigt model to Δf and ΔD measured at two overtones (3^{rd} and 5^{th}) [188-190]. The fixed parameters were the solvent density, set to 1000 kg/m3, the solvent viscosity, set to 0.009 Pa·s. This calculation gave rise to the viscoelastic load on the sensor, *i.e.*, the Voigt mass, which is due both adsorbed nanomedicine and water [191].

5.2.4 Atomic Force Microscopy (AFM)

AFM measurements were collected after adsorption equilibrium and rinsing using Dimension Icon AFM (Bruker, Santa Barbara, CA). The AFM measurements were conducted using a tip radius of less than 10nm. Measurements were performed at 0° scan angle at a fix scan rate of 1 Hz. All scans were done in tapping mode.

5.2.5 Computational Analysis of the Flow Behavior

The simulation model described in this paper was constructed using COMSOL Multiphysics v4.2a. The analysis consisted of 3-D laminar flow in the steady state and the QCM-D geometry is shown in Figure 5.8a. Diameter of the chamber was 11.1 mm and the depth was 0.64 mm. Inlet and outlet were 1 mm in diameter and 1 mm in height, and their center points [x, y] were located at [-5, 0] (in mm) and [5, 0] (in mm), respectively. The fluid was water and temperature was 298.15 K. The chamber was divided with a physics-controlled mesh of normal size. No slip boundary condition was used in the simulation. At the inlet, uniform velocity distribution was 3.18×10^{-3} m/s, which was obtained by taking the ratio of the flow rate over inlet area.

5.3 Results and Discussion

5.3.1 Characterization of PNDDS

Figure 5.1a displays the intensity-weighted particle size distribution for six different sizes of PNDDS prepared. The size distributions were fairly unimodal, and their mean value ranged from 90 nm to 305 nm. The PNDDS had a spherical morphology with a core-shell structure (Fig. 5.1b).

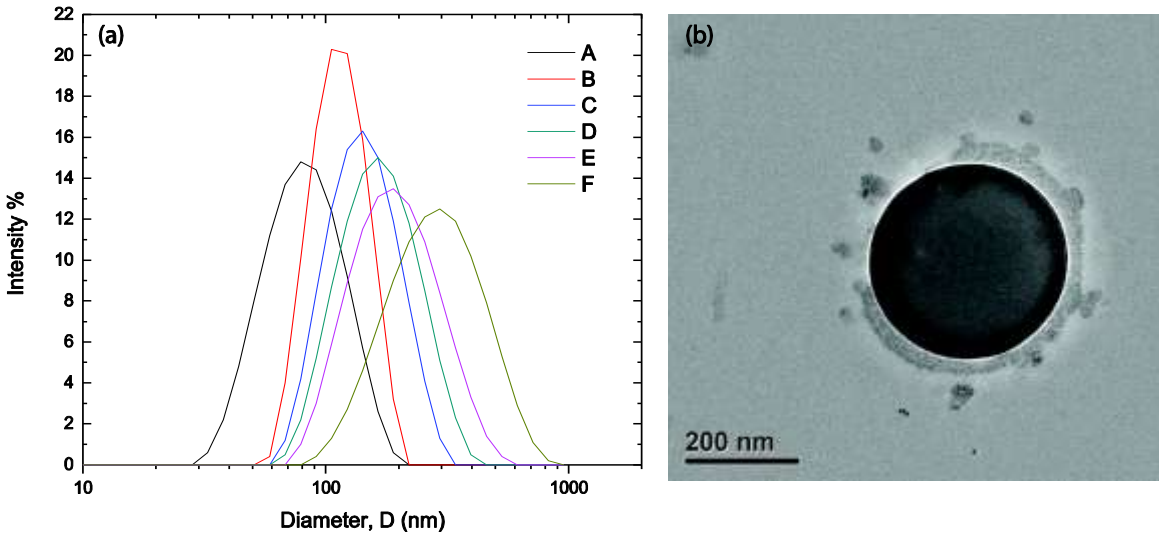

Figure 5.1. (a) Particle size distributions for polymeric nanomedicine. The mean of Z-average sizes of PNDDS were 90 ± 5 nm (black, A), 110 ± 4 nm (red, B), 149 ± 5 nm (blue, C), 174 ± 5 nm (dark cyan, D), 207 ± 6 nm (magenta, E) and 305 ± 7 nm (olive color, F). ± values indicates the standard deviation of different measurements of Z-average values. (b) TEM micrograph of sample F.

Size distribution of particle was also measured after diluting 10 times or stored at 4 °C for 10 days. Figure 5.2 showed size distribution of 305-nm PDNNS at experiment concentration (Day 0), diluting 10 times, and after 10 days. There was no significant change after dilution or 10-days storage at 4 °C, which is different from the stability of unloaded polymeric micelle.

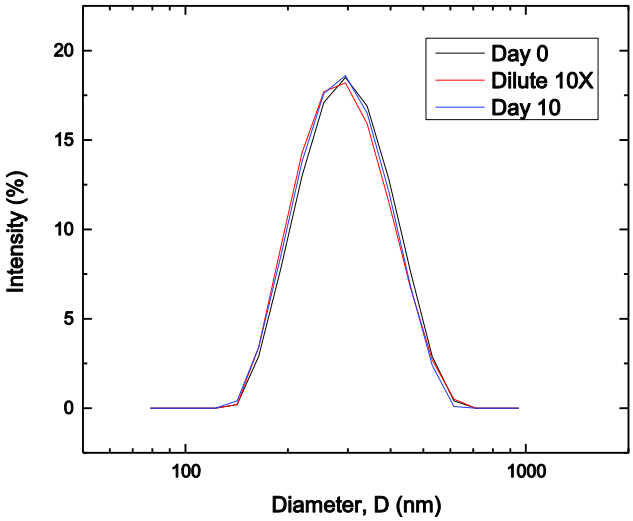

Figure 5.2. Size distribution of 305-nm nanomedicine at Day 0, after diluting 10 times and after storage for 10 days.

The superior stability is attributed to the combination of steric and electrostatic effects [192-194] due to the presence of long PEG chains and the fact that the zeta potential of PEG-PCL based nanomedicine surface ranged from -25 mV to – 30 mV. However, it is significant to note that the stability of nanoparticles with respect to the hydrodynamic size does not necessarily mean that there is no release of drug out of PNDDS [195]. The release of drug from the core of polymer nanoparticles can lead to more porous polymer nanoparticles while maintaining the same hydrodynamic radius. Such a structural change cannot always be detected by DLS.

5.3.2 Adsorption Behavior of PNDDS on Silica Surfaces

Figure 5.3 shows the frequency and dissipation shifts measured for 3rd overtone as a function of time for PNDDS of varying sizes during adsorption stage and the calculated Voigt mass as function of time obtained using 3rd and 5th overtones. Voigt model was selected because it is suitable for soft viscoelastic adsorbed layers and it has

commonly used in studies on adsorption of bacteria [196], proteins [197-199], DNA [200-202], and polymer/copolymers [203-206]. As expected, the frequency decreased with increasing time and eventually reached a plateau (Fig. 5.3a). This trend indicates that there is an increasing amount of PNDDS adsorbed on the silica surfaces with increasing time and eventually reaching an equilibrium (steady-state) surface concentration. For all sizes of PNDDS, the frequency shifts followed an exponential trend (R^2>0.89), which suggests a first-order adsorption kinetic. In other word, adsorption rate was linear to the concentration of PNDDS in bulk solution. The exponential time constant mostly increased with decreasing size.

The energy dissipation increased with increasing time or increasing amount of PNDDS adsorption (Fig. 5.3b) and eventually plateauing out. This trend indicates that the effective rigidity of adsorbate on the sensor decreases with time and eventually reaches an equilibrium value. In addition, for a given time, the energy dissipation was smaller for larger PNDDS. This behavior is attributed to the lower surface coverage for larger PNDDS.

Figure 5.3c shows the Voigt mass as a function of time obtained using 3rd and 5th overtones. The equilibrium surface concentration ranged from 683±73 ng/cm^2 to 411±110 ng/cm^2 during the exposure stage. For smaller nanoparticle sizes (i.e. 90-nm, 110-nm, and 149-nm), the surface concentration was smaller for larger nanoparticles. On the other hand, for larger nanoparticle sizes (i.e. 174-nm, 207-nm, and 305-nm), there was no clear trend in the surface concentration with respect to the nanoparticle size. The increasing importance of the gravitational forces in comparison to intermolecular and

surface forces for larger particles may be responsible for this behavior.

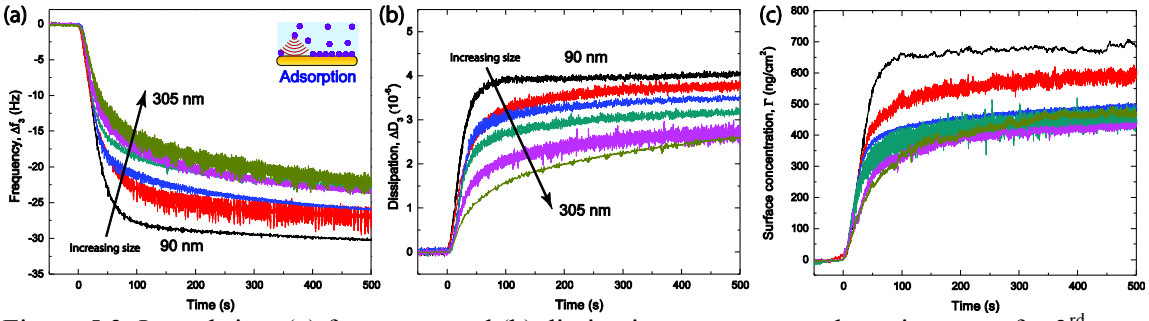

Figure 5.3. In-real-time (a) frequency and (b) dissipation response at adsorption stage for 3rd overtone (15 MHz). (c) The Voigt mass as function of time obtained through 3rd and 5th overtones. Black lines indicate PNDDS of 90 ± 5 nm, red lines PNDDS of 110 ± 4 nm, blue lines PNDDS of 149 ± 5 nm, dark cyan lines PNDDS of 174 ± 5 nm, magenta lines PNDDS of 207 ± 6 nm, and olive colored lines PNDDS of 305 ± 7 nm. For each size, the data shown above are obtained by arithmetic averaging of several experimental repeats using OriginLab software (OriginLab 8, Northampton, MA, USA).

5.3.3 Removal Behaviour of Polymeric Nanomedicine on Silica Surfaces

Figure 5.4 shows the QCM-D frequency and dissipation shifts with respect to time for PNDDS of varying sizes on silica surfaces at the rinsing stage. The frequency, which increased as the PNDDS was removed from the silica surface, followed roughly an exponential trend (R^2>0.84) with respect to time (Fig. 5.4a). However, the frequency did not return to the initial base line, indicating that adsorbed PNDDS were not removed completely from the sensor. In other words, the adsorption of PNDDS on silica is a partially reversible process. As opposed to the adsorption case, the frequency shifts did not show a simple trend with respect to the particle size for the removal case. This is because both initial surface concentration and removal rate constant were different for different sizes.

The dissipation response during the removal stage also followed an exponential trend for all sizes (Fig. 5.4b). However, there was no apparent trend in the magnitudes of

dissipation with respect to nanoparticle size. The ratios of dissipation to frequency shifts were comparable for the exposure and rinsing stages for all sizes: 0.1×10^{-6} for the exposure stage and $0.1–0.2 \times 10^{-6}$ for the rinsing stage. Considering all PNDDS contains the same building blocks i.e. PEG-b-PCL, Levofloxacin, and polystyrene, the comparable dissipation to frequency shift ratios are reasonable.

Under steady-state conditions, 68±26 ng/cm^2 to 131±19 ng/cm^2 of the PNDDS adsorbate was removed during rinsing stage (Table 5.1). The corresponding equilibrium (steady-state) surface concentration ranged from 580±122 ng/cm^2 to 357±163 ng/cm^2. Similar to the exposure stage, the equilibrium concentration decreased with increasing particle size for smaller nanoparticles. However, there was no significant difference in the equilibrium concentration for larger nanoparticles.

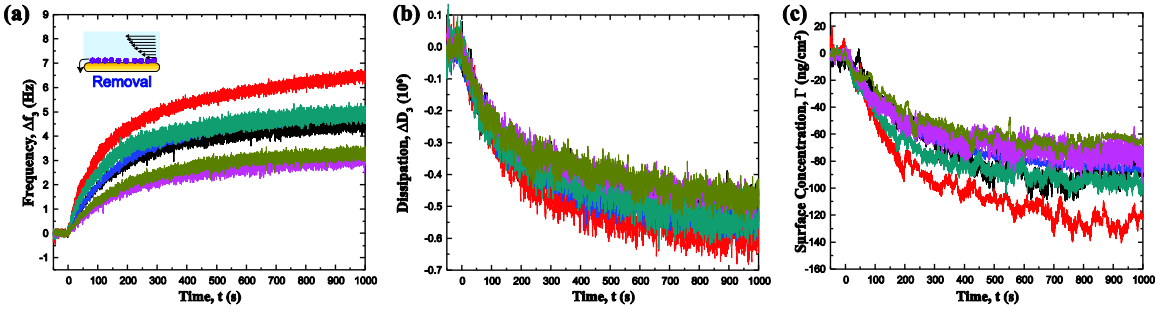

Figure 5.4. In-real-time (a) frequency and (b) dissipation response at rinsing stage at harmonics of 15 MHz. (c) The Voigt mass as function of time obtained through 3rd and 5th overtones. Black lines indicate PNDDS of 90 ± 5 nm, red lines PNDDS of 110 ± 4 nm, blue lines PNDDS of 149 ± 5 nm, dark cyan lines PNDDS of 174 ± 5 nm, magenta lines PNDDS of 207 ± 6 nm, and olive colored lines PNDDS of 305 ± 7 nm. For each size, the data shown above are obtained by arithmetic averaging of several experimental repeats using OriginLab software (OriginLab 8, Northampton, MA, USA).

5.3.4 Structural Characterization of Adsorbate

Figure 5.5 displays AFM micrographs of silica surfaces before and after exposing to 305-nm PNDDS dispersion and after rinsing the exposed surfaces with

water. The neat sensor was relatively smooth with a root-mean-square (*rms*) height of 1.1 nm (Fig. 5.5a). After the exposure stage, the presence of nanoparticles on the silica could readily be observed (Fig. 5.5b). The adsorbed nanoparticles showed a relatively broad size distribution ranging from 70 nm to 400 nm. In addition, some of the nanoparticles were found to deform up to 70% (height-to-diameter ratio) upon absorbing on the silica surfaces. The higher magnification and phase images revealed that a large fraction of the "flat looking" areas contained a polymer film of 4-5 nm thickness, suggesting that majority of PNDDS disintegrated. Upon rinsing, the majority of the intact PNDDS were removed while the polymer film mostly remained on the surface (Fig. 5.5c). The processes observed through AFM studies are illustrated in Figure 5.6.

These AFM results are consistent with the previous studies. For instance, Vangeyte *et al.* [207] investigated the adsorption behavior of (empty) polymeric micelles of PEG-b-PCL and found that both micelles and free copolymer chains exists at the silica interface after the adsorption. Likewise, the previous studies involving various type of vesicles indicated that the rupture of vesicle can take upon the adsorption under certain conditions [208, 209]. However, in our previous studies involving cellulose surfaces and ibuprofen loaded PEG-b-PCL nanomedicine, the existence of polymer film forming upon the adsorption and disintegration of polymeric nanoparticles were not observed. Both cellulose (-12 mV) [155] and silica (-25 mV to -40 mV) [210] surfaces

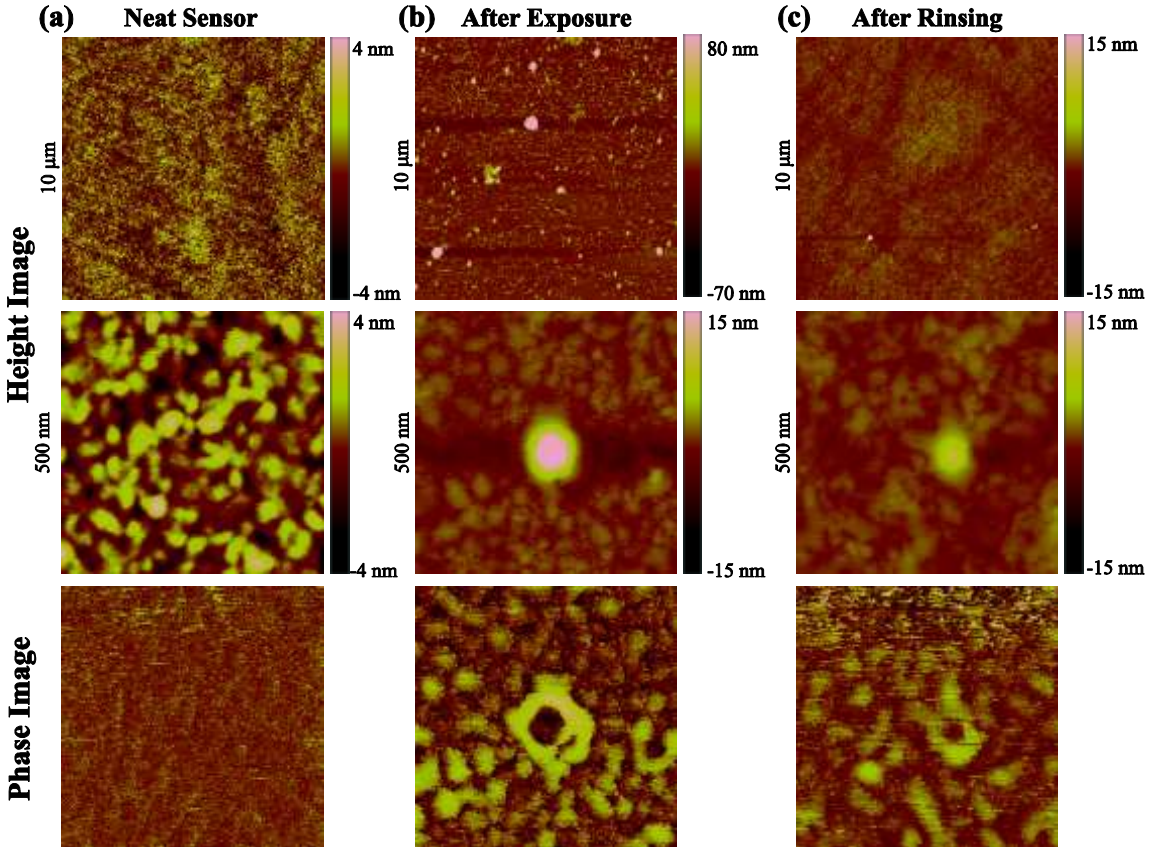

Figure 5.5. AFM micrographs of (a) the clean sensor, (b) the sensor after being exposed to the nanomedicine dispersion, and (c) the sensor after being rinsed following the exposure stage. For each stage, one low and one high resolution height map and a phase map of the magnified region are displayed.

has negative zeta potential values. In both studies, the same polymeric building block is used. Therefore, we believe that the higher solubility of levofloxacin compared to ibuprofen facilitates the disintegration (rupture) of PNDDS. The differences in the magnitudes of the zeta potentials may also play a role in the different rupture behavior. In addition, since a certain fraction of the PNDDS raptured and PNDDS showed a range of particle sizes, we may suspect that the PNDDS size can also influence the rupture behavior. However, regardless of the exact reason for the differences in the rupture

behavior, the main outcome here is that levofloxacin loaded PNDDS on silica ruptures while ibuprofen loaded PNDDS on cellulose does not rupture. This information will be used as the basis of our modeling effort to describe the adsorption of the PNDDS used in this study.

5.3.5 Model for the Adsorption and Removal Kinetics

Since a partial removal of PDNNS upon rinsing is observed in this study, a partially irreversible model is proposed to describe the kinetics of the adsorption and removal of PDNNS onto and from silica surface. In this model, there are two states of nanoparticle on the surface: α-state involving intact and deformed nanomedicine and β-state involving disintegrated copolymer chains forming a film on the surface (Fig. 5.6). PDNNS in the α-state can be removed while PDNNS in the β-state cannot be removed within the timescales of the QCM-D studies. In other words, PDNNS in the β-state is responsible for the partially reversible behavior.

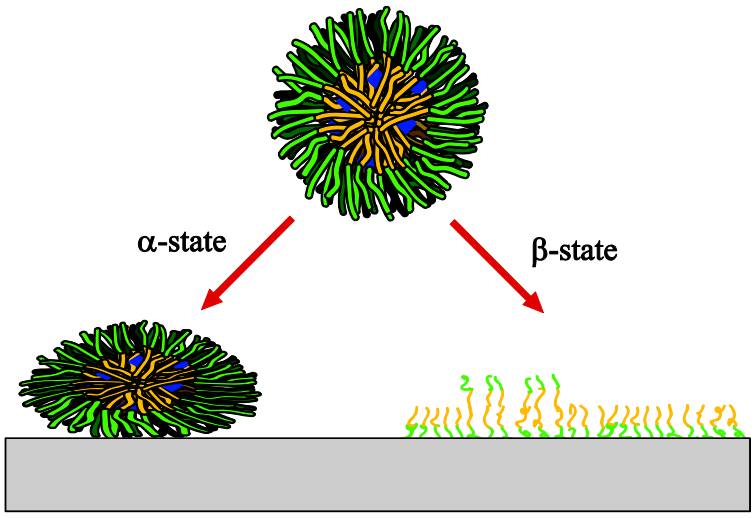

Figure 5.6. An illustration of the two states of the PDNNS on the silica surface. The PDNNS can either deform on the silica surface (α-state) or disintegrate into its building blocks (β-state) upon adsorption on the silica surface.

Assuming the multilayer nanomedicine adsorption does not take place, the total surface concentration during adsorption stage and the concentration of α-particles during rinsing can be expressed as [155]:

$$\Gamma = \frac{k_a m_s \Gamma^*}{k_a m_s + \Gamma^* k_r <\theta>} + C_1 e^{-(k_a m_s/\Gamma^* + k_r <\theta>)t} \quad [5.1]$$

$$\Gamma_\alpha = C_2 e^{-k_r t} \quad [5.2]$$

where Γ is the total surface concentration of all PDNNS on the sensor surface; Γ^* is the maximum surface concentration of PDNNS that can cover the surface, which is the equilibrium concentration of PDNNS on the sensor surface at very large concentrations; Γ_α is the surface concentration of α-particles; m_s is the bulk solution concentration of PDNNS; k_a is the rate of adsorption; and k_r is the rate of removal. $<\theta>$ is the average ratio of non-deformed to total PDNNS mass on the surface of the sensor ($\theta=\Gamma_\alpha/\Gamma$).

By fitting Eq. 5.1 and 5.2 with the QCM-D data, k_a and k_r was determined (Fig. 5.7). The adsorption rate constants decreased with increasing size. On the other hand, the removal rate constants increased with increasing size. Previous studies have shown that while hydrodynamic forces are responsible for the removal process of nanoparticles and particle-surface interactions and/or diffusion are responsible for the adsorption process nanoparticles in QCM-D studies [155, 211, 212]. Therefore, the removal and adsorption rate constants can display opposite trends with respect to the nanoparticle size as in this study.

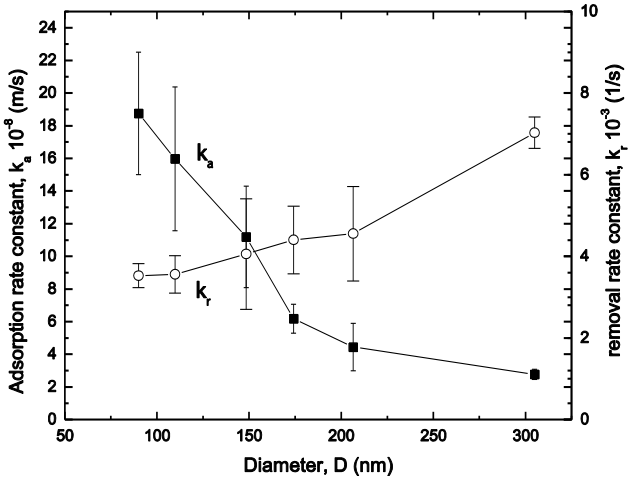

Figure 5.7. Adsorption and removal constants of polymeric nanomedicine on and from silica surfaces as a function of polymeric nanomedicine size.

5.3.6 Hydrodynamics of Nanoparticle Dispersion in the QCM-D Chamber

To explain the relationship between k_a and size and between k_r and size for this system, mass and fluid transport models are needed. To this end, first, we focused on the hydrodynamics in the QCM-D chamber. Since the diameter of inlet and outlet are much smaller than the diameter of the chamber (Fig. 5.8a), bipolar coordinate can be used here. The relation between bipolar coordinate and Cartesian coordinate is [213]:

$$x = a\frac{sinh\tau}{cosh\tau - cos\sigma} \quad [5.3]$$

$$y = a\frac{sin\sigma}{cosh\tau - cos\sigma} \quad [5.4]$$

where the ζ-coordinate of a point equals the angle F_1PF_2 and the η-coordinate equals the natural logarithm of the ratio of the distances r_1 and r_2 to the foci (Fig. 5.8b)

$$\tau = ln\frac{r_1}{r_2} \quad [5.5].$$

The curves of constant ζ correspond to non-concentric circles (solid lines in Fig. 4.8c) and the curves of constant η correspond to non-intersecting circles (dashed lines in

Fig. 4.8c).

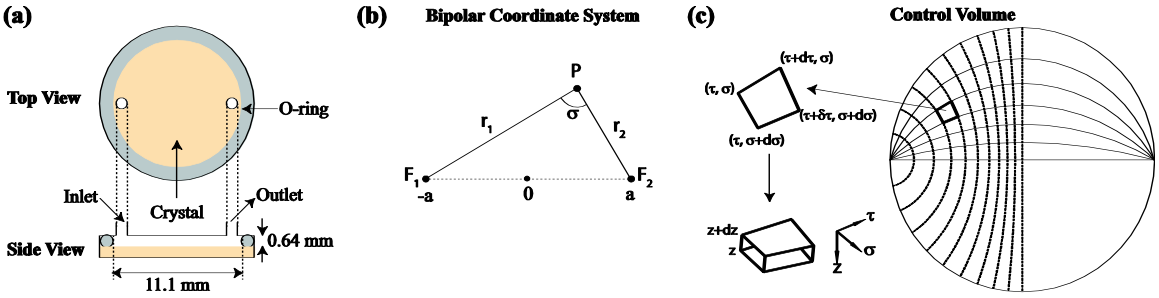

Figure 5.8 (a) A schematic of QCM-D chamber. The inner diameter is 11.1 mm and the depth is about 0.64 mm. The crystal sensor is mounted on bottom side of the chamber, and an inlet and an outlet are on the top side. The O-ring is used to prevent leaking of fluid to outside of chamber. (b) Bipolar coordinate system. (c) Control volume selected for the derivation of transport equations.

The two foci F_1 and F_2 in bipolar coordinates indicate inlet and outlet, respectively. While the curves of constant η correspond to isopotential lines, the curves of constant ζ, which are orthogonal to isopotential lines, correspond to the potential gradient. Since both the mass sensitivity and amplitude distribution curves follow a Gaussian function in QCM-D and significant fraction of the QCM-D signal is obtained mostly within a radius of 3 mm [214] and the depth of the chamber is much smaller than the diameter of the chamber, the influence of the side walls is neglected in this analysis.

The flow is in the τ- direction, hence there is no velocity component in either the σ- or z- direction (i.e., $v_\zeta = v_z = 0$). Then, the continuity equation for an incompressible fluid at steady state is:

$$(v_\tau h_\sigma d\sigma dz)|_\tau - (v_\tau h_\sigma d\sigma dz)|_{\tau+d\tau} = 0 \qquad [5.6]$$

Therefore, $v_\eta h_\zeta d\zeta$ is independent of η. With no slip boundary conditions at the top and bottom surfaces, the solution for the velocity profile at different z can be found to be:

$$v_\tau = 6\frac{z}{b}\left(1-\frac{z}{b}\right) < v_\tau > \quad [5.7]$$

where b is depth of the gap, $<v_\eta>$ is average of v_η from z=0 to z=b with constant η and ζ and the origin is the entrance to the QCM-D chamber. At the inlet ($\eta = -\infty$), assuming that the fluid has the same flow rates in all directions, the total volumetric flow per linear depth, Q/b, can be obtained integrating the velocity to give:

$$2\int_{\pi/2}^{\pi} < v_\tau > h_\sigma d\sigma = \frac{Q}{b} \quad [5.8].$$

Here, h_ζ is the scale factors for ζ coordinate in bipolar coordinates, and the length along ζ axis is $h_\zeta d\zeta$. The scale factors for the bipolar coordinates (ζ, η) are equal to [213]:

$$h_\sigma = h_\tau = \frac{a}{cosh\tau - cos\sigma} \quad [5.9]$$

Using Eq. 5.7, 5.8 and 5.9, velocity at any point could be expressed as:

$$v_\tau(\tau,\sigma,z) = 6\frac{z}{b}\left(1-\frac{z}{b}\right)\frac{cosh\tau - cos\sigma}{a}\frac{Q}{\pi b} \quad [5.10]$$

In addition to the approximate analytical solution (*i.e.* Eq. 5.10), three-dimensional solution for the velocity profile was numerically obtained using COMSOL Multiphysics to check the validity of assumptions used for the analytical solution case. Figure 5.9a shows the velocity field of water in the QCM-D chamber obtained by COMSOL. The direction of flow was found to be along η-axis as assumed in the case of analytical model. The velocity decreased with increasing η from η = -∞ to η = 0 (the left half of the chamber), and then increased with increasing η from η = 0 to η = ∞ (the right half of the chamber). At a given constant τ, the velocity was maximum at ζ = π (along the straight line connecting the inlet and outlet). Overall, the numerical and analytical solutions were very similar, especially in the region where the majority of QCM-D

signal is obtained i.e. the central area within the radius of 3 mm (Fig. 5.9a&b).

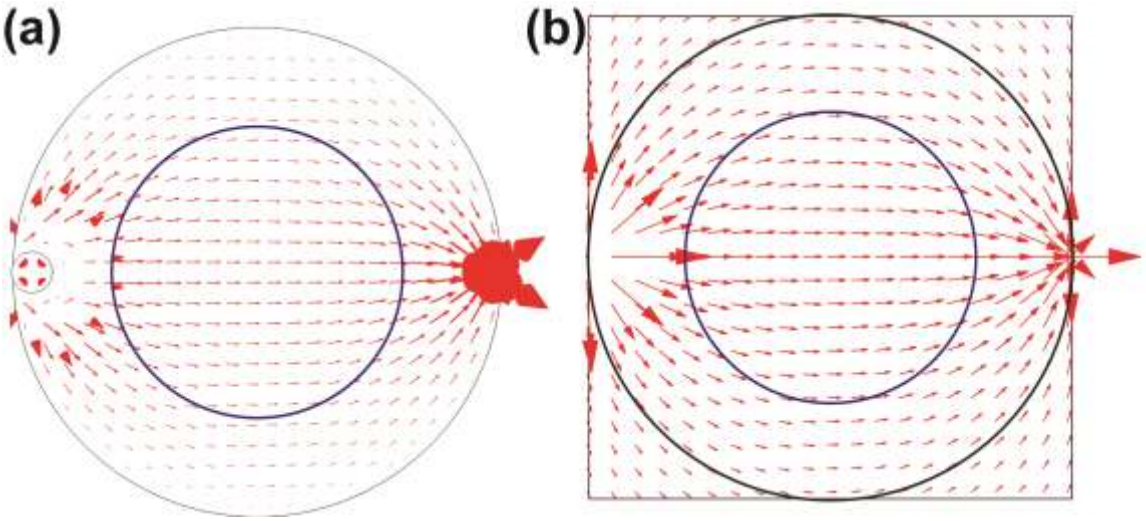

Figure 5.9. (a) Velocity field in the QCM-D chamber obtained using Comsol Multiphysics (top view). (b) A vectorial plot of Eq. 10 plotted using Matlab R2012a (Mathworks, Natick, Massachusetts, U.S.A). The black lines indicate the boundary of the QCM-D chamber while the blue lines indicate the region from which the majority of QCM-D signal is obtained.

5.3.7 Mass Transport of Nanoparticle Dispersion in the QCM-D Chamber

Given that the flow is along τ-direction and assuming that the diffusion in η- and ζ- direction is negligible in comparison the diffusion in z-direction, the convection–diffusion equation can be expressed as follows:

$$\frac{\partial c}{\partial t} dV = \left[-D_c \left[\left(\frac{\partial c}{\partial z}\right)|_z - \left(\frac{\partial c}{\partial z}\right)|_{z+dz}\right] h_\sigma d\sigma h_\tau d\tau\right] + \left[(c v_\tau h_\sigma d\sigma dz)|_\tau - (c v_\tau h_\sigma d\sigma dz)|_{\tau+d\tau}\right] \quad [5.11]$$

where the terms in the first bracket on the right side is diffusion at *z*-direction, the terms in the second bracket on the right side is convection at η-direction. Here, D_c is diffusivity, c is the concentration of nanoparticles, and $dV=(h_\eta d\eta)(h_\zeta d\zeta)dz$ is the differential control volume shown in Figure 5.8c. Dividing both sides to dV leads to:

$$\frac{\partial c}{\partial t} = D_c \frac{\partial^2 c}{\partial z^2} - \frac{\partial (c v_\tau h_\sigma d\sigma)}{\partial S} \quad [5.12]$$

where ∂S is the differential sweep area: $\partial S = h_\sigma d\sigma h_\tau d\tau$ and S is the sweep area from η = -∞ (inlet) to $\eta = \eta$ with the width of $h_\zeta d\zeta$ i.e. $S(\tau, \sigma) = \int_{\tau=-\infty}^{\tau=\tau} h_\sigma d\sigma h_\tau d\tau$.

Plugging Eq. 5.10 into Eq. 5.12 gives rise to:

$$\frac{\partial c}{\partial t} = D_c \frac{\partial^2 c}{\partial z^2} - 6\frac{z}{b}\left(1 - \frac{z}{b}\right) K d\sigma \frac{\partial c}{\partial S} \quad [5.13]$$

where $K = Q/\pi b$. The boundary conditions are as follows:

at $t = 0$, c = 0 for all $S > 0$ [5.14]

at $S = 0$, c = c_0 for all $t > 0$ [5.15]

at $z = 0$, $D_c \partial c \, \partial z = R(c)$ for all $t \geq 0$, $S > 0$ [5.16]

where $R(c)$ is the unknown intrinsic kinetic rate expression for particle adsorption, c_0 the concentration of nanoparticles in inlet solution.

At times long relative to the time required for the initial nanoparticle front to displace the pure water, a steady-state concentration boundary layer is established in the nanoparticle dispersion adjacent to the adsorbing surface. Within the region of the concentration boundary layer, where $z/b << 1$, then the model describing transport-limited adsorption at long times can be given by:

$$D_c \frac{\partial^2 c}{\partial z^2} = 6\frac{z}{b} K d\sigma \frac{\partial c}{\partial S} \quad [5.17]$$

subject to:

at $z = 0$, $c = 0$ for all $S > 0$ [5.18]

at $z = \infty$, $c = c_0$ for all $S \geq 0$ [5.19]

at $S = 0$, $c = c_0$ for all $z > 0$ [5.20]

The equation can be solved analytically using a similarity variable, $u = z\times[6Kd\zeta/(9bDS)]^{1/3}$. The corresponding solution is:

$$\frac{d\Gamma}{dt} = -D_c \frac{\partial c}{\partial z}|_{z=0} = \frac{D_c c_0}{Gamma\left(\frac{4}{3}\right)}\left(\frac{6K}{9bD_cS}\right)^{1/3} \quad [5.21]$$

where $Gamma(4/3)$ is the Gamma function and

$$\frac{K}{S} = \frac{\frac{Q}{\pi b}d\sigma}{\int_{\tau=-\infty}^{\tau} h_\sigma d\sigma h_\tau d\tau} = \frac{\frac{Q}{\pi b}}{\int_{\tau=-\infty}^{\tau} h_\sigma h_\tau d\tau} \quad [5.22]$$

The Equation 5.22 is very similar to Leveque Solution [215], which is

$$\frac{d\Gamma}{\partial t} = \frac{D_c c_0}{Gamma\left(\frac{4}{3}\right)}\left(\frac{\gamma}{9D_c x}\right)^{1/3} \quad [5.23].$$

For one dimensional potential flow in the Cartesian coordinates, $h_\eta = h_\zeta = 1$, and $S = xdy$, Eq. 5.21 simplifies to the Leveque Solution.

Leveque solution has successfully explained various studies involving protein adsorption [212, 216], polymer adsorption [217, 218], copolymer adsorption [211], and polymer-modified protein adsorption [219] in narrow slits under laminar flow conditions. Therefore, Leveque solution may also be used for the polymeric nanomedicine adsorption and so is Equation 5.21, which is a modified Leveque solution taking into account the curvilinear nature of the flow inside the QCM-D chamber. The effective adsorption rate constant k_a can be expressed as:

$$k_a = \frac{D_c}{Gamma\left(\frac{4}{3}\right)}\left(\frac{6K}{9bD_cS}\right)^{1/3} \quad [5.24].$$

Here, diffusivity, D_c, is assumed to a function of size as described by the Stokes-Einstein Equation[215]:

$$D_c = \frac{k_B T}{6\pi R\eta} \quad [5.25].$$

Equation 5.24 is based on the assumption that diffusion in the η- and ζ- directions can be ignored compared to the diffusion in z-direction and convection in the η-direction. We compared the magnitudes of these four mass transfer terms using the numerically solved concentration profiles at several selected points, and found that the diffusion in the z-direction is about 10^3~10^5 times greater than that in the η- and ζ- direction (In Appendix C2). Therefore, the assumption that diffusion in η- and ζ- directions can be ignored is reasonable.

Equation 5.24 can rewrite as

$$k_a = \frac{{D_c}^{2/3} Q^{1/3}}{Gamma\left(\frac{4}{3}\right)} \left(\frac{6}{9b} \frac{\frac{1}{\pi b}}{\int_{\tau=-\infty}^{\tau} h_\sigma h_\tau d\tau} \right)^{1/3} \quad [5.26].$$

If let

$$n = \frac{1}{Gamma\left(\frac{4}{3}\right)} \left(\frac{6}{9b} \frac{\frac{1}{\pi b}}{\int_{\tau=-\infty}^{\tau} h_\sigma h_\tau d\tau} \right)^{1/3} \quad [5.27].$$

n is determined by position of the measured point and geometry of bipolar fluid field. Then k_a can be expressed as:

$$k_a = {D_c}^{2/3} Q^{1/3} n \quad [5.28].$$

5.3.8 Comparison of Theoretical Calculation and Experimental Results

Equation 5.28 calculates adsorption rate at any point (η, ζ). However, as mentioned earlier, QCM-D mostly measures the average mass adsorption on the area with r < 3 mm. To compare experimentally measured adsorption rates with the one obtained from the modified Leveque solution, averaged k_a need be calculated as:

$$< k_a >= {D_c}^{2/3} Q^{1/3} < n > \quad [5.29].$$

We numerically average n over the area within radius of 3 mm and normalize the integration with the area of circle with a radius of 3 mm and <n> was calculated to be 4.44×10^{3} $m^{-4/3}$ (see Appendix C1 for further details).

Figure 5.10 shows experiment and theoretically calculated (based on Eq. 5.29) adsorption rate constants. The theoretical k_a matched experimental k_a both in the trend and magnitude, in particular for particles smaller than 150 nm. The small difference between the theoretical and experimental k_a values for larger particles (D>150 nm) could be due to several factors. First, the influence of gravitational forces becomes important as the particles get larger [195, 220]. Therefore, we carried out additional experiments where the QCM-D experiments were conducted after changing the orientation of the chamber upside-down. We found that there was no significant difference in the adsorption behavior, thereby concluding that the gravitational forces are not responsible for the abovementioned differences for larger particles. Second, the particles have a size distribution (Fig. 5.2) as opposed to a single uniform size used in theoretical model. As discussed earlier, the fact that the size distribution is wider for larger nanoparticles can also be responsible for the lack of any consistent trend for larger nanoparticles. Third, the penetration depths of 3rd and 5th overtones in the QCM-D is about 100-150 nm [221, 222]. In other words, decaying oscillatory waves partially sense the mass of the particles above this range and underestimate the experimentally measured rate constants.

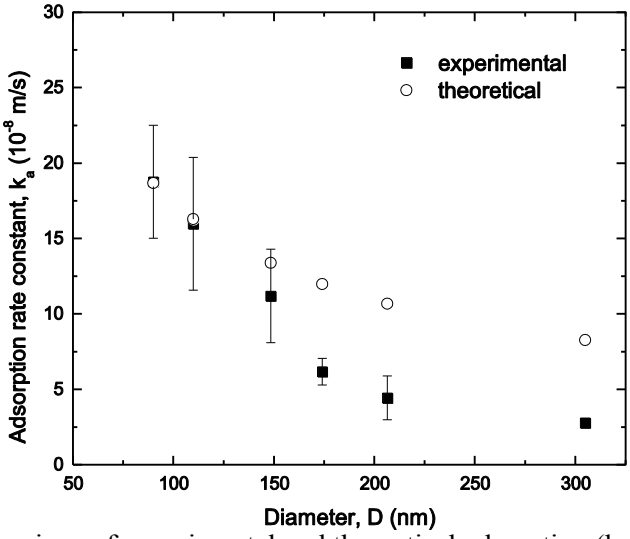

Figure 5.10. The comparison of experimental and theoretical adsorption (based on Eq. 24) rate constants as a function of particle size.

Regarding the removal rate constant, k_r, it was shown in Figure 5.7 that k_r increases with increasing particle size. If the particle removal is governed by diffusion or desorption, the removal rate constant would be decrease with particle size since diffusion coefficient decreases with particle size and desorption energy barrier increases with particle size [85, 215]. Hence, the nanomedicines were not removed through diffusion or desorption; and were mostly likely to be removed by the hydrodynamic forces acting parallel to the surfaces [155, 223-225]. Hydrodynamic forces are proportional to fluid viscosity, particle size, and fluid velocity at the middle of particle. Considering the fluid velocity at middle of particle increase with increasing particle size for no-slip boundary or partial slip boundary condition, it is reasonable that the removal rate constants increase as the particle size increases.

5.4 Conclusions

In this Chapter, we study the adsorption and removal behavior of a model

PNDDS with different sizes on silica surface. The adsorption of such particles on silica surface was found to be partially reversible. The adsorption rate constant decreased with increasing particle size. This trend is primarily due to the smaller diffusion coefficient for larger nanomedicine. We also developed a modified Leveque equation to describe the mass transport behavior inside the QCM-D chamber. The adsorption rate constants calculated using this equation was found to match the experimental results well. A small fraction of adsorbed PNDDS from silica surfaces could be removed by hydrodynamic forces acting parallel to the surfaces. The removal rate increased with increasing particle size. This trend is ascribed to the larger flow velocity at the distance of particle radius from the surface for larger particle sizes.

CHAPTER VI

SUMMARY

In this dissertation, transports of polymeric nanomedicine in the environment surface as well as uptake of nanomedicine into plants were investigated through six chapters. Cellulose surface and silica surface were chosen as environmental surfaces and ryegrass was chosen as a plant. Adsorption and removal of PNDDS on and from environmental surface was studied by QCM and AFM. Uptake and translocation of PNDDS in ryegrass were investigated by SFM, confocal microscopy, AFM, and cross sectional TEM. Adsorption, removal and uptake kinetics were also studied theoretically.

In Chapter I, a brief review is presented on the importance of PNDDS in drug delivery and their potential environment impact. While PNDDS have many advantages for therapeutic use due to their special properties, there properties may also make them a potential environment problem after PNDDS enter environment by several possible routes, since most PNDDS are loaded with therapeutic materials that are ecotoxic. Current studies on transport phenomena of nanoparticles, transport of nanoparticles in the environment, interaction between nanoparticles and environmental interface are also present in Chapter I

In Chapter II, current studies on adsorption of polymer nanoparticle are present. Adsorption behavior of polymeric nanoparticles includes adsorption of functional molecules on polymeric nanoparticles, and adsorption of polymeric nanoparticles on large surfaces. The adsorption of polymeric nanoparticles may also take place via two

kinetics regimes at different times: a diffusion-limited process in the initial stage, and a significantly slower process at dense surface coverage. Multi-layer adsorption is usually not applicable due to the repulsive interaction between polymeric nanoparticles. Therefore, the pattern of polymeric adsorption equilibrium isotherms assumes either a Langmuir-type or Freundlich-type shape. Adsorption Kinetics was also studied generally in this chapter.

In Chapter III, adsorption, desorption, and removal of behavior of a model PNDDS of various sizes on and from cellulose was investigated by QCM and AFM. It is determined that most of the adsorbate PNDDS do not desorb from the cellulose surface even upon rinsing with a large amount of water *i.e.* the adsorption process is only partially reversible. PNDDS may deform and adsorb irreversibly on cellulose surface.

The rate constant of adsorption decreases with increasing PNDDS size. This trend is ultimately related to the activation energy of absorption, which is, at first approximation, linearly proportional to the PNDDS size. The theoretical k_a calculations relying on attractive van der Waals interaction, Born repulsion, and electrical double-layer repulsion give a fairly accurate estimates for the measured k_a values.

In addition, it is shown that hydrodynamic forces acting parallel to the surfaces (orthogonal to the intermolecular forces) are of great importance in the context of PNDDS dynamics near the cellulose wall, and ultimately responsible for the removal of PNDDS via rolling or sliding. As the particle size increases, the removal rates of the particles increased for a given hydrodynamical condition.

Chapter IV shows that ryegrass can uptake PNDDS of size ranging from 46 nm to 271 nm through its roots. The uptake behavior was studied by SFM, confocal microscopy, SEM and cross sectional TEM. The rate and fraction of PNDDS uptake by ryegrass roots increased with decreasing size. PNDDS can firstly adsorb irreversibly on root surface and then uptake into root. PNDDS was found both in root cells and intercellular space in root. It is also shown that very small amount of PNDDS, if any, transport from stem to leaf, which is presumably due to the selectivity of membranous ligule.

Furthermore, the kinetics of uptake was studied as a two-step process: adsorption onto root and uptake into root. It was found that the adsorption step was faster than the uptake step, making the uptake step overall rate determining step for the transport of PNDDS from aqueous media into ryegrass root. The trend of decreasing uptake rate with increasing PNDDS size can be explained through the consideration of mass flux of particles or molecules across a porous membrane when particle size is comparable to the pre size.

Chapter V studies the adsorption and removal behavior of another model PNDDS agent with different sizes on silica surface by QCM and AFM. The adsorption of such particles on silica surface was also found to be partially reversible. Some of the adsorbed PNDDS were deformed up to 70%. The majority of the PNDDS had disintegrated and formed a polymer film of 4-5 nm. The majority of the intact nanomedicine was removed while most of the polymer film remained on the surface upon rinsing.

The adsorption rate constant decreased with increasing particle size. This trend is

primarily due to the smaller diffusion coefficient for larger nanomedicine. A modified Leveque equation was developed to describe the mass transport behavior inside the QCM-D chamber. The adsorption rate constants calculated using this equation was found to match the experimental results well. A small fraction of adsorbed PNDDS from silica surfaces could be removed by hydrodynamic forces acting parallel to the surfaces. The removal rate increased with increasing particle size. This trend is ascribed to the larger flow velocity at the distance of particle radius from the surface for larger particle sizes.

With the results obtained in the dissertation, PNDDS can easier adsorb onto environment surface and uptake into some plants. Transport behavior and kinetics of PNDDS onto environmental surface was primary studied. The results are significant because more and more PNDDS are entering pre-clinical, clinical, or commercial development. PNDDS could be an environment concern since most of PNDDS are loaded with ecotoxic therapeutics and properties of PNDDS largely increase their environment impact.

Future studies are recommended in order to gain a complete knowledge of environmental impact of PNDDS so that a systemic management method of PNDDS waste could develop to better govern their disposal. Future studies could focus on transport of PNDDS with different concentrations, stabilities, surface property. Also, Uptake of PNDDS into different plants and their storage time in plants is also required to study. Whether PNDDS could accumulate through food chain and whether they could finally go back to human body is also important to fulfill the research on environmental

impact of PNDDS.

REFERENCES

1. Etheridge, M.L., et al., *The big picture on nanomedicine: the state of investigational and approved nanomedicine products.* Nanomedicine-Nanotechnology Biology and Medicine, 2013. **9**(1): p. 1-14.
2. Mahapatra, I., et al., *Potential environmental implications of nano-enabled medical applications: critical review.* Environmental Science: Processes & Impacts, 2013. **15**(1): p. 123-144.
3. Borm, P.J.A. and D. Muller-Schulte, *Nanoparticles in drug delivery and environmental exposure: same size, same risks?* Nanomedicine, 2006. **1**(2): p. 235-249.
4. Chan, V.S.W., *Nanomedicine: an unresolved regulatory issue.* Regulatory Toxicology and Pharmacology, 2006. **46**(3): p. 218-224.
5. Wiesner, M.R. and J.-Y. Bottero. *Environmental nanotechnology: applications and impacts of nanomaterials*. McGraw-Hill Professional. New York. 2007.
6. Oberdörster, G., E. Oberdörster, and J. Oberdörster, *Nanotoxicology: an emerging discipline evolving from studies of ultrafine particles.* Environ Health Perspect, 2005. **113**: 823–839.
7. Akbulut, M., et al., *Novel methods of targeted drug delivery: the potential of multifunctional nanoparticles.* Expert Review of Clinical Pharmacology, 2009. **2**(3): p. 265-282.

8. Mundargi, R.C., et al., *Nano/micro technologies for delivering macromolecular therapeutics using poly(D,L-lactide-co-glycolide) and its derivatives.* Journal of Controlled Release, 2008. **125**(3): p. 193-209.

9. Sahoo, S.K. and V. Labhasetwar, *Nanotech approaches to delivery and imaging drug.* Drug Discovery Today, 2003. **8**(24): p. 1112-1120.

10. Soppimath, K.S., et al., *Biodegradable polymeric nanoparticles as drug delivery devices.* Journal of Controlled Release, 2001. **70**(1-2): p. 1-20.

11. Allen, T.M. and P.R. Cullis, *Drug delivery systems: entering the mainstream.* Science, 2004. **303**(5665): p. 1818-1822.

12. Otsuka, H., Y. Nagasaki, and K. Kataoka, *PEGylated nanoparticles for biological and pharmaceutical applications.* Advanced Drug Delivery Reviews, 2003. **55**(3): p. 403-419.

13. Burt, H.M., et al., *Development of copolymers of poly(,-lactide) and methoxypolyethylene glycol as micellar carriers of paclitaxel.* Colloids and Surfaces B: Biointerfaces, 1999. **16**(1-4): p. 161-171.

14. Dong, Y. and S.-S. Feng, *Methoxy poly(ethylene glycol)-poly(lactide) (MPEG-PLA) nanoparticles for controlled delivery of anticancer drugs.* Biomaterials, 2004. **25**(14): p. 2843-2849.

15. Batrakova, E., et al., *Pluronic P85 increases permeability of a broad spectrum of drugs in polarized BBMEC and caco-2 cell monolayers.* Pharmaceutical Research, 1999. **16**(9): p. 1366-1372.

16. Farokhzad, O.C., et al., *Targeted nanoparticle-aptamer bioconjugates for cancer chemotherapy in vivo.* Proceedings of the National Academy of Sciences, 2006. **103**(16): p. 6315-6320.

17. Cheng, J., et al., *Formulation of functionalized PLGA-PEG nanoparticles for in vivo targeted drug delivery.* Biomaterials, 2007. **28**(5): p. 869-876.

18. Alakhov, V.Y., et al., *Hypersensitization of multidrug resistant human ovarian carcinoma cells by pluronic P85 block copolymer.* Bioconjugate Chemistry, 1996. **7**(2): p. 209-216.

19. Nishiyama, N., et al., *Novel cisplatin-incorporated polymeric micelles can eradicate solid tumors in mice.* Cancer Research, 2003. **63**(24): p. 8977-8983.

20. Bogdanov, A.A., et al., *An adduct of cis-diamminedichloroplatinum(II) and poly(ethylene glycol)poly(l-lysine)−succinate: synthesis and cytotoxic properties.* Bioconjugate Chemistry, 1996. **7**(1): p. 144-149.

21. Bhadra, D., et al., *A PEGylated dendritic nanoparticulate carrier of fluorouracil.* International Journal of Pharmaceutics, 2003. **257**(1-2): p. 111-124.

22. McCarron, P.A., A.D. Woolfson, and S.M. Keating, *Sustained release of 5-fluorouracil from polymeric nanoparticles.* Journal of Pharmacy and Pharmacology, 2000. **52**(12): p. 1451-1459.

23. Simeonova, M., et al., *Poly(butylcyanoacrylate) nanoparticles for topical delivery of 5-fluorouracil.* International Journal of Pharmaceutics, 2003. **263**(1-2): p. 133-140.

24. Simon, J.A., *Estradiol in micellar nanoparticles: the efficacy and safety of a novel transdermal drug-delivery technology in the management of moderate to severe vasomotor symptoms.* Menopause, 2006. **13**(2): p. 222-231.

25. Lim Soo, P., et al., *Polycaprolactone-block-poly(ethylene oxide) micelles: a nanodelivery system for 17β-Estradiol.* Molecular Pharmaceutics, 2005. **2**(6): p. 519-527.

26. Cleuvers, M., *Aquatic ecotoxicity of pharmaceuticals including the assessment of combination effects.* Toxicology Letters, 2003. **142**(3): p. 185-194.

27. Dietrich, D.R., B.C. Hitzfeld, and E. O'Brien. *Toxicology and risk assessment of pharmaceuticals*. University of Konstanz. Konstanz, Germany. 2006.

28. Zounková, R., et al., *Ecotoxicity and genotoxicity assessment of cytostatic pharmaceuticals.* Environmental Toxicology and Chemistry, 2007. **26**(10): p. 2208-2214.

29. Jeong, J., et al.. *In vitro and in vivo toxicity study of nanoparticles*. John Wiley & Sons. New York. 2009.

30. Chen, H.L. and R.S. Juang, *Extraction of surfactin from fermentation broth with n-hexane in microporous PVDF hollow fibers: Significance of membrane adsorption.* Journal of Membrane Science, 2008. **325**(2): p. 599-604.

31. Minchin, R., *Nanomedicine: sizing up targets with nanoparticles.* Nat Nano, 2008. **3**(1): p. 12-13.

32. de Wolf, H.K., et al., *Effect of cationic carriers on the pharmacokinetics and tumor localization of nucleic acids after intravenous administration.* International Journal of Pharmaceutics, 2007. **331**(2): p. 167-175.

33. Lacerda, L., et al., *Dynamic imaging of functionalized multi-walled carbon nanotube systemic circulation and urinary excretion.* Advanced Materials, 2008. **20**(2): p. 225-230.

34. He, X.X., et al., *In vivo study of biodistribution and urinary excretion of surface-Modified Silica Nanoparticles.* Analytical Chemistry, 2008. **80**(24): p. 9597-9603.

35. Brar, S.K., et al., *Engineered nanoparticles in wastewater and wastewater sludge - Evidence and impacts.* Waste Management, 2010. **30**(3): p. 504-520.

36. Smith, S.R.. *Agricultural recycling of sewage sludge and the environment*. Cab International. Wallingford, England. 1995.

37. Nowack, B., et al., *Exposure modeling of engineered nanoparticles in the environment.* Abstracts of Papers of the American Chemical Society, 2009. **237**.

38. Cussler, E.L.. *Diffusion: mass transfer in fluid systems*. Cambridge University Press. Cambridge, England. 2009.

39. Somasundaran, P.. *Encyclopedia of surface and colloid science*. CRC Press. Boca Raton. 2006.

40. Hubbe, M.A., *Theory of detachment of colloidal particles from flat surfaces exposed to flow.* Colloids and Surfaces, 1984. **12**: p. 151-178.

41. Barouch, E., T.H. Wright, and E. Matijević, *Kinetics of particle detachment: I. General considerations.* Journal of Colloid and Interface Science, 1987. **118**(2): p. 473-481.

42. Oron, A., C. Gutfinger, and S. Hassid, *Turbulent deposition of charged particles under the influence of an external electric field.* Journal of Colloid and Interface Science, 1988. **121**(2): p. 531-542.

43. Soltani, M. and G. Ahmadi, *Detachment of rough particles with electrostatic attraction from surfaces in turbulent flows.* Journal of Adhesion Science and Technology, 1999. **13**(3): p. 325-355.

44. Schwarzenbach, R.P. and J. Westall, *Transport of nonpolar organic compounds from surface water to groundwater: laboratory sorption studies.* Environmental Science & Technology, 1981. **15**(11): p. 1360-1367.

45. Luthy, R.G., et al., *Sequestration of hydrophobic organic contaminants by geosorbents.* Environmental Science & Technology, 1997. **31**(12): p. 3341-3347.

46. Arnon, S., et al., *Transport of testosterone and estrogen from dairy-farm waste lagoons to groundwater.* Environmental Science & Technology, 2008. **42**(15): p. 5521-5526.

47. McMurdo, C.J., et al., *Aerosol enrichment of the surfactant PFO and mediation of the water−air transport of gaseous PFOA.* Environmental Science & Technology, 2008. **42**(11): p. 3969-3974.

48. Ter Laak, T.L., et al., *Facilitated transport of polychlorinated biphenyls and polybrominated diphenyl ethers by dissolved organic matter.* Environmental Science & Technology, 2009. **43**(5): p. 1379-1385.

49. Higgins, C.P. and R.G. Luthy, *Sorption of perfluorinated surfactants on sediments.* Environmental Science & Technology, 2006. **40**(23): p. 7251-7256.

50. Craun, G.F., *Waterborne disease—a status report emphasizing outbreaks in ground-water systemsa.* Ground Water, 1979. **17**(2): p. 183-191.

51. Yates, M.V., et al., *Modeling virus survival and transport in the subsurface.* Journal of Contaminant Hydrology, 1987. **1**(3): p. 329-345.

52. Snowdon, J.A., D.O. Cliver, and C.J. Hurst, *Coliphages as indicators of human enteric viruses in groundwater.* Critical Reviews in Environmental Science and Technology, 1989. **19**(3): p. 231-249.

53. Mishurov, M., A. Yakirevich, and N. Weisbrod, *Colloid transport in a heterogeneous partially saturated sand column.* Environmental Science & Technology, 2008. **42**(4): p. 1066-1071.

54. Zhuang, J., J.S. Tyner, and E. Perfect, *Colloid transport and remobilization in porous media during infiltration and drainage.* Journal of Hydrology, 2009. **377**(1): p. 112-119.

55. Grolimund, D., et al., *Transport of in situ mobilized colloidal particles in packed soil columns.* Environmental Science & Technology, 1998. **32**(22): p. 3562-3569.

56. French, R.A., et al., *Influence of ionic strength, pH, and cation valence on aggregation kinetics of titanium dioxide nanoparticles.* Environmental Science & Technology, 2009. **43**(5): p. 1354-1359.

57. Fang, J., et al., *Stability of titania nanoparticles in soil suspensions and transport in saturated homogeneous soil columns.* Environmental Pollution, 2009. **157**(4): p. 1101-1109.

58. Battin, T.J., et al., *Nanostructured TiO2: transport behavior and effects on aquatic microbial communities under environmental conditions.* Environmental Science & Technology, 2009. **43**(21): p. 8098-8104.

59. Thill, A., et al., *Cytotoxicity of CeO2 nanoparticles for Escherichia coli. Physico-chemical insight of the cytotoxicity mechanism.* Environmental Science & Technology, 2006. **40**(19): p. 6151-6156.

60. Park, B., et al., *Hazard and risk assessment of a nanoparticulate cerium oxide-based diesel fuel additive-a case study.* Inhalation Toxicology, 2008. **20**(6): p. 547-566.

61. Gimbert, L.J., et al., *Partitioning and stability of engineered ZnO nanoparticles in soil suspensions using flow field-flow fractionation.* Environmental Chemistry, 2007. **4**(1): p. 8-10.

62. Brunner, T.J., et al., *In vitro cytotoxicity of oxide nanoparticles: comparison to asbestos, silica, and the effect of particle solubility.* Environmental Science & Technology, 2006. **40**(14): p. 4374-4381.

63. Franklin, N.M., et al., *Comparative toxicity of nanoparticulate ZnO, bulk ZnO, and ZnCl2 to a freshwater microalga (Pseudokirchneriella subcapitata): the importance of particle solubility.* Environmental Science & Technology, 2007. **41**(24): p. 8484-8490.

64. Gardea-Torresdey, J., et al., *Formation and growth of Au nanoparticles inside live alfalfa plants.* Nano Letters, 2002. **2**(4): p. 397-401.

65. Kuhnen, F., et al., *Transport of iron oxide colloids in packed quartz sand media: Monolayer and multilayer deposition.* Journal of Colloid and Interface Science, 2000. **231**(1): p. 32-41.

66. Darlington, T.K., et al., *Nanoparticle characteristics affecting environmental fate and transport through soil.* Environmental Toxicology and Chemistry, 2009. **28**(6): p. 1191-1199.

67. Roh, J.-y., et al., *Ecotoxicity of silver nanoparticles on the soil nematode Caenorhabditis elegans using functional ecotoxicogenomics.* Environmental Science & Technology, 2009. **43**(10): p. 3933-3940.

68. Krueger, K.M., et al., *Characterization of nanocrystalline CdSe by size exclusion chromatography.* Analytical Chemistry, 2005. **77**(11): p. 3511-3515.

69. Utsunomiya, S., et al., *Uraninite and fullerene in atmospheric particulates.* Environmental Science & Technology, 2002. **36**(23): p. 4943-4947.

70. Kagan, V., et al., *Direct and indirect effects of single walled carbon nanotubes on RAW 264.7 macrophages: role of iron.* Toxicology Letters, 2006. **165**(1): p. 88-100.

71. Handy, R.D., et al., *Manufactured nanoparticles: their uptake and effects on fish—a mechanistic analysis.* Ecotoxicology, 2008. **17**(5): p. 396-409.

72. Cheng, J., E. Flahaut, and S.H. Cheng, *Effect of carbon nanotubes on developing zebrafish (Danio rerio) embryos.* Environmental Toxicology and Chemistry, 2007. **26**(4): p. 708-716.

73. Dunphy Guzman, K.A., M.P. Finnegan, and J.F. Banfield, *Influence of surface potential on aggregation and transport of titania nanoparticles.* Environmental Science & Technology, 2006. **40**(24): p. 7688-7693.

74. Jaisi, D.P. and M. Elimelech, *Single-walled carbon nanotubes exhibit limited transport in soil columns.* Environmental Science & Technology, 2009. **43**(24): p. 9161-9166.

75. Nel, A.E., et al., *Understanding biophysicochemical interactions at the nano–bio interface.* Nature Materials, 2009. **8**(7): p. 543-557.

76. Min, Y., et al., *The role of interparticle and external forces in nanoparticle assembly.* Nature Materials, 2008. **7**(7): p. 527-538.

77. Nel, A., et al., *Toxic potential of materials at the nanolevel.* Science, 2006. **311**(5761): p. 622-627.

78. Oberdörster, G., et al., *Principles for characterizing the potential human health effects from exposure to nanomaterials: elements of a screening strategy.* Particle and Fibre Toxicology, 2005. **2**(1): p. 8.

79. Mundargi, R.C., et al., *Nano/micro technologies for delivering macromolecular therapeutics using poly (d, l-lactide-< i> co</i>-glycolide) and its derivatives.* Journal of Controlled Release, 2008. **125**(3): p. 193-209.

80. Dunphy Guzman, K.A., M.R. Taylor, and J.F. Banfield, *Environmental risks of nanotechnology: national nanotechnology initiative funding, 2000-2004.* Environmental Science & Technology, 2006. **40**(5): p. 1401-1407.

81. Nowack, B. and T.D. Bucheli, *Occurrence, behavior and effects of nanoparticles in the environment.* Environmental Pollution, 2007. **150**(1): p. 5-22.

82. Tóth, J.. *Adsorption : theory, modeling, and analysis*. Dekker. New York. 2002.

83. Couvreur, P., et al., *Adsorption of antineoplastic drugs to polyalkylcyanoacrylate nanoparticles and their release in calf serum.* J Pharm Sci, 1979. **68**(12): p. 1521-4.

84. Chavany, C., et al., *Adsorption of oligonucleotides onto polyisohexylcyano acrylate nanoparticles protects them against nucleases and increases their cellular uptake.* Pharmaceutical Research, 1994. **11**(9): p. 1370-1378.

85. Somasundaran, P.. *Encyclopedia of surface and colloid science*. Taylor & Francis. New York. 2006.

86. Blunk, T., et al., *Kinetics of plasma protein adsorption on model particles for controlled drug delivery and drug targeting.* European Journal of Pharmaceutics and Biopharmaceutics, 1996. **42**(4): p. 262-268.

87. Lecommandoux, S., et al., *A physico-chemical investigation of poly(ethylene oxide)-block-poly(L-lysine) copolymer adsorption onto silica nanoparticles.* Journal of Colloid and Interface Science, 2011. **359**(2): p. 413-422.

88. Motschmann, H., M. Stamm, and C. Toprakcioglu, *Adsorption-kinetics of block copolymers from a good solvent - a 2-stage process.* Macromolecules, 1991. **24**(12): p. 3681-3688.

89. Hoogeveen, N.G., M.A.C. Stuart, and G.J. Fleer, *Polyelectrolyte adsorption on oxides .1. Kinetics and adsorbed amounts.* Journal of Colloid and Interface Science, 1996. **182**(1): p. 133-145.

90. Halaoui, L.I., et al., *Self-assembly of polyacrylate-capped platinum nanoparticles on a polyelectrolyte surface: kinetics of adsorption and effect of ionic strength and deposition protocol.* Langmuir, 2003. **19**(11): p. 4804-4811.

91. Rafael, T., *The London-van der Waals interaction energy between objects of various geometries.* Journal of Physics: Condensed Matter, 2001. **13**(9): p. L195.

92. Ruckenstein, E. and D.C. Prieve, *Adsorption and desorption of particles and their chromatographic-separation.* Aiche Journal, 1976. **22**(2): p. 276-283.

93. Ruckenst.E and D.C. Prieve, *Rate of deposition of brownian particles under action of london and double-layer forces.* Journal of the Chemical Society-Faraday Transactions Ii, 1973. **69**(10): p. 1522-1536.

94. Jia, X. and R.A. Williams, *Particle deposition at a charged solid liquid interface.* Chemical Engineering Communications, 1990. **91**: p. 127-198.

95. Bird, R.B., W.E. Stewart, and E.N. Lightfoot. *Transport phenomena*. John Wiley & Sons. New York. 2007.

96. Wiesner, M.R. and J.-Y. Bottero. *Environmental nanotechnology: applications and impacts of nanomaterials*. McGraw-Hill Professional. New York. 2007.

97. Oberdorster, G., E. Oberdorster, and J. Oberdorster, *Nanotoxicology: an emerging discipline evolving from studies of ultrafine particles.* Environmental Health Perspectives, 2005. **113**(7): p. 823-839.

98. Moore, M.N., *Do nanoparticles present ecotoxicological risks for the health of the aquatic environment?* Environment International, 2006. **32**(8): p. 967-976.

99. Boxall, A.B.A., *The environmental side effects of medication - how are human and veterinary medicines in soils and water bodies affecting human and environmental health?* Embo Reports, 2004. **5**(12): p. 1110-1116.

100. Steen, E. and K. Larsson, *Carbohydrates in roots and rhizomes of perennial grasses.* New Phytologist, 1986. **104**(3): p. 339-346.

101. Zhang, W.L., et al., *Amphiphilic toothbrushlike copolymers based on poly(ethylene glycol) and poly(epsilon-caprolactone) as drug carriers with enhanced properties.* Biomacromolecules, 2010. **11**(5): p. 1331-1338.

102. Tian, Y.Q., et al., *2,1,3-Benzothiadiazole (BTD)-moiety-containing red emitter conjugated amphiphilic poly(ethylene glycol)-block-poly(epsilon-caprolactone) copolymers for bioimaging.* Journal of Materials Chemistry, 2010. **20**(9): p. 1728-1736.

103. Richter, A., et al., *Solubilization of sagopilone, a poorly water-soluble anticancer drug, using polymeric micelles for parenteral delivery.* International Journal of Pharmaceutics, 2010. **389**(1-2): p. 244-253.

104. Mikhail, A.S. and C. Allen, *Poly(ethylene glycol)-b-poly(epsilon-caprolactone) micelles containing chemically conjugated and physically entrapped docetaxel: synthesis, characterization, and the influence of the drug on micelle morphology.* Biomacromolecules, 2010. **11**(5): p. 1273-1280.

105. Akbulut, M., et al., *Generic method of preparing multifunctional fluorescent nanoparticles using flash nanoprecipitation.* Advanced Functional Materials, 2009. **19**(5): p. 718-725.

106. Akbulut, M., et al., *Novel methods of targeted drug delivery: the potential of multifunctional nanoparticles.* Expert Review of Clinical Pharmacology, 2009. **2**: p. 265-282.

107. VanTassel, P.R., P. Viot, and G. Tarjus, *A kinetic model of partially reversible protein adsorption.* Journal of Chemical Physics, 1997. **106**(2): p. 761-770.

108. DeMejo, L.P., D. Rimai, and L.H. Sharpe. F*undamentals of adhesion and interfaces*. Gordon and Breach Science Publishers. New York. 1999.

109. Maugis, D. and H.M. Pollock, *Surface forces, deformation and adherence at metal microcontacts.* Acta Metallurgica, 1984. **32**(9): p. 1323-1334.

110. Rimai, D.S., L.P. Demejo, and R.C. Bowen, *Mechanics of particle adhesion.* Journal of Adhesion Science and Technology, 1994. **8**(11): p. 1333-1355.

111. Brandani, P. and P. Stroeve, *Adsorption and desorption of PEO−PPO−PEO triblock copolymers on a self-assembled hydrophobic surface.* Macromolecules, 2003. **36**(25): p. 9492-9501.

112. Chen, N., et al., *Adhesion and friction of polymer surfaces: the effect of chain ends.* Macromolecules, 2005. **38**(8): p. 3491-3503.

113. Kinning, D.J., *Surface and interfacial structure of release coatings for pressure sensitive adhesives i. polyvinyl N-alkyl carbamates.* The Journal of Adhesion, 1997. **60**(1): p. 249-274.

114. Chaudhury, M.K. and M.J. Owen, *Adhesion hysteresis and friction.* Langmuir, 1993. **9**(1): p. 29-31.

115. Benz, M., et al., *The deformation and adhesion of randomly rough and patterned surfaces.* The Journal of Physical Chemistry B, 2006. **110**(24): p. 11884-11893.

116. Anderson, G.P., S.J. Bennett, and K.L. DeVries. *Analysis and testing of adhesive bonds*. Academic Press. San Diego. 1977.

117. Maeda, N., et al., *Adhesion and friction mechanisms of polymer-on-polymer surfaces.* Science, 2002. **297**(5580): p. 379-382.

118. Ruths, M. and S. Granick, *Rate-dependent adhesion between polymer and surfactant monolayers on elastic substrates.* Langmuir, 1998. **14**(7): p. 1804-1814.

119. Schönherr, H. and G.J. Vancso. *Polymer surface and interface properties and (dynamic) processes*, in *Scanning force microscopy of polymers*, Springer. New York. 2010.

120. Bhushan, B.. *Springer handbook of nanotechnology*. Springer. New York. 2010.

121. Kastl, K., et al., *Partially reversible adsorption of annexin A1 on POPC/POPS bilayers investigated by QCM measurements, SFM, and DMC simulations.* Chembiochem, 2006. **7**(1): p. 106-115.

122. Apte, J.S., et al., *Kinetics of leucine-lysine peptide adsorption and desorption at --CH_3 and --COOH terminated alkylthiolate monolayers.* Biointerphases, 2010. **5**(4): p. 97-104.

123. Lamblet, M., et al., *Key role of receptor density in colloid/cell specific interaction: a quantitative biomimetic study on giant vesicles.* The European Physical Journal E: Soft Matter and Biological Physics, 2008. **26**(1): p. 205-216.

124. Lyklema, J.. *Fundamentals of interface and colloid science: solid-liquid interfaces*. Academic Press. Waltham, Massachusetts. 1995.

125. Baralia, G.G., et al., *Nanodecoding by dewetting.* Advanced Materials, 2007. **19**(24): p. 4453-4459.

126. Bergstrom, L., et al., *Spectroscopic ellipsometry characterisation and estimation of the Hamaker constant of cellulose.* Cellulose, 1999. **6**(1): p. 1-13.

127. Israelachvili, J.N.. *Van der Waals forces between particles and surfaces*, in *intermolecular and surface forces*, Academic Press. San Diego. 2011.

128. Toussaint, A.F. and P. Luner, *The wetting properties of grafted cellulose films.* Journal of Adhesion Science and Technology, 1993. **7**(6): p. 635-648.

129. Leighton, D. and A. Acrivos, *The lift on a small sphere touching a plane in the presence of a simple shear flow.* Zeitschrift für Angewandte Mathematik und Physik (ZAMP), 1985. **36**(1): p. 174-178.

130. Wang, H.-C., *Effects of inceptive motion on particle detachment from surfaces.* Aerosol Science and Technology, 1990. **13**(3): p. 386 - 393.

131. Toikka, G., R.A. Hayes, and J. Ralston, *The application of lateral force microscopy to particle removal in aqueous polymer solutions.* Journal of Adhesion Science and Technology, 1997. **11**(12): p. 1479-1489.

132. Visser, J., *Particle adhesion and removal: a review.* Particulate Science and Technology: An International Journal, 1995. **13**(3): p. 169 - 196.

133. Soltani, M. and G. Ahmadi, *Particle removal mechanisms under substrate acceleration.* The Journal of Adhesion, 1994. **44**(3): p. 161 - 175.

134. Persson, B.N.J.. *Sliding friction: physical principles and applications*. Springer. London. 2000.

135. Knothe, K. and U. Miedler, *Analytical approximation formulae for the rolling resistance of elastic and viscoelastic cylinders.* Konstruktion, 1995. **47**: p. 118.

136. Burdick, G.M., N.S. Berman, and S.P. Beaudoin, *Describing hydrodynamic particle removal from surfaces using the particle Reynolds number.* Journal of Nanoparticle Research, 2001. **3**(5-6): p. 455-467.

137. Maynard, A., D. Bowman, and G. Hodge, *The problem of regulating sophisticated materials.* Nature Materials, 2011. **10**(8): p. 554-557.

138. Colvin, V.L., *The potential environmental impact of engineered nanomaterials.* Nature Biotechnology, 2003. **21**(10): p. 1166-1170.

139. Klaine, S.J., et al., *Nanomaterials in the environment: behavior, fate, bioavailability, and effects.* Environmental Toxicology and Chemistry, 2008. **27**(9): p. 1825-1851.

140. Wiesner, M.R., et al., *Decreasing uncertainties in assessing environmental exposure, risk, and ecological implications of nanomaterials.* Environmental Science & Technology, 2009. **43**(17): p. 6458-6462.

141. Ma, X.M., et al., *Interactions between engineered nanoparticles (ENPs) and plants: Phytotoxicity, uptake and accumulation.* Science of the Total Environment, 2010. **408**(16): p. 3053-3061.

142. Rico, C.M., et al., *Interaction of nanoparticles with edible plants and their possible implications in the food chain.* Journal of Agricultural and Food Chemistry, 2011. **59**(8): p. 3485-3498.

143. Lin, D.H. and B.S. Xing, *ENVR 55-phytotoxicity of ZnO nanoparticle: inhibition of ryegrass growth.* Abstracts of Papers of the American Chemical Society, 2008. **235**: p. 1053.

144. Suksiriworapong, J., et al., *Investigation of polymer and nanoparticle properties with nicotinic acid and p-aminobenzoic acid grafted on poly(epsilon-caprolactone)-poly(ethylene glycol)-poly(epsilon-caprolactone) via click chemistry.* Bioconjugate Chemistry, 2011. **22**(4): p. 582-594.

145. Oh, W.K., H. Yoon, and J. Jang, *Size control of magnetic carbon nanoparticles for drug delivery.* Biomaterials, 2010. **31**(6): p. 1342-1348.

146. Ellis, E.A., *Solution to the prblem of substitution of ERL 4221 for vinyl cyclohexene dioxide in Spurr low viscosity embedding formulations.* Microscopy Today, 2006. **14**: p. 32-33.

147. Sackett, D.L. and J. Wolff, *Nile red as a polarity-sensitive fluorescent-probe of hydrophobic protein surfaces.* Analytical Biochemistry, 1987. **167**(2): p. 228-234.

148. Greenspan, P. and S.D. Fowler, *Spectrofluorometric studies of the lipid probe, nile red.* Journal of Lipid Research, 1985. **26**(7): p. 781-789.

149. Hawe, A., M. Sutter, and W. Jiskoot, *Extrinsic fluorescent dyes as tools for protein characterization.* Pharmaceutical Research, 2008. **25**(7): p. 1487-1499.

150. deTroch, P. and J. Vanderleyden, *Surface properties and motility of rhizobium and azospirillum in relation to plant root attachment.* Microbial Ecology, 1996. **32**(2): p. 149-169.

151. Tiller, K.G., Honeyset.Jl, and M.P.C. Devries, *Soil zinc and its uptake by plants .1. isotopic-exchange equilibria and application of tracer techniques.* Australian Journal of Soil Research, 1972. **10**(2): p. 151-164.

152. Bailey, G.W. and J.L. White, *Soil-pesticide relationships, adsorption and desorption of organic pesticides by soil colloids with implications concerning pesticide bioactivity.* Journal of Agricultural and Food Chemistry, 1964. **12**(4): p. 324-332.

153. Grundler, F.M.W., M. Sobczak, and W. Golinowski, *Formation of wall openings in root cells of Arabidopsis thaliana following infection by the plant-parasitic nematode Heterodera schachtii.* European Journal of Plant Pathology, 1998. **104**(6): p. 545-551.

154. Wakabayashi, H., et al., *Effect of calcium hydroxide paste dressing on uninstrumented root-canal wall.* Journal of Endodontics, 1995. **21**(11): p. 543-545.

155. Zhang, M. and M. Akbulut, *Adsorption, desorption, and removal of polymeric nanomedicine on and from cellulose surfaces: effect of size.* Langmuir, 2011. **27**(20): p. 12550-12559.

156. Hunter, A.K. and G. Carta, *Protein adsorption on novel acrylamido-based polymeric ion-exchangers - IV. Effects of protein size on adsorption capacity and rate.* Journal of Chromatography A, 2002. **971**(1-2): p. 105-116.

157. Aboudzadeh, M.R., J.W. Zhu, and W. Bin, *Simulation of protein adsorption in a batchwise affinity chromatography with a modified rate model.* Korean Journal of Chemical Engineering, 2006. **23**(6): p. 997-1002.

158. Chen, S.H., H. Yao, and K. Kimura, *Reversible transference of Au nanoparticles across the water and toluene interface: a langmuir type adsorption mechanism.* Langmuir, 2001. **17**(3): p. 733-739.

159. Xu, Y.M. and C.H. Langford, *UV- or visible-light-induced degradation of X3B on TiO2 nanoparticles: The influence of adsorption.* Langmuir, 2001. **17**(3): p. 897-902.

160. Shar, J.A., et al., *Adsorption studies of diblock copolymers at the cyclohexane/carbon black interface.* Langmuir, 1999. **15**(22): p. 7688-7694.

161. Paul, M., et al., *Pentamidine-loaded poly(D,L-lactide) nanoparticles: Adsorption and drug release.* Drug Development Research, 1998. **43**(2): p. 98-104.

162. Lea, P.J. and R.C. Leegood. *Plant biochemistry and molecular biology*, John Wiley & Sons. New York. 1993.

163. Oparka, K.J.. *Plasmodesmata*. Blackwell. Oxford. 2005.

164. Robards, A.W., *Plasmodesmata.* Annual Review of Plant Physiology and Plant Molecular Biology, 1975. **26**: p. 13-29.

165. Roberts, A.G. and K.J. Oparka, *Plasmodesmata and the control of symplastic transport.* Plant, Cell & Environment, 2003. **26**(1): p. 103-124.

166. Lee, W.M., et al., *Toxicity and bioavailability of copper nanoparticles to the terrestrial plants mung bean (Phaseolus radiatus) and wheat (Triticum aestivum): Plant agar test for water-insoluble nanoparticles.* Environmental Toxicology and Chemistry, 2008. **27**(9): p. 1915-1921.

167. Hischemoller, A., et al., *In-vivo imaging of the uptake of upconversion nanoparticles by plant roots.* Journal of Biomedical Nanotechnology, 2009. **5**(3): p. 278-284.

168. Lin, D.H. and B.S. Xing, *Phytotoxicity of nanoparticles: inhibition of seed germination and root growth.* Environmental Pollution, 2007. **150**(2): p. 243-250.

169. Zhu, H., et al., *Uptake, translocation, and accumulation of manufactured iron oxide nanoparticles by pumpkin plants.* Journal of Environmental Monitoring, 2008. **10**(6): p. 713-717.

170. Lin, S.J., et al., *Uptake, translocation, and transmission of carbon nanomaterials in rice plants.* Small, 2009. **5**(10): p. 1128-1132.

171. Navarro, D.A., Bisson, M, Aga, B. D, *Investigating uptake of water-dispersible CdSe/ZnS quantum dot nanoparticles by Arabidopsis thaliana plants.* Journal of Hazardous Materials, 2012. **211-212**: p. 427-435.

172. Spiering, M.J., et al., *Distribution of the fungal endophyte Neotyphodium lolii is not a major determinant of the distribution of fungal alkaloids in Lolium perenne plants.* Phytochemistry, 2005. **66**(2): p. 195-202.

173. Amiard, V., et al., *Fate of fructose supplied to leaf sheaths after defoliation of Lolium perenne L.: assessment by 13C-fructose labelling.* Journal of Experimental Botany, 2003. **54**(385): p. 1231-1243.

174. Moreno, M.A., et al., *liguleless encodes a nuclear-localized protein required for induction of ligules and auricles during maize leaf organogenesis.* Genes & Development, 1997. **11**(5): p. 616-628.

175. Endre, N.. *1 - On mass transport through a membrane layer*, in *Basic equations of the mass transport through a membrane layer*. Elsevier. Oxford. 2012.

176. Nikaido, H. and E.Y. Rosenberg, *Effect of solute size on diffusion rates through the transmembrane pores of the outer-membrane of escherichia-coli.* Journal of General Physiology, 1981. **77**(2): p. 121-135.

177. Gratton, S.E.A., et al., *The effect of particle design on cellular internalization pathways.* Proceedings of the National Academy of Sciences, 2008. **105**(33): p. 11613-11618.

178. Farokhzad, O.C. and R. Langer, *Impact of nanotechnology on drug delivery.* ACS Nano, 2009. **3**(1): p. 16-20.

179. Davis, M.E., Z. Chen, and D.M. Shin, *Nanoparticle therapeutics: an emerging treatment modality for cancer.* Nat Rev Drug Discov, 2008. **7**(9): p. 771-782.

180. Park, J.H., et al., *Polymeric nanomedicine for cancer therapy.* Progress in Polymer Science, 2008. **33**(1): p. 113-137.

181. Sirk, K.M., et al., *Effect of adsorbed polyelectrolytes on nanoscale zero valent iron particle attachment to soil surface models.* Environmental Science & Technology, 2009. **43**(10): p. 3803-3808.

182. Spiro, T.G., K. Purvis-Roberts, and W.M. Stigliani. *Chemistry of the environment*. Elsevier. Access Online via Elsevier. 2012.

183. Hoffman, A.S., *Hydrogels for biomedical applications.* Advanced Drug Delivery Reviews, 2012. **64**: p. 18-23.

184. Tyrrell, Z.L., Y.Q. Shen, and M. Radosz, *Fabrication of micellar nanoparticles for drug delivery through the self-assembly of block copolymers.* Progress in Polymer Science, 2010. **35**(9): p. 1128-1143.

185. Gupta, H., et al., *Biodegradable levofloxacin nanoparticles for sustained ocular drug delivery.* Journal of Drug Targeting, 2011. **19**(6): p. 409-417.

186. Cheow, W.S., M.W. Chang, and K. Hadinoto, *Antibacterial efficacy of inhalable levofloxacin-loaded polymeric nanoparticles against E. coli biofilm cells: the effect of antibiotic release profile.* Pharmaceutical Research, 2010. **27**(8): p. 1597-1609.

187. Akbulut, M., et al., *Novel methods of targeted drug delivery: the potential of multifunctional nanoparticles.* Expert Review of Clinical Pharmacology, 2009. **2**(3): p. 265-282.

188. Hook, F., et al., *Variations in coupled water, viscoelastic properties, and film thickness of a Mefp-1 protein film during adsorption and cross-linking: A quartz crystal microbalance with dissipation monitoring, ellipsometry, and surface plasmon resonance study.* Analytical Chemistry, 2001. **73**(24): p. 5796-5804.

189. Voinova, M.V., et al., *Viscoelastic acoustic response of layered polymer films at fluid-solid interfaces: continuum mechanics approach.* Physica Scripta, 1999. **59**(5): p. 391-396.

190. Domack, A., et al., *Swelling of a polymer brush probed with a quartz crystal resonator.* Physical Review E, 1997. **56**(1): p. 680-689.

191. Reimhult, E., et al., *A multitechnique study of liposome adsorption on Au and lipid bilayer formation on SiO2.* Langmuir, 2006. **22**(7): p. 3313-3319.

192. Min, Y.J., et al., *The role of interparticle and external forces in nanoparticle assembly.* Nature Materials, 2008. **7**(7): p. 527-538.

193. Hajdu, A., et al., *Surface charging, polyanionic coating and colloid stability of magnetite nanoparticles.* Colloids and Surfaces a-Physicochemical and Engineering Aspects, 2009. **347**(1-3): p. 104-108.

194. Nayeri, M., R. Karlsson, and J. Bergenholtz, *Surfactant effects on colloidal interactions: concentrated micellar solutions of nonionic surfactant.* Colloids and Surfaces a-Physicochemical and Engineering Aspects, 2010. **368**(1-3): p. 84-90.

195. Zhang, M., et al., *Uptake and translocation of polymeric nanoparticulate drug delivery systems into ryegrass.* RSC Advances, 2012. **2**(25): p. 9679-9686.

196. Strauss, J., Y. Liu, and T. Camesano, *Bacterial adhesion to protein-coated surfaces: an AFM and QCM-D study.* Jom, 2009. **61**(9): p. 71-74.

197. Malmström, J., et al., *Viscoelastic modeling of highly hydrated laminin layers at homogeneous and nanostructured surfaces: quantification of protein layer properties using QCM-D and SPR.* Langmuir, 2007. **23**(19): p. 9760-9768.

198. Olanya, G., et al., *Protein interactions with bottle-brush polymer layers: Effect of side chain and charge density ratio probed by QCM-D and AFM.* Journal of Colloid and Interface Science, 2010. **349**(1): p. 265-274.

199. López, A.E., et al., *Influence of surface chemistry and protein concentration on the adsorption rate and S-layer crystal formation.* Physical Chemistry Chemical Physics, 2011. **13**(25): p. 11905-11913.

200. Lu, N., J.L. Zilles, and T.H. Nguyen, *Adsorption of extracellular chromosomal DNA and its effects on natural transformation of azotobacter vinelandii.* Applied and Environmental Microbiology, 2010. **76**(13): p. 4179-4184.

201. Kao, W.-L., et al., *Adsorption behavior of plasmid DNA on binary self-assembled monolayers modified gold substrates.* Journal of Colloid and Interface Science, 2012. **382**(1): p. 97-104.

202. Ziółkowski, R., et al., *Electrochemical uranyl biosensor with DNA oligonucleotides as receptor layer.* Analytical and Bioanalytical Chemistry, 2012. **402**(7): p. 2259-2266.

203. Irwin, E.F., et al., *Analysis of interpenetrating polymer networks via quartz crystal microbalance with dissipation monitoring.* Langmuir, 2005. **21**(12): p. 5529-5536.

204. Orski, S.V., et al., *Design and implementation of two-dimensional polymer adsorption models: evaluating the stability of candida antarctica lipase B/solid-support interfaces by QCM-D.* Biomacromolecules, 2013. **14**(2): p. 377-386.

205. Slavin, S. and D.M. Haddleton, *An investigation into thiol-ene surface chemistry of poly(ethylene glycol) acrylates, methacrylates and CCTP polymers via quartz crystal microbalance with dissipation monitoring (QCM-D).* Soft Matter, 2012. **8**(40): p. 10388-10393.

206. Dunér, G., E. Thormann, and A. Dėdinaitė, *Quartz crystal microbalance with dissipation (QCM-D) studies of the viscoelastic response from a continuously growing grafted polyelectrolyte layer.* Journal of Colloid and Interface Science, **408**: p. 229-234.

207. Vangeyte, P., et al., *Adsorption of poly(ethylene oxide)-b-poly(E-caprolactone) copolymers at the silica-water interface.* Langmuir, 2005. **21**(7): p. 2930-2940.

208. Liu, Y.P. and S.L. Regen, *Control over vesicle rupture and leakage by membrane packing and by the aggregation state of an attacking surfactant.* Journal of the American Chemical Society, 1993. **115**(2): p. 708-713.

209. Idiart, M.A. and Y. Levin, *Rupture of a liposomal vesicle.* Physical Review E, 2004. **69**(6): p. 061922.

210. Kirby, B.J. and E.F. Hasselbrink, *Zeta potential of microfluidic substrates: 1. Theory, experimental techniques, and effects on separations.* Electrophoresis, 2004. **25**(2): p. 187-202.

211. Zdyrko, B., et al., *Adsorption of copolymers aggregates: from kinetics to adsorbed layer structure.* Journal of Colloid and Interface Science, 2008. **322**(2): p. 365-374.

212. Kim, D., W. Cha, and R.L. Beissinger, *Mass-transport of macromolecules in solution to surfaces.* Journal of Colloid and Interface Science, 1993. **159**(1): p. 1-8.

213. Polyanin, A.D.. *Handbook of linear partial differential equations for engineers and scientists*. Chapman & Hall/CRC. London. 2002.

214. Hillier, A.C. and M.D. Ward, *Scanning electrochemical mass sensitivity mapping of the quartz crystal microbalance in liquid media.* Analytical Chemistry, 1992. **64**(21): p. 2539-2554.

215. Bird, R.B., W.E. Stewart, and E.N. Lightfoot. *Transport phenomena*. John Wiley & Sons. New York. 2007.

216. Lok, B.K., Y.L. Cheng, and C.R. Robertson, *Protein adsorption on crosslinked polydimethylsiloxane using total internal-reflection fluorescence.* Journal of Colloid and Interface Science, 1983. **91**(1): p. 104-116.

217. Fu, Z.G. and M.M. Santore, *Poly(ethylene oxide) adsorption onto chemically etched silicates by Brewster angle reflectivity.* Colloids and Surfaces a-Physicochemical and Engineering Aspects, 1998. **135**(1-3): p. 63-75.

218. Mubarekyan, E. and M.M. Santore, *Adsorption and exchange dynamics in aging hydroxyethylcellulose layers on silica.* Journal of Colloid and Interface Science, 2000. **227**(2): p. 334-344.

219. Daly, S.M., T.M. Przybycien, and R.D. Tilton, *Adsorption of poly(ethylene glycol)-modified ribonuclease A to a poly(lactide-co-glycolide) surface.* Biotechnology and Bioengineering, 2005. **90**(7): p. 856-868.

220. Cho, E.C., Q. Zhang, and Y.N. Xia, *The effect of sedimentation and diffusion on cellular uptake of gold nanoparticles.* Nature Nanotechnology, 2011. **6**(6): p. 385-391.

221. Kosslinger, C., et al., *Comparison of the QCM and the SPR method for surface studies and immunological applications.* Sensors and Actuators B-Chemical, 1995. **24**(1-3): p. 107-112.

222. Olsson, A.L.J., et al., *Influence of cell surface appendages on the bacterium−substratum interface measured real-time ssing QCM-D.* Langmuir, 2008. **25**(3): p. 1627-1632.

223. Sharma, M.M., et al., *Factors controlling the hydrodynamic detachment of particles from surfaces.* Journal of Colloid and Interface Science, 1992. **149**(1): p. 121-134.

224. Das, S.K., M.M. Sharma, and R.S. Schechter, *Adhesion and hydrodynamic removal of colloidal particles from surfaces.* Particulate Science and Technology, 1995. **13**(3-4): p. 227-247.

225. Burdick, G.M., N.S. Berman, and S.P. Beaudoin, *Hydrodynamic particle removal from surfaces.* Thin Solid Films, 2005. **488**(1-2): p. 116-123.

APPENDIX A

SUPPLEMENTAL INFORMATION FOR CHAPTER III

A1 List of Variables and Abbreviations

A: the Hamaker constant, J

b: the length of the sensor that is orthogonal to the flow direction, m

D: diameter of PNDDS, m

$D_c(h)$: the diffusion coefficient, m^2/s

F_A: adhesion force, N

F_D: drag force, N

F_L: lift force, N

h: the separation between the particle and surface, m

k_B: Boltzmann constant, $m^2\ kg\ s^{-2}\ K^{-1}$

k_a: the rate constant of adsorption, m/s

k_d: the rate constant of desorption, 1/s

k_s: the rate constant of spreading, 1/s

l: the distance between two walls of the QCM, m

m_s: the mass concentration of PNDDS in the solution, kg/m^3

R: radius of PNDDS, m

$R_{exposure}$: the rate of concentration change on the surface during the PNDDS exposure stage, kg/m^2

$R_{rinsing}$: the rate of concentration change on the surface during the rising stage, kg/m^2

S: total area of the sensor, m^2

T: temperature, K

t: time, s

V: the fluid velocity as a function of position, m/s

V_c: the fluid velocity at the center of the particle, m/s

V_P: the particle velocity at the center of mass, m/s

W: total interaction energy, J

W_b: the interaction energy at $h = \delta_b$, J

W_m: the interaction energy at $h = \delta_m$, J

W_{vdw}: van der Waals interaction energy, J

W_{Born}: Born interaction energy, J

W_{DL}: double-layer interaction energy, J

Γ_α: the concentration of α-particles (reversibly bound particles) on the sensor surface, kg/m^2

$\Gamma_{\alpha\infty}$: the concentration of α-particles (reversibly bound particles) on the sensor surface at adsorption equilibrium state, kg/m^2

Γ_β: the concentration of β-particles (irreversibly bound particles) on the sensor surface, kg/m^2

Γ^*: the maximum surface concentration of PNDDS that can cover the surface, kg/m^2

δ: the diffusion boundary-layer thickness, m

δ_m: the separation at which there is a primary minimum in the total interaction potential, m

δ_b: the separation at which there is the maximum energy barrier, m

ε:the dielectric constant of the medium, $C^2N^{-1}m^{-2}$

θ: the ratio of non-deformed to total PNDDS mass on the surface of the sensor ($\theta=\Gamma_\alpha/\Gamma$).

θ_∞: the ratio of non-deformed to total PNDDS mass on the surface of the sensor at adsorption equilibrium state

κ^{-1}: Debye length, m

μ: the fluid viscosity, kg (m·s)

ρ: the fluid density, kg m^3

σ: the collision diameter, m

$\Phi_{\alpha}(t)$: the probability of an incoming α-particle to land in a non-overlapping on the surface

χ: the coefficient of static friction or the rolling resistance coefficient

$\Psi_{\alpha\beta}(t)$: the probability of an α-particle that is already on the surface to have sufficient area to spread

ψ_{s1}:surface potential of the PNDDS, V

ψ_{s2}:surface potential of cellulose surface, V

APPENDIX B

SUPPLEMENTAL INFORMATION FOR CHAPTER IV

B1 Numerical Calculation of k_a and k_{up}

In Section 4.3.6, we got the follow expression for kinetics of uptake:

$$\Gamma^* \frac{V}{k_a S}\frac{d^2\ln(m_s)}{dt^2} + \frac{V}{S}\left(m_s + \frac{k_{up}\Gamma^*}{k_a}\right)\frac{d\ln(m_s)}{dt} + k_{up}\Gamma^* = 0 \quad [4.5]$$

$$\Gamma^* \frac{V}{k_a S}\frac{d^2\ln(m_s)}{dt^2} + \frac{V}{S}\left(e^{\ln(m_s)} + \frac{k_{up}\Gamma^*}{k_a}\right)\frac{d\ln(m_s)}{dt} + k_{up}\Gamma^* = 0 \quad [4.6]$$

if let $\ln(m_s) = x$, so

$$\Gamma^* \frac{V}{k_a S}\frac{d^2x}{dt^2} + \frac{V}{S}\left(e^{x} + \frac{k_{up}\Gamma^*}{k_a}\right)\frac{dx}{dt} + k_{up}\Gamma^* = 0 \quad [4.7]$$

$$\frac{d^2x}{dt^2} + \left(\frac{k_a}{\Gamma^*}e^{x} + k_{up}\right)\frac{dx}{dt} + \frac{S}{V}k_a k_{up} = 0 \quad [4.8]$$

integral both side:

$$\frac{dx}{dt} - \left(\frac{dx}{dt}\right)_{t=0} + \frac{k_a}{\Gamma^*}(e^{x} - e^{x_0}) + k_{up}(x - x_0) + \frac{S}{V}k_a k_{up} t = 0 \quad [4.9]$$

$$\frac{dx}{dt} = -[\frac{k_a}{\Gamma^*}(e^{x} - e^{x_0}) + k_{up}(x - x_0) + \frac{S}{V}k_a k_{up} t] + \left(\frac{dx}{dt}\right)_{t=0} \quad [4.10]$$

$$\frac{dx}{dt} = \frac{x_1 - x_0}{\Delta t} = -[\frac{k_a}{\Gamma^*}(e^{x} - e^{x_0}) + k_{up}(x - x_0) + \frac{S}{V}k_a k_{up} t] + \left(\frac{dx}{dt}\right)_{t=0} \quad [4.11]$$

Using numerical intergration

$$x_0 = x_0 \quad [4.12]$$

$$\left(\frac{dx}{dt}\right)_{t=0} = -\frac{k_a S}{V} \quad [4.13]$$

$$x_1 = -\frac{k_a S}{V}\Delta t + x_0 \quad [4.14]$$

$$x_2 = -[\frac{k_a}{\Gamma^*}(e^{x_1} - e^{x_0}) + k_{up}(x_1 - x_0) + \frac{S}{V}k_a k_{up} t + \frac{k_a S}{V}]\Delta t + x_1 \quad [4.15]$$

…

$$x_i = -[\frac{k_a}{\Gamma^*}(e^{x_{i-1}} - e^{x_0}) + k_{up}(x_{i-1} - x_0) + \frac{S}{V}k_a k_{up} t + \frac{k_a S}{V}]\Delta t + x_{i-1} \quad [4.16]$$

Matlab was used to fit k_a and k_{up}, by $\min[(x_{t=0}-x_{t=0}')^2+(x_{t=1}-x_{t=1}')^2+\ldots+(x_{t=48}-x_{t=48}')^2]$ with Δt=1 6 hr, Γ^* constant as described below.

```
function [ y ] = kinetic ( k,j )
% k is (ka,kup) and j is for different size
V=6*10^-6; %
S=6.28*10^-5;
G=0.6;%gamma
n=6;
dt=1/n;
x(1)=4.89;%initial scale
for i=1:48*n
    x(i+1)=-(k(1)*S/V+k(1)/G*(exp(x(i))-exp(x(1)))+k(2)*(x(i)-
x(1))+S/V*k(1)*k(2)*(i-1)/6)*dt+x(i);
end

B=[4.891 4.861 4.815 4.762 4.648 4.395
    4.891 4.876 4.855 4.834 4.781 4.738
    4.891 4.865 4.868 4.806 4.724 4.652
    4.889 4.869 4.862 4.827 4.790 4.745
    4.892 4.887 4.864 4.840 4.807 4.777
    4.890 4.866 4.857 4.836 4.799 4.780
    4.891 4.876 4.851 4.829 4.824 4.815]; %from SFM results
A=B(j,:);

y=(x(1)-A(1))^2+(x(1+n*1)-A(2))^2+(x(1+n*3)-A(3))^2+(x(1+n*9)-
A(4))^2+(x(1+n*27)-A(5))^2+(x(1+n*48)-A(6))^2;

end



clear all;
for j=1:7
    k=fminsearch(@(k) kinetic (k,j), [0.002, 0.63])
end
```

APPENDIX C

SUPPLEMENTAL INFORMATION FOR CHAPTER V

C1 Numerical Calculation of the Average Adsorption Rate Constant k_a

In Section 5.3.7, we derived the following expression for the adsorption rate constant, k_a:

$$k_a = \frac{D^{2/3}}{Gamma\left(\frac{4}{3}\right)}\left(\frac{6K}{9bS}\right)^{1/3} \quad [5.30]$$

where $K = \frac{Q}{\pi b}$ and $S = \int_{\tau=-\infty}^{\tau} h_\sigma h_\tau d\tau$. Diffusivity, D_c, can be calculated from the particle size using Stokes-Einstein equations:

$$D_c = \frac{k_B T}{6\pi R\eta} \quad [5.32].$$

To calculate the average k_a over the measurement area of QCM-D (i.e. $r \leq$ 3mm), the area integration is performed as follows:

$$< k_a >= \int_{x=-r}^{x=r} \int_{y=0}^{y=\sqrt{r^2-x^2}} k_a \, dy \, dx \quad [5.33]$$

This integration was numerically carried out Matlab as described below.

```
clear all;
a=0.005; % radius of the chamber, m
b=0.00064; % thickness of the chamber, m
r=0.003; % radius of measurement area, m
dx=0.00001; % step size of x and y for integral, m
du=0.01;     u, v were used for τ, σ, du is the step size of u for integral
M=0;
for x=0-r:dx:r
   ym=sqrt(r^2-x^2);
   for y=0:dx:ym
      u=log(sqrt((x+a)^2+y^2)/sqrt((a-x)^2+y^2));
      v=atan((a+x)/y)+atan((a-x) y);     convert (x, y) to (τ, σ)
      S=0;
      for i=-10:du:u
         S=S+1/(cosh(i)-cos(v))^2*du;
```

```
        end
        ka=1/0.893*(6/pi/b^2/a^2/S/9)^(1/3); % local ka without D
        M=M+ka;
    end
end
N=M*dx*dx/pi/0.003^2*2 % average ka without D
%%<ka>=N*D^(2/3)*Q^(1/3)
```

C2 Calculation of Mass Transport due to Diffusion at Different Directions

The concentration profile inside the QCM-D chamber was calculated to be:

$$\frac{c}{c_0} = \frac{\int_0^{\eta} e^{-m^3} dm}{Gamma\left(\frac{4}{3}\right)} \qquad [5.34].$$

The mass transport due to diffusion at different directions can be calculated by taking the second derivative of the concentration with respect to the direction of interest.

For diffusion at z-direction:

$$-D_c \left[\left(\frac{\partial c}{\partial z}\right)|_z - \left(\frac{\partial c}{\partial z}\right)|_{z+dz}\right] h_\sigma d\sigma h_\tau d\tau = D_c \frac{\partial^2 c}{\partial z^2} * dV \qquad [5.35]$$

$$\frac{\partial c}{\partial z} = \frac{c_0}{Gamma\left(\frac{4}{3}\right)} e^{-\eta^3} \frac{\partial \eta}{\partial z} = \frac{c_0}{Gamma\left(\frac{4}{3}\right)} e^{-\eta^3} \left(\frac{6K}{9DbS}\right)^{1/3} \qquad [5.36]$$

$$\frac{\partial^2 c}{\partial z^2} = \frac{c_0}{Gamma\left(\frac{4}{3}\right)} e^{-\eta^3} * (-3\eta^2) \left(\frac{6K}{9DbS}\right)^{2/3} \qquad [5.37]$$

For diffusion at τ-direction:

$$-D\left[\left(\frac{\partial c}{h_\tau \partial \tau}\right)|_\tau - \left(\frac{\partial c}{h_\tau \partial \tau}\right)|_{\tau+d\tau}\right] h_\sigma d\sigma dz = D \frac{\partial}{h_\tau \partial \tau}\left(\frac{\partial c}{h_\tau \partial \tau}\right) * dV \qquad [5.38]$$

$$\frac{\partial c}{h_\tau \partial \tau} = \frac{c_0}{Gamma\left(\frac{4}{3}\right)} e^{-\eta^3} \frac{1}{h_\tau} \frac{\partial \eta}{\partial \tau} = \frac{c_0}{Gamma\left(\frac{4}{3}\right)} e^{-\eta^3} \eta \frac{1}{3} S^{-1} h_\sigma \qquad [5.39]$$

$$\frac{\partial}{h_\tau \partial \tau}\left(\frac{\partial c}{h_\tau \partial \tau}\right) = \frac{c_0}{Gamma\left(\frac{4}{3}\right)} e^{-\eta^3} \left[\frac{1}{3S} \frac{\partial \eta}{\partial \tau} - \frac{\eta h_\tau h_\sigma}{3S^2} + \frac{\eta}{3S} \frac{\partial h_\sigma}{h_\tau \partial \tau} - \eta^3 S^{-1} \frac{\partial \eta}{\partial \tau}\right] \qquad [5.40]$$

For diffusion at σ-direction:

$$-D\left[\left(\frac{\partial c}{h_\sigma \partial \sigma}\right)|_\sigma - \left(\frac{\partial c}{h_\sigma \partial \sigma}\right)|_{\sigma+d\sigma}\right] h_\tau d\tau dz = D\frac{\partial}{h_\sigma \partial \sigma}\left(\frac{\partial c}{h_\sigma \partial \sigma}\right) * dV \quad [5.41]$$

$$\frac{\partial c}{h_\sigma \partial \sigma} = \frac{c_0}{Gamma\left(\frac{4}{3}\right)} e^{-\eta^3} \frac{1}{h_\sigma}\frac{\partial \eta}{\partial \sigma} = \frac{c_0}{Gamma\left(\frac{4}{3}\right)} e^{-\eta^3} \frac{1}{h_\sigma}\eta\frac{1}{3}S^{-1}\int_{\tau=-\infty}^{\tau}\frac{\partial}{\partial \sigma}(h_\sigma h_\tau)d\tau \quad [5.42]$$

$$\text{Let } \int_{\tau=-\infty}^{\tau}\frac{\partial}{\partial \sigma}(h_\sigma h_\tau)d\tau = M \quad [5.43]$$

$$\frac{\partial}{h_\sigma \partial \sigma}\left(\frac{\partial c}{h_\sigma \partial \sigma}\right) = \frac{c_0}{Gamma\left(\frac{4}{3}\right)} e^{-\eta^3}\left[\frac{-\eta M}{3(h_\sigma)^3 S}\frac{\partial h_\sigma}{\partial \sigma} + \frac{M}{3{h_\sigma}^2 S}\frac{\partial \eta}{\partial \sigma} - \frac{\eta M^2}{3{h_\sigma}^2 S^2} + \frac{\eta}{3{h_\sigma}^2 S}\frac{\partial M}{\partial \sigma} - \frac{\eta^3 M}{{h_\sigma}^2 S}\frac{\partial \eta}{\partial \sigma}\right] \quad [5.44]$$

$$\text{where } \eta = z\left(\frac{6K}{9DbS}\right)^{1/3} = z\left(\frac{6K}{9DbS}\right)^{1/3};\ K = \frac{Q}{\pi b}\ ; \text{and}\ S = \int_{\tau=-\infty}^{\tau} h_\sigma h_\tau d\tau. \quad [5.45]$$

$$\frac{\partial \eta}{\partial \tau} = z\left(\frac{6K}{9Db}\right)^{1/3}\frac{1}{3}S^{-\frac{2}{3}}h_\sigma h_\tau = \eta\frac{1}{3}S^{-1}h_\sigma h_\tau \quad [5.46]$$

$$\frac{\partial \eta}{\partial \sigma} = z\left(\frac{6K}{9Db}\right)^{1/3}\frac{1}{3}S^{-\frac{2}{3}}\int_{\tau=-\infty}^{\tau}\frac{\partial}{\partial \sigma}(h_\sigma h_\tau)d\tau = \eta\frac{1}{3}S^{-1}\int_{\tau=-\infty}^{\tau}\frac{\partial}{\partial \sigma}(h_\sigma h_\tau)d\tau = \eta\frac{1}{3}S^{-1}M \quad [5.47]$$

$$\frac{\partial \eta}{\partial z} = \left(\frac{6K}{9DbS}\right)^{1/3} = \frac{\eta}{z} \quad [5.48]$$

Table 5.2 summarizes the calculated diffusion induced mass transport at τ-, σ-, and z-directions for selection locations. As can readily be seen, the magnitude of the mass transport due to diffusion at z-direction was much larger than that at τ- and σ-directions.

Table 5.2. Calculated diffusion induced mass transport at τ-, σ-, and z-directions for some selected points

	Position	Diffusion (kg/s)	D_z/D_σ	(x,y,z) m
τ	0	1.35E-05	-2.16E+04	(0, 2E-3, 1E-5)
σ	2.356194	-2.45E-05		
z	1.00E-05	5.30E-01		
τ	0	1.35E-05	-2.16E+04	(0, -2E-3, 1E-5)
σ	3.926991	-2.45E-05		
z	1.00E-05	5.30E-01		
τ	-1	4.72E-05	-6.10E+04	(-2.6E-3, 1.5E-3, 1E-5)
σ	2.356194	-3.33E-05		
z	1.00E-05	2.03E+00		
τ	-1	8.25E-89	2.35E+05	(-2.6E-3, 1.5E-3, 1E-4)
σ	2.356194	8.08E-91		
z	1.00E-04	1.90E-85		
τ	-1	9.10E-06	-6.51E+03	(-2.6E-3, 1.5E-3, 1E-5)
σ	2.356194	-4.30E-05		
z	1.00E-05	2.80E-01		
τ	0	1.40E-06	-2.11E+03	(0, 1.5E-3, 1E-6)
σ	2.356194	-2.70E-06		
z	1.00E-06	5.70E-03		

The following Matlab code was used to numerically calculate the mass transport due to diffusion shown above.

```
function y = Diffusion(x1,x2,x3)
%x1=tao, x2=sigma, x3=z
%y1,y2,y3: diffusion at x1,x2,x3
c0=500;
a=0.005;
Q=2.5E-9;
b=0.64E-3;
D=5.45E-12; %diffusion coefficient for 90-nm partilces
gamma=0.893; %Gamma(4/3)
K=Q/pi/b;
s=0;%s=S/a^2
m=0;%m=ds/dx2
```

```
n=0;%n=dm/dx2
dx1=0.01;
      for   i=-30:dx1:x1
            s=s+1/(cosh(i)-cos(x2))^2;
            m=m-2/(cosh(i)-cos(x2))^3*sin(x2);
            n=n+6/(cosh(i)-cos(x2))^4*sin(x2)*sin(x2)-2/(cosh(i)-
cos(x2))^3*cos(x2);
      end
S=dx1*s*a^2;
M=dx1*m*a^2;
N=dx1*n*a^2;
h=a/(cosh(x1)-cos(x2));
eta=x3*(6*K/9/D/b/S)^(1/3);
etax1=eta/3/S*h^2; %d(eta)/dx1
etax2=eta/3/S*M; %d(eta)/dx2
y1=1/3/S*etax1-1/3*eta/S^2*h^2+1/3*eta/S/h*(-1)*a/(cosh(x1)-
cos(x2))^2*sinh(x1)-eta^3/S*etax1;
y2=M*eta/h^3/3/S*a/(cosh(x1)-cos(x2))^2*sin(x2)+etax2*M/h^2/3/S-
M^2*eta/3/h^2/S^2+N*eta/h^2/3/S-eta^3*M*etax2/h^2/S;
y3=-3*eta^4/x3^2;
y=-1*D*[y1 y2 y3]*c0/gamma*exp(-3*eta^3);
end
```

C3 List of Variables and Abbreviations

a: the distance from inlet/outlet to center of the QCM chamber, m

b: the depth of the QCM chamber gap, m

c: the mass concentration of nanomedicine in solution, g/m^3

c_0: the mass concentration of nanomedicine in inlet solution, g/m^3

D: diameter of nanomedicine, m

D_c: the diffusion coefficient, m^2/s

h_ζ, h_η: scale factors for ζ coordinate and η coordinate, m

K: $Q/\pi b$, m^2/s

k_B: Boltzmann constant, m^2 kg s^{-2} K^{-1}

k_a: the rate constant of adsorption, m/s

k_r: the rate constant of removal, 1/s

m_s: the mass concentration of nanomedicine in bulk solution, g/m^3

r_1, r_2: distance of a point to two foci F_1 and F_2, m

Q: flow rate of fluid, m^3/s

R: radius of nanomedicine, m

$R(c)$: unknown intrinsic kinetic rate expression for particle adsorption, g/m^2s

S: the sweep area from $\eta = -\infty$ (inlet) to $\eta = \eta$ with the width of $h_\zeta d\zeta$, m^2

T: temperature, K

t: time, s

u: $z\times[6Kd\zeta/(9bDS)]1/3$, similarity variable used for solving Equation 17

v_ζ, v_η, v_z: fluid velocities at ζ, η and z coordinate, m/s

η: the fluid viscosity, kg (m·s)

θ: the ratio of non-deformed to total nanomedicine mass on the surface of the sensor ($\theta=\Gamma_\alpha/\Gamma$).

Γ_α: the concentration of α-particles (reversibly bound particles) on the sensor surface, g/m^2

Γ: the concentration of nanomedince on the sensor surface, g/m^2

Γ^*: the maximum surface concentration of nanomedicine that can cover the surface, g/m^2